UNIVERSITY OF CALIFORNIA
SANTA CRUZ

SYNTHESIS, CHARACTERIZATION, AND EXCITON DYNAMICS OF II-VI SEMICONDUCTING NANOMATERIALS AND AB-INITIO STUDIES FOR APPLICATIONS IN EXPLOSIVES SENSING

A dissertation submitted in partial satisfaction
Of the requirements for the degree of

DOCTOR OF PHILOSOPHY

in

CHEMISTRY

by

Jason K. Cooper

June 2013

The Dissertation of Jason K. Cooper is approved:

_____
Professor Jin Zhang, chair

_____
Assistant Professor Yat Li

_____
Professor Ilan Benjamin

_____
Tyrus Miller
Vice Provost and Dean of Graduate Studies

TABLE OF CONTENTS

LIST OF FIGURES AND TABLES

CHAPTER 1

CHAPTER 2

CHAPTER 3

ABSTRACT

SYNTHESIS, CHARACTERIZATION, AND EXCITON DYNAMICS OF II-VI SEMICONDUCTING NANOMATERIALS AND AB-INITIO STUDIES FOR APPLICATIONS IN EXPLOSIVES SENSING

by

JASON K. COOPER

II-VI semiconducting nanostructures have been intensively researched as promising materials in applications including sensing, light emitting diodes (LEDs), lasers, photoelectrochemical (PEC) materials for water splitting and photo-catalysis, and dye or quantum dot sensitized solar cells. On the nanoscale, structural morphology plays a significant role in determining optical, electronic, and physical properties, and thus consequently affects the ultimate device properties.

In zero-dimensional quantum dots (QDs), control of the crystal size can allow for tunability of properties such as the absorption and emission spectrum. As a result, these nanostructures have proven attractive for QD-LEDs, biological labeling, and sensing. Because of the high surface to volume ratio of QDs, the surface quality and structure of these nanocrystals play a significant role in carrier trapping and non-radiative decay processes. QD surfaces can be effectively passivized by increasing the coordination number of surface atoms through coordinating capping ligands. Ligands improve photoluminescence (PL) quantum yield by healing dangling bond bandgap states, but they can also insert electron acceptor states below the conduction band (CB), which can trap photoelectrons and quench QD PL. This latter approach

has been investigated for sensing applications such as in explosives detection. Characterization using density function theory DFT and time dependent DFT has been applied to study the acceptor levels in six explosives to help target different II-VI materials as potential fluorescent probes.

In one-dimensional quantum rods or wires, the exciton can be confined in two dimensions, leaving the third available for transport. These structures are promising in light harvesting applications such as PEC water splitting and solar cells. Nanowire (NW) photoanodes allow for efficient collection of photogenerated electrons by providing a direct route to the back contact while minimizing the distance the photohole must travel to reach the solution interface. At the same time, the added surface area increases the surface/electrolyte contact area, as well as improves sensitizer loading, the latter of which has been studied to improve performance in the visible portion of the spectrum. Common sensitizers for metal oxide (MO) anodes, which have large bandgaps and therefore do not absorb visible photons, include organic dyes, QDs, and in some studies the use of metal nanoparticles (NPs) has been proposed. Metal NPs, with their size and shape tunable surface plasmon resonance, can be controlled through the visible-NIR portion of the spectrum, and have been investigated as potential sensitizers on ZnO photoanodes using ultrafast transient absorption spectroscopy.

Enhanced performance of MO photoanodes can also be achieved through various annealing treatments meant to improve crystallinity, decrease intrinsic trapping defects, increase donor concentration by encouraging advantageous defects

in n-type semiconductors, or passivate undesirable defects. The effect of air and hydrogen annealing of ZnO NWs on PEC performance was investigated with *in-situ* TA spectroscopy which showed that the combination of these methods improves PEC water splitting efficiency.

Finally, the application of II-VI materials in three-dimensional thin films has shown great potential in next generation photovoltaics which include the CdS/CdTe solar cell. The n-type CdS window layer, which forms the p-n junction with p-type CdTe, can be deposited by several different techniques but commonly include: DC pulse sputtering (DCPS) and chemical bath deposition (CBD). The dynamics of photoexcited charge carriers in CdS films prepared these methods was investigated with ultrafast transient absorption spectroscopy and the results was analyzed using singular value decomposition global fitting. The CBD sample had significant donor, acceptor, and donor acceptor pair recombination attributed to high oxygen content in the films while the DCPS had intrinsic donor level defects which are expected for n-type CdS. The results suggest that DCPS made thin films should offer improved performance in solar cell applications.

DEDICATION

I dedicate this work to my parents John and Linda Burroughs

Your support and guidance made this possible. The words ‘thank you’ do not express the gratitude I have for all you have done for me. I love you both.

And to Brian Lock and Christina Brady

For a lifetime of friendship, both what has past and has yet to come; and, countless meals over the past four years.

ACKNOWLEDGEMENTS

First, of course I would like to thank my advisor Jin Zhang. There are many things about your advising style I appreciate which I would like to notice. You have always been very fair with me and other students. You hold people to a high standard and expect the best of people which makes them try harder than they might on their own and achieve more than they set out to accomplish. You care about each and every one of your students and do what you can to make the start of their careers a success. You tailor your expectations, method of motivation, and oversight on a student by student basis which indicates you are attentive and dedicated to helping people. Your analogies, while intended to help explain complex topics, are always a good source of smiles later. "If your car doesn't start in the morning on your way to work, you need to check step by step, what could be the problem? Maybe there is no air in the tires." Thank you for everything. You will be missed.

Yat Li, your poignant questions during group meeting and in the hallways, inquisitive nature, and positive friendly group you cultivate made collaborations easy, fruitful, and fun. You have always been generous with your time and with your resources and your friendly demeanor made working with you a great experience. Thank you.

Ilan Benjamin, I wish we had a chance to work more on projects together; the well of time is never a deep as you hope it to be. You have been so generous with your computational resources and with your time. You were very supportive when I

propositioned you to install Gaussian on your cluster and made the process easy and positive. I hope you found the work we did end up doing together worthwhile, I know I did.

To the three of you, I hope we have the opportunity to continue working together even after I leave.

To the Zhang Lab, Sheraz Gul, Robert Fitzmorris, Damon Wheeler, Carley Corrado, Rebecca Newhouse, Jenny Hensel, Staci Adams, Liat Zavodivker, and Sarah Lindley I couldn't have asked for a better group of people to work with every day. You have all been a joy to work with and learn from in scientific endeavors as well as in personal growth. I wish all of you the very best of luck with your futures. Also, Alexandra Franco you were a great help in the lab and a wonderful friend; I am fortunate to have met you.

Yichuan Ling, you are always happy to help and share your time and assistance in making films and getting projects done. I could always count on and trust you. The remaining Li Lab, generally the most dedicated group of people I may have ever met. You all set the bar for hard work and focus; it was inspiring to witness. Stephen Hauskins, thank you for helping with my countless computer related questions regarding Linux and being so generous with your time getting Gaussian to work properly. Jim Lewis, thank you for collaborating on the several projects we did together involving you laser, you are a wealth of knowledge. Eefei Chen and the remaining Kliger Lab, thank you for being so generous with your optics in times of need. Istvan Szundi, your Matlab code has been a data fitting lifesaver

and has taught me so much about data analysis. Christian Grant, your project ideas, guidance, and expertizes with lasers made it a great pleasure to work with and collaborate with you. Yashar Abdollahian, I wish we could have done a project together, you were always eager to help people with XRD samples and I can't thank you enough for all your help. Burak Himmetoglu, you will I am sure never read this but thank you for your help at the Quantum Espresso conference and for answering all my emails helping me get things going here in Santa Cruz. Tom Yuzvinsky and Robert Hoelle, kings of SEM, thank you both for all the images and indulging my intrigue. Thank you as well to Sophie Ballo for all of your edits.

The text of this dissertation includes reprints of the following previously published material:

Chapter 1: "Characterization of Primary Amine Capped CdSe, ZnSe, and ZnS Quantum Dots by FT-IR: Determination of Surface Bonding Interaction and Identification of Selective Desorption", Cooper, J.K., Franco, A.M., Gul, S., Corrado, C., Zhang, J.Z., Langmuir, **2011**, 27(13), 8486-8493

Chapter 2: "Ultrafast charge carrier dynamics and photoelectrochemical properties of ZnO nanowires decorated with Au nanoparticles", Cooper, J.K., Ling, Y., Zhang, J.Z., **2011**, Proc. SPIE 8109, Solar Hydrogen and Nanotechnology VI, 81090M

Chapter 3: "Effects of Hydrogen Treatment and Air Annealing on Ultrafast Charge Carrier Dynamics in ZnO Nanowires Under *In Situ* Photoelectrochemical Conditions", Cooper, J.K., Ling, Y., Longo, C., Li, Y., Zhang, J.Z., J. Phys. Chem. C, **2012**, 116(33), 17360-17368

Chapter 4: "Ab-Initio Calculation of Ionization Potential and Electron Affinity of Six Common Explosive Compounds", Cooper, J.K., Grant, C.D., Zhang, J.Z., Reports in Theoretical Chemistry, **2012**, 1, 11-19

Chapter 5: "Experimental and TD-DFT Study of Optical Absorption of Six Explosive Molecules: RDX, HMX, PETN, TNT, TATP, and HMTD", Cooper, J.K., Grant, C.D., Zhang, J.Z., J. Phys. Chem. A, **2013**, online only at the date of this publication.

CHAPTER 1: Characterization of Primary Amine Capped CdSe, ZnSe, and ZnS Quantum Dots by FT-IR: Determination of Surface Bonding Interaction and Identification of Selective Desorption

1.1 Abstract

Surface ligands of semiconductor quantum dots (QDs) critically influence their properties and functionalities. It is of strong interest to understand the structural characteristics of surface ligands and how they interact with the QDs. Three quantum dot (QD) systems (CdSe, ZnSe, and ZnS) with primary aliphatic amine capping ligands were characterized primarily by FT-IR spectroscopy, as well as by NMR, UV-visible, fluorescence spectroscopy, and transmission electron microscopy (TEM). Representative primary amines ranging from 8 to 16 carbons were examined in the vapor phase, KBr pellet, and neat, and were compared to the QD samples. The strongest hydrogen bonding effects of the adsorbed ligands were observed in CdSe QDs with the weakest observed in ZnS QDs. There was an observed splitting of the N-H scissoring mode from 1610 cm^{-1} in the neat sample to 1544 and 1635cm^{-1} when bound to CdSe QDs, which has the largest splitting. The splitting is attributed to amine ligands bound to either Cd or Se surface sites, respectively. The effect of exposure of the QDs dispersed in non-polar medium to methanol as a crashing agent was also examined. In the CdSe system, the Cd-bound scissoring mode disappeared, possibly due to methanol replacing surface cadmium sites. The opposite was observed for ZnSe QDs, in which the Se-bound scissoring mode disappeared. It was concluded that surface coverage and ligand bonding partners could be characterized

by FT-IR, and that selective removal of surface ligands could be achieved through introduction of competitive binding interactions at the surface.

1.2 Introduction

Semiconducting nanomaterials such as nanocrystals (NCs) or quantum dots (QDs) have found useful applications in a wide range of fields from biology to materials science. Their successful development in applications such as fluorescence labeling of bio-molecules,[1] light harvesting in quantum dot sensitized solar cells[2-7] and photo-electrochemical cells,[8-11] as well as next generation lighting technologies, including quantum dot light emitting diodes (QD-LED's)[12-15] and alternating current driven electroluminescence,[16-18] have proven their broad range of usefulness in the scientific community. The unique properties observed in these materials are due to the small size of the particles; this gives rise to quantum confinement effects which are capitalized for tuning emission wavelengths. It is also a consequence of the small size that the particle properties can be dominated by the surface atoms, since the surface-to-volume ratio can be quite high compared to bulk. These surface effects can be influenced by surface defect sites, dangling bonds, or capping ligands; this study addresses the effects of the latter contributor.

Capping ligands are required to impart solubility and stability properties to the particles, as well as to reduce aggregation. The effects of the capping ligand on the structural and electronic properties has been shown to be equally important.[19-24] Capping surface atoms of QDs with an organic ligand increases their coordination number to that of the internal atoms, thereby reducing dangling bond energy states

within the band gap which can act as non-radiative emission centers. The chemical nature of the capping ligands, while not directly involved in the band structure of the semiconductor, can have a substantial effect on the growth characteristics[24-27] and optical properties[22, 25] of the material. Common capping ligands that have been investigated in organic media have included trioctylphosphine oxide (TOPO), phosphonic acids, amines, thiols, and carboxylic acids. Many high temperature organic synthetic techniques utilize metal alkylcarboxylates, and it is often assumed that the resulting capping ligand is the alkylcarboxylic acid. However, some proposed mechanisms for the growth of the crystals indicate the elimination of the carboxylic acid early on,[28] so it is unlikely to be observed at the particle surface unless additional acids are added to the reaction mixture. It is also common for synthetic techniques to include a primary amine as well, and this has been shown to aid in the growth of zinc chalcogenide QD's by activating the zinc carboxylate precursor;[29] it is also known that at high temperature the amine will combine with carboxyl groups to form amides,[30] further eliminating the chance of observing an acid as the resultant ligand. In addition, primary amines have been shown to have greater surface binding energy than carboxylic acids, though lower binding energy compared to TOPO and phosphonic acids by computational studies.[20, 31, 32] However, primary amines have the advantage of more complete surface coverage - which can theoretically reach 100% - over TOPO (30% coverage) due to reduced steric effects.[33, 34] In addition, the added van der Waals force between alkyl chains has been determined for alkyl thiol SAM layers on Au and was found to be between 0.8-1.8

kcal/mol per CH_2 group which may help tip the energy minimization in favor of the primary amine.[35-37] As a result, primary amines have been observed at the surface of our quantum dots even with TOP and TOPO in solution. Therefore, we have focused on the primary amine in this study, as they will likely continue to play a beneficial role in the emerging field of QDs for solid state lighting and other applications.

In this work, three II-VI quantum dot systems were examined by FT-IR spectroscopy in an effort to better understand the local environment of the ligand on the QD surface. Techniques like NMR are of course highly sensitive to local environment; however, the head group of the organic molecule attached to the quantum dot can be difficult or impossible to observe in the ^{1}H NMR due to peak broadening and shifting. While FT-IR is less sensitive to local chemical environment, it has, however, proven a powerful tool in characterization of the bonding between the ligand and the QD.[38] The three QDs studied were CdSe, ZnSe, and ZnS, all of which were capped with a long chain (C8-C18) aliphatic primary amine. The spectra did not appear to depend on the chain length over the range studied. As QD preparations commonly use a crashing step to help clean and isolate the particles from the crude reaction mixture, samples were collected immediately after this step and compared to prior to crashing. The results demonstrate that surface coverage and ligand structure can be characterized by FT-IR, and that selective removal of surface ligands can be achieved through the introduction of competitive binding interactions at the surface.

1.3 Experimental

1.3.1 Synthesis of CdSe-Hexadecylamine Quantum Dots

The CdSe QDs were synthesized under Ar protection using the hot injection method. A 50 mL three-neck round-bottom flask was charged with 10 g ODE and 0.136 g cadmium stearate and was degassed three times to a pressure of 150 mmHg for a total of 30 minutes with purging. The mixture was heated to 90°C where it was degassed again for 10 minutes. The mixture was heated to 300°C where at which point a mixture of 0.039 g Se, 2.5 g TOP, and 0.2 g HDA prepared under N_2 was injected to the stirring cadmium solution. Growth was continued until the exciton had red-shifted to 603 nm, as monitored by UV-vis, for a total reaction time of approximately 6-8 minutes. The mixture was cooled to room temperature where the crude reaction mixture was cleaned with the following procedure.

1.3.2 Synthesis of ZnSe-Hexadecylamine Quantum Dots

The synthesis of the ZnSe QDs was performed under $Ar_{(g)}$ protection using the hot injection method. To begin, 0.06 g zinc stearate with 10 mL ODE was charged in a three-neck round-bottom flask. The mixture was evacuated to 150 mmHg three times for a total of 30 minutes with purging, with an additional evacuation at 90 °C for 15 minutes. The mixture was heated to 300 °C with stirring at which point 0.032 g Se powder dissolved in 0.32 g TBP with 0.15 g HDA and 1 mL ODE was injected rapidly. Growth was continued at 250 °C until the first exciton had shifted to between 400-405 nm, as monitored by UV-vis spectroscopy. The solution was

cooled to room temperature where the QDs were separated from the crude reaction mixture with the reported cleaning procedure.

1.3.3 Synthesis of ZnS-Octadecylamine Quantum Dots

Synthesis of ZnS QDs was performed using the hot injection method under $Ar_{(g)}$ protection. A 50 mL three-neck round-bottom flask was charged with 10 mL ODE and 0.0597 g zinc stearate. The solution was degassed 3 times to 150 mmHg for a total of 30 minutes with purging and then heated to 90 °C and degassed again for 10 minutes to 150 mmHg. The mixture was heated to 300 °C at which point a mixture of 0.013 g sulfur, 0.32 g TBP, and 0.1 g ODA prepared under $N_{2(g)}$ and diluted in 0.6-1 mL ODE was injected with stirring. The temperature was decreased to 250-260 °C where the growth was continued for 6 minutes before the reaction was cooled to room temperature and cleaned as described.

1.3.4 Cleaning of the QDs

To the crude reaction mixture, 2 mL dichloromethane (DCM) mixed in 10 mL methanol was added and mixed thoroughly. Separation of the methanol phase was encouraged through centrifugation and the resulting MeOH layer was discarded. This process was repeated a minimum of three times until this layer was clear. To the resulting solution, acetone was added until the mixture became turbid and the precipitate of the QDs was collected via centrifugation. The crystals were washed two times with acetone and collected by centrifugation, dried under Ar and re-dispersed in a mixture of hexanes and DCM or toluene. This sample was then degassed with $Ar_{(g)}$ and stored for 24 hours prior to sample analysis. The sample was

subsequently sampled for FT-IR, TEM, UV-vis, and PL measurements. The prepared samples dispersed in the non-polar solvent were also crashed using methanol and then centrifuged to collect the final quantum dot precipitate. These were again re-dissolved in toluene or hexanes and sampled for FT-IR analysis.

1.3.5 FT-IR Sample Preparation and Characterization

All KBr pellets were prepared using KBr which was stored at 120°C and were ground in a N_2 glove box to reduce any water and CO_2 contamination. Ground samples were sealed in small dry vials and stored in a desiccator until pressed into a pellet with a pellet press which was also stored in a desiccator. Samples were exposed to atmosphere for no more than 2 minutes before the spectra were collected. Neat samples were collected between NaCl windows prepared in a N_2 glove box and stored under N_2 until analysis. The primary amine samples used as reference were generated by heating the respective compound in a septum-topped vial to 120-140°C for 10 minutes while bubbling N_2. These samples were subsequently stored in a N_2 glove box as well. The gas phase spectrum was collected using a gas cell with NaCl windows by placing a few drops of the heat treated octylamine into the chamber in the N_2 glove box. All spectra were collected at atmospheric pressure under mild heating of the sample cell.

QD samples were dispersed in either hexane or toluene and added drop-wise to the top of a NaCl window under a mild stream of Ar. When a sufficient amount had been added to create the thin film and allowed to dry, the windows were placed into the vacuum transfer chamber of a N_2 glove box and evacuated to ~100mmHg for

5 minutes to remove any remaining solvent. The transfer chamber was subsequently purged with N_2 and the windows were immediately placed into a desiccator for no more than thirty minutes before the spectra were collected.

1.3.6 Instrumentation

Absorption and photoluminescence spectra were collected at room temperature with a Hewlett Packard 845A diode array UV-Visible spectrometer and a Perkin-Elmer Luminescence spectrometer LS50B, respectively. ^{1}H and ^{13}C NMR were collected in d_6-benzene using a Varian Inova 600 NMR. Vibration spectra were recorded with a Perkin-Elmer FTIR spectrometer at a resolution of 4 cm^{-1}. TEM measurements were made using a JEOL JEM-1200EX microscope.

1.4 Results and Discussion

1.4.1 TEM, UV-vis, and Photoluminescence

All QD samples were prepared under similar conditions using organic solvents and the hot injection method as previously described. The samples were characterized using transmission electron microscopy (TEM). **Figure 1** shows representative TEM images of different QD samples. The images indicate the presence of uniform nanospheres with monodispersity within 10% of the mean size distribution in all cases. The sizes of the QDs from TEM images were found to be approximately 4, 6, and 4 nm in diameter for ZnS, ZnSe, and CdSe, respectively. Since the excitonic position in the UV-vis absorption spectrum is dependent on particle size, it can be used to estimate the particle size. For example, for the CdSe

QDs, a diameter of 3.8 nm was calculated based on the first excitonic peak observed in the UV-vis spectrum, which agrees closely with the TEM analysis (4 nm).[39]

Figure 1. Representative TEM images of the three quantum dot systems studied: a) ZnS, b) ZnSe, and c) CdSe. Scale bar: 30 nm.

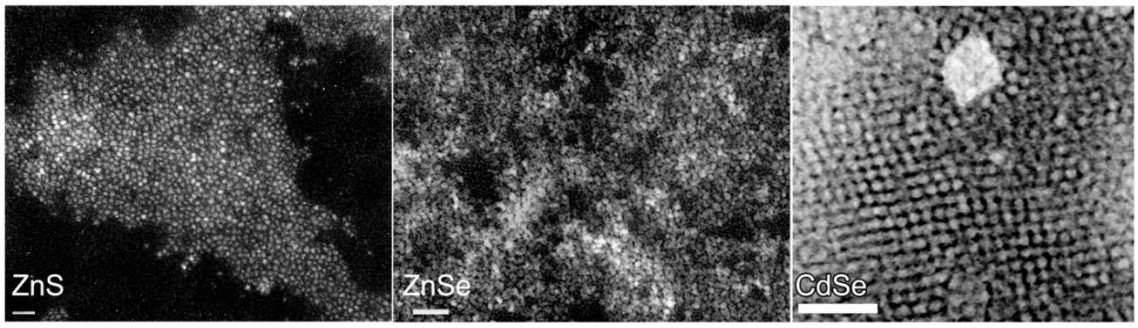

Figure 2 shows UV-vis electronic absorption and photoluminescence spectra of the samples. The spectra are normalized to better compare the different samples. The CdSe QDs show a first exciton at 576 nm (2.15eV). This energy is close to the bandgap energy of the QDs (differing by the small exciton binding energy) and suggests, when compared to the bulk band gap of 1.71eV, that quantum confinement effects are important for the QDs. A Stokes shift of 0.08 eV was observed in the emission peak at 598 nm, which had a full width half maximum (FWHM) of 34 nm. The shift has been implicated due to the electronic fine structure.[40, 41] The narrow peak width is consistent with the monodispersity of the QDs determined by TEM analysis. The strong bandedge PL and weak trap state PL indicate a low density of trap states.[42, 43]

The UV-vis spectrum of ZnSe QDs shows a first exciton peaked at 404 nm (3.07 eV). This is also larger than the bulk band gap of 2.69 eV for ZnSe, again

indicating quantum confinement in the QDs. The PL spectrum shows a major emission band peaked at 427 nm, which had a Stokes shift of 0.17 eV, and a FWHM of 30 nm. There is a weak shoulder to the red of the main band-edge PL band that is apparently due to trap state emission. The narrow PL spectrum and weak trap state PL also suggest monodisperse QDS with low density of trap states.

For the ZnS QD sample, the first exciton appears at about 300 nm (4.13 eV), which is roughly the band gap energy and is larger compared to the bulk band gap energy of ZnS (3.68 eV), indicative of some quantum confinement effect. The PL spectrum exhibits two peaks at 378 and 459 nm which have a Stokes shift of 0.85 and 1.43 eV, respectively. The latter has been previously described as being emission from vacancy states.[44]

Figure 2. Absorption and emission spectra of ZnS (blue/purple), ZnSe (drk green/green), and CdSe (drk red/red).

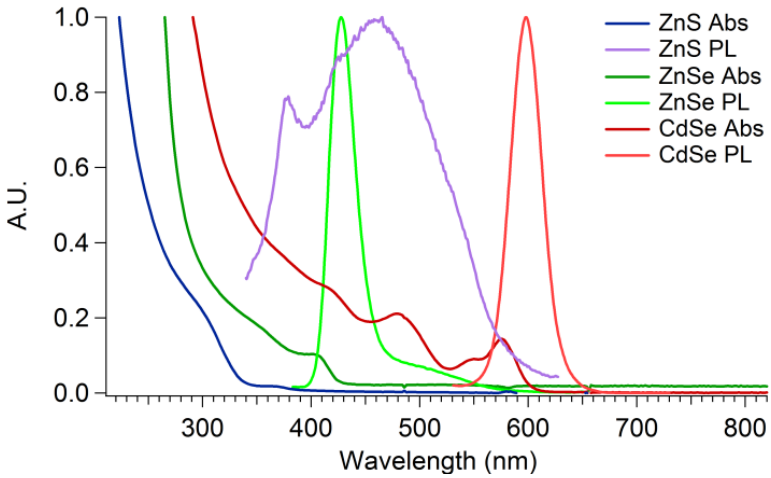

1.4.2 NMR

While FT-IR analysis was sufficient to identify the capping ligand, further confirmation was achieved by ^{1}H and ^{13}C NMR. NMR has been successfully employed in characterization of alkylamines,[21, 45, 46] phosphonic acids,[47] carboxylic acids,[48] TOPO,[49] and thiophenol[50] capping ligands on QD surfaces, to name only a

few. Shown in **Figure 3a** is the proton spectrum of hexadecylamine (color) and CdSe quantum dots with HDA capping ligands both in D_6-Benzene (7.16 ppm).[51] Four peaks were observed at 0.51 ppm(broad-s), 0.92 ppm(t), 1.31(m), and 2.53 ppm(t), corresponding to the amine, methyl, backbone, and α-hydrogens, respectively. In the CdSe sample, however, only two of these peaks remained from the amine; these were observed at 0.93 ppm (broad-triplet), 1.4 ppm (broad feature), with the remaining assigned peaks due to toluene contamination at 2.11 ppm(s) and 7.15 ppm(s). The additional peak at 0.30 ppm(s) is most likely due to a desorbed solution HDA species. The peaks from the α-C and the amine hydrogens interacting with the surface were not observed. The remaining backbone and methyl peaks were broadened which would result from the restricted motion of the surface bound ligands.

The ^{13}C NMR spectrum of the HDA in D_6-benzene (128.06 ppm) is reported as **Figure 3b**. The following peaks were observed and are reported with their carbon number assignments: C1 (42.7 ppm), C2 (34.5), C3 (27.4), C4-14 (30.2), C15 (23.1), and C16 (14.4). The following assignments were made for the QD-HDA sample: C1 (NA), C2 (34.3), C3 (27.3), C4-14 (30.2), C15 (23.2), C16 (14.4). The observation of the C1 carbon could not be resolved due to low S/N. A clear chemical shift was not observed for the HDA on the surface which is consistent with previous reports.[46] The result of the ^{1}H and ^{13}C NMR data confirm the capping ligand to be the aliphatic primary amine from the chemical shift data. The loss of the amine and alpha hydrogens confirm the QD surface interaction while peak broadening in both spectra is from reduced tumbling in solution.[46]

Figure 3. 1H (left) and 13C (right) NMR of hexadecylamine (black) and CdSe QD-hexadecylamine (grey) in d6-benzene at 600 and 150.92 MHz, respectively.

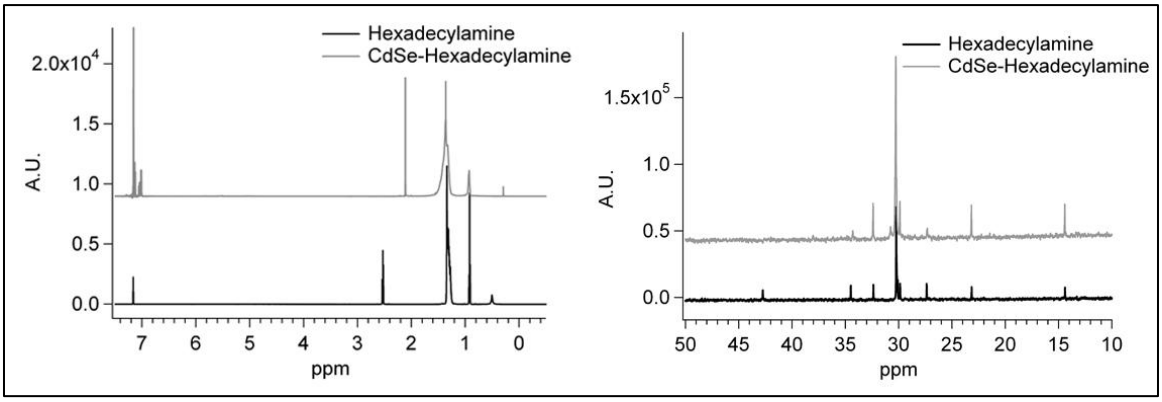

1.4.3 FT-IR of Primary Amines

As it was the goal of this investigation to use the vibrational spectra of primary amines on the surface of QDs to probe their structure and interaction with the QDs, it was necessary to first characterize the amines without the QDs as control experiments. Since the ligands bond through the NH_2 head group, changes in the N-H stretching and bending modes after bonding to the QD surface are expected. Therefore, adequate characterization of hydrogen bonding effects was necessary. To accomplish this, the reference primary amines, octyl- and hexadecyl-, were examined and showed very similar spectral characteristics; however, some variability was observed dependent on the sample preparation. The samples were studied in various forms, including gas phase as well as neat on NaCl and in KBr pellet. The reference amine spectra are shown in **Figure 4** for the full frequency range studied, 450-4000 cm^{-1}. In all spectra, it is not reasonable to compare intensities between samples

because the exact molar concentrations and film thickness were impossible to correct for. Primary amines have been well characterized in the literature,[52-54] however, characterization is discussed here for the purpose of comparing to the quantum dot samples.

Beginning with the gas phase sample, for which octylamine was used (as longer chain amines had insufficient vapor pressures to provide adequate absorption), two weak NH_2 stretching peaks were observed at 3346 and 3316cm^{-1}, corresponding to the anti-symmetric and symmetric modes, respectively. However, free amines are expected to have stretching modes at 3496 and 3401 cm^{-1},[55, 56] while bonded vapor phase ethylamine is expected to have stretching modes at 3344 and 3225 cm^{-1}.[52, 57] The NH_2 scissoring mode was observed at 1623 cm^{-1} as a sharp peak with a FWHM of 13 cm^{-1}. The CH_2 bending modes were at 1467 and 1386 cm^{-1}. The broad peak at 1074 cm^{-1} was due to overlapping C-N stretching modes. Out-of-plane NH_2 bending was observed as a

Figure 4. FT-IR spectrum from 500 to 4000 cm-1 of octylamine in the vapor phase (red), octylamine neat on NaCl (blue), dodecylamine in a KBr pellet (green), and hexadecylcarbamic acid in a KBr pellet (grey).

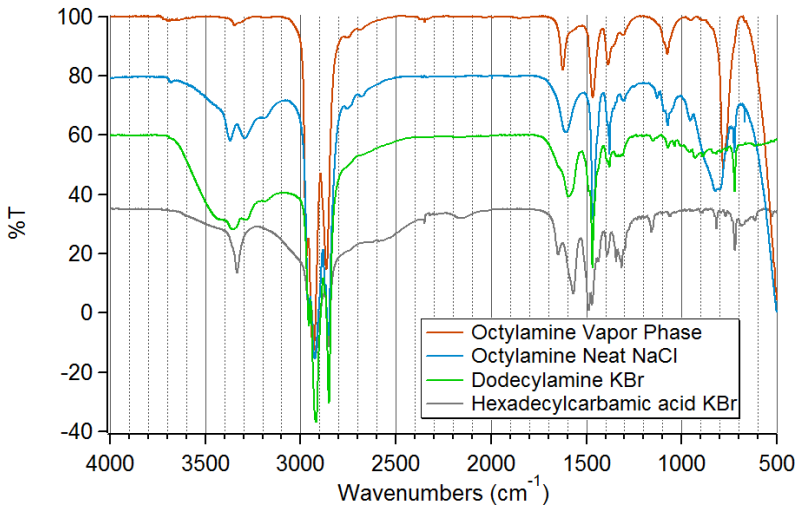

strong absorption at 781 cm^{-1} which eclipsed the backbone rocking mode expected at 722 cm^{-1}.

The neat octylamine spectrum showed a large increase in absorption in the N-H stretching region accompanied by spectral broadening, indicative of hydrogen bonding.[56] Three peaks could be identified at 3370, 3294, and 3191 cm^{-1}, the two former being N-H stretching modes and the latter being the overtone of the NH_2 bending mode interacting with the symmetric stretching mode.[56] The anti-symmetric stretch was frequency up-shifted by 24 cm^{-1} while the symmetric stretch was frequency down-shifted by 22 cm^{-1} compared to that of the vapor phase amine. The NH_2 scissoring peak was located at 1609 cm^{-1}, which was down-shifted by 14 cm^{-1} and was nearly triply broadened compared to the vapor phase sample, with a FWHM of 34 cm^{-1}. The C-H bending and C-N stretching modes were not shifted with respect to the vapor phase sample; however, the NH_2 out-of-plane bending was much broader, weaker, and slightly up-shifted to 814 cm^{-1} allowing for observation of the C-H rocking peak at 723 cm^{-1}.

It should be noted that the hexadecylamine collected from the sample bottle that had been stored unprotected did not show the characteristic group frequencies for a primary amine. It is, however, well known that primary amines will combine with CO_2 to form carbamic acids.[58-60] The FT-IR group frequencies did match a carbamic acid, as it showed a strong sharp peak at 3333 cm^{-1}, which is characteristic of carbamic acid compounds and is due to N-H stretching. This mode was observed over the top of a broad weak O-H stretch centered around the same frequency. Two

peaks were observed at 1648 and 1568 cm^{-1} corresponding to the C=O stretching and NH_2 bending modes, respectively. This sample has therefore been assigned to hexyadecylcarbamic acid however the spectrum of this compound has been occasionally miss-assigned in the literature as a primary amine. Consequentially, the primary amine was regenerated using the technique described in the experimental section. Adequate removal of any carbamic acids in the primary amine sample preparation by elimination of CO_2 via the degassing and heating method was supported by the absence of the sharp 3333 cm^{-1} peak in the N-H stretching region. As peaks were observed in a broad spectral region in the NH_2 scissoring mode and C=O stretching region, the N-H stretch was the only decisive peak for confirming the complete elimination of any carbamic acid.

The hexadecylamine sample, which was ground and pressed in KBr, showed further broadening and shifting of the amine-related peaks. The N-H stretching peaks were further intensified and broadened with what could be identified as three peaks at 3357, 3283, and 3187cm^{-1}. The NH_2 anti-symmetric stretch was again up-shifted by 11cm^{-1}, with respect to the vapor phase amine, while the symmetric stretch was down-shifted by 33cm^{-1}. The NH_2 scissoring mode was further down-shifted to 1592 cm^{-1} and broadened, showing a shoulder at 1642cm^{-1} which has been referred to by Randall *et al*. as "special invariant groups of unknown mode of vibration." It is our suggestion that the broadening and shifting observed in this region due to hydrogen bonding be evidence that the shoulder observed is due to "free" amines within the solid sample matrix. Also, the C-N stretch was weakened even further and the NH_2

out-of-plane stretch slightly up-shifted over the neat sample and was also much diminished with some slight broadening. [61] In summary, hydrogen bonding effects were observed to increase from the vapor, liquid, and solid samples marked by increased NH stretching absorption and down-shifting of the NH scissoring peak with broadening observed in both features.

1.4.4 FT-IR of Amines on Surface of QDs

1.4.4.1 N-H Stretching Region

With the free amines independently characterized, the vibration frequencies of the amines bound to the surface of QDs with emphasis on the changes were observed. The FT-IR spectra of octadecylamine capped QD samples of CdSe, ZnSe, and ZnS are shown in **Figure 5** over the range from 450-4000 cm^{-1}. Spectra were collected before and after crashing with methanol to observe any changes in the spectra. Therefore, there were two spectra measured for each type of QD, one before crashing with methanol and another after and labeled with "MeOH." To help compare the critical NH_2 scissoring region, the expanded spectra from 650-1800 cm^{-1} are shown in **Figure 6**.

Figure 5. FT-IR spectrum from 500-4000 cm-1 of octadecylamine capped QD solid samples taken on NaCl plates before and after crashing with MeOH for CdSe(red/orange), ZnSe (green, light green), and ZnS (blue/ light blue), respectively. Inset: expanded N-H stretching region.

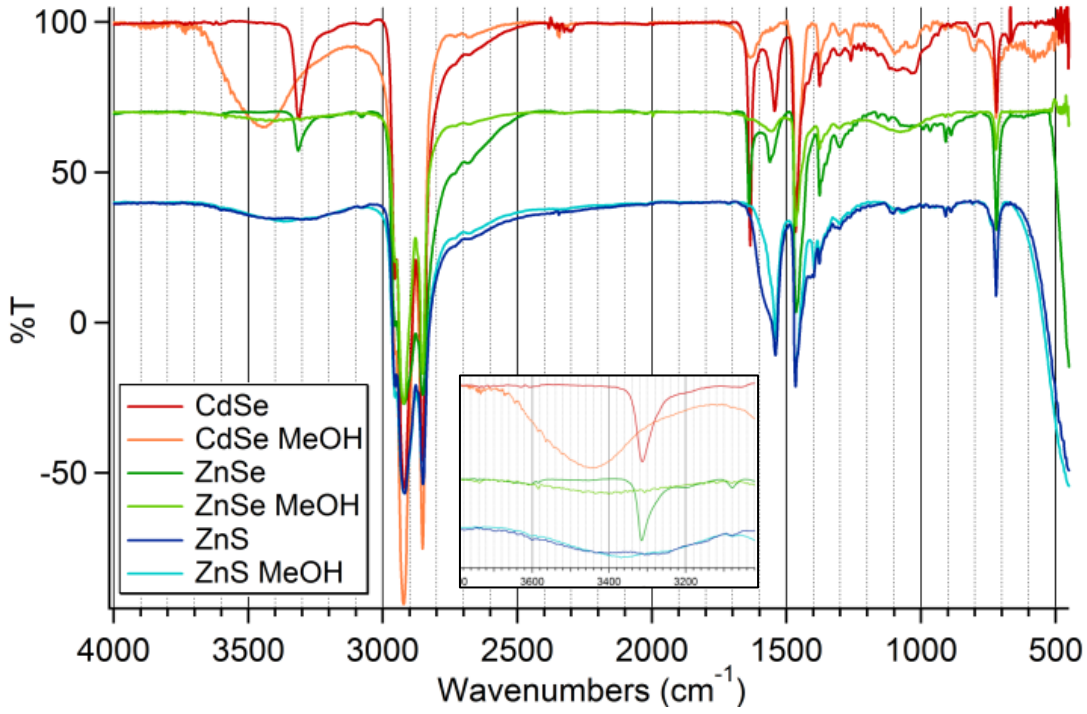

Figure 6. Expanded FT-IR spectrum from 730-1800 cm-1 of octadecylamine capped QD solid samples taken on NaCl plates before and after crashing with MeOH for CdSe(red/orange), ZnSe (green, light green), and ZnS (blue/ light blue), respectively.

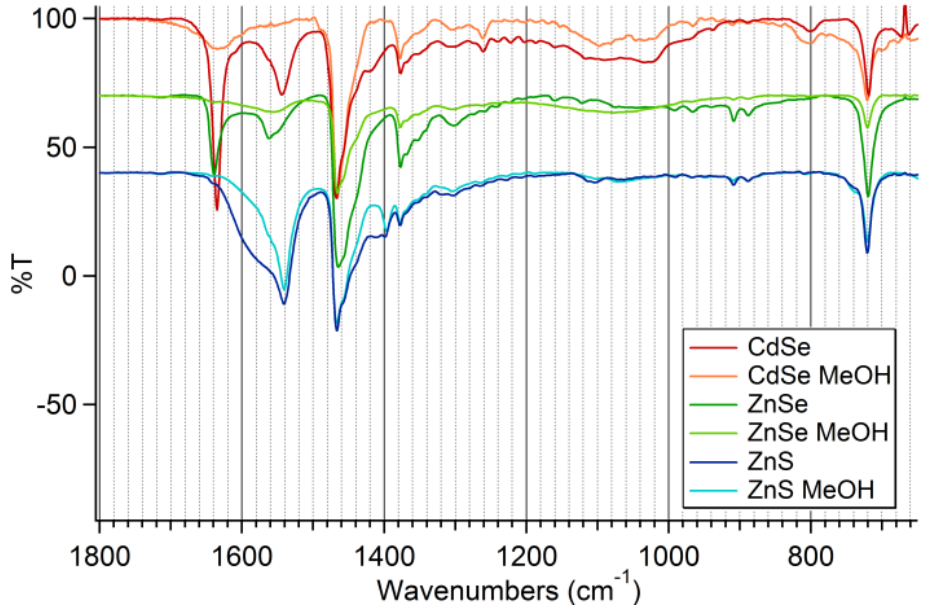

Beginning with the N-H stretching region, two of the QD samples, CdSe and ZnSe, exhibit a similar characteristic in that before washing with MeOH a single, strong, asymmetric low frequency sharp peak was observed at 3314 cm^{-1}. This represents a down-shift of 33 cm^{-1} compared to the vapor phase amine, which implies that the peak is due to the symmetric stretch with the anti-symmetric stretch absent. Due to the magnitude of the shift in all samples of these modes, which was the same in the solid reference amine in KBr, the QD-bound ligands seem to be involved in strong hydrogen bonding and in a solid-like environment. The ZnS sample had a broad feature with two separate peaks at 3409 and 3281 cm^{-1}, indicating the presence of both stretching modes. The reason for the observed differences in this region between the metal selenides (MSe) and the ZnS will be discussed later.

The second harmonic of the NH_2 scissoring interaction with the N-H symmetric stretch also has very low and similar intensity at ~3196 and 3057 cm^{-1}, 3200 and 3078cm^{-1}, and 3155 and 3079cm^{-1} for CdSe, ZnSe, and ZnS, respectively. The two sets of peaks correspond to the two scissoring modes observed in these systems, also to be discussed in a later section.

The spectra after crashing with MeOH showed an up-shifted and broadened NH stretching peak at 3446 and 3413 cm^{-1} for CdSe and ZnSe, respectively, while the ZnS sample showed a slightly down-shifted peak to 3363 cm^{-1}. In the MSe samples, the anti-symmetric stretch became active after crashing, while for ZnS QDs the MeOH crashing step did not have as dramatic an effect. It was, however, not possible to ascertain the exact peak position of the two stretching modes in CdSe and ZnSe due to substantial broadening; whereas for ZnS the peak positions were 3363 and 3262 cm^{-1}. In addition, due to the high intensity of the N-H stretching region in the CdSe sample, it was speculated that strong hydrogen bonding was maintained. Hydrogen bonding is less significant in the ZnSe QDs and very weak for ZnS QDs, based on comparison of the N-H scissoring vs stretching intensities. Also after crashing, one of the two Fermi overtone bands was eliminated in the ZnS sample, leaving the 3079 cm^{-1} peak. As this sample had the least broadening in this region it was the only one in which this effect could be observed.

The combined observations thus far suggest that prior to crashing, the capping ligand head groups were in a highly uniform distribution in a strongly hydrogen-bonded network across the surface in CdSe and ZnSe. This interaction between

ligands would only be possible if they were occupying both metal and chalcogen sites. For example, on the surface, ligands would be too far away from one another when occupying only metal sites to hydrogen bond (CdSe: Cd-Cd d=4.30Å, ZnSe: Zn-Zn d=4.01Å, ZnS: Zn-Zn d=3.82Å)[62]. However, if ligands were also occupying chalcogen sites as well, hydrogen bonding would be much more accessible between ligands (CdSe: Cd-Se d=2.63Å, ZnSe: Zn-Se d=2.45Å, ZnS: Zn-S d=2.34Å)[62]. It has been shown that optimum hydrogen bonding distances between alkylamides is about 3 Å between the N and O and 2 Å between H and O in the N-H···O bond.[63] However, after crashing, desorption of one of the two binding sites took place, and the highly uniform surface was disrupted, resulting in substantial peak broadening. ZnS appears to be the borderline between strong hydrogen bonding with ordered surface of both Zn and S sites occupied and steric interference between neighboring capping ligands on Zn and S sites, where the crystal structure may favor only Zn sites. The implication of these results on the surface bonding scheme will be further discussed later.

1.4.4.2 NH_2 Scissoring Region

For the scissoring region (**Figure 6**), the samples exhibited two medium to strong peaks at 1635 and 1544 cm^{-1} for CdSe, 1639 and 1560cm^{-1} for ZnSe, and 1584 and 1541 cm^{-1} for ZnS. Relative percentages were calculated by fitting these high:low frequency peaks and were found to be 60:40, 50:50, and 50:50 for the CdSe, ZnSe, and ZnS, respectively. After crashing, however, only one of the two peaks remained, the higher frequency for CdSe and the lower frequency for ZnSe and ZnS.

These observations have led to the suggestion that the two amine scissoring peaks were the result of ligands bound either to the metal or the chalcogen and that crashing with methanol removed one of the two ligands. As the CdSe and ZnSe share the higher frequency peak (which is observed at much lower frequencies in ZnS), this peak was assigned to ligands bound to the chalcogen sites while the lower frequency peak was attributed to ligands bound to the metal sites. Therefore, crashing with methanol in the CdSe case removed specifically more Cd-bound ligands. It could be speculated that the origin of the high frequency peak is due to asymmetric NH_3^+ stretching, which has been reported to be at 1630 cm^{-1}. However, this is unlikely as the NH_3^+ group exhibits a symmetric bend as well at 1560 cm^{-1}, which was not observed in the CdSe system after MeOH crashing. It has, however, been shown that the scissoring peak position is sensitive to hydrogen bonding.[64] In addition, there were two Fermi resonance-amplified NH_2 scissoring overtones observed prior to crashing, further supporting our assignment that both of these peaks are due to NH_2 scissoring.

It is therefore reasonable to assume a competitive binding model in which QDs exposed to both primary aliphatic amines and methanol would exhibit competitive surface-site binding in non-polar solvents. Crashing with MeOH could cause desorption of surface ligands by replacing them with methanol; however, in this experiment direct observation of MeOH bound to the QDs could not be detected via FT-IR. It is also possible that during the re-dissolving process ligands were removed from the surface as intermolecular forces between co-aggregated QDs would be

competing with head group binding interactions, which could result in extraction of some ligands from the surface. This could also explain some of the scissoring broadening observed between 1580 and 1600cm^{-1} as these extracted ligands would remain in solution whereas the ones replaced by MeOH would have been decanted. However, the magnitude of the broadening is not proportional to the initial intensity from the two scissoring components, indicating that most of the ligands were removed upon addition of methanol and were subsequently discarded. It is unexpected to observe only Se-bound amines in this experiment after crashing, as Cd sites have been reported to be more stable binding sites.[20] However, there is remaining conflict in the literature in which Se sites have been reported to be more stable.[32] The spectra suggest that the Se-bound ligands remained after crashing. It is, therefore, possible for Se-bound ligands to remain at Se sites if they are stabilized by hydrogen bonding interactions from adjacent Cd bound ligands. If MeOH had replaced surface Cd sites, the Se-bound ligands could still remain adsorbed; however, there is no direct evidence of this to date experimentally or computationally. It is a slightly different situation in the ZnSe case in which the remaining peak after crashing was attributed to the ligand bound to the Zn site, which would suggest that the capping ligand strength with the Se sites in this system is weaker. The same was observed in ZnS in which the Zn sites remained after crashing. In all systems, crashing the particles had the effect of reducing the photoluminescence. This observation further supported the removal of capping ligands from the QD surface.

As discussed previously, the post-crashing N-H stretching intensity in the CdSe system was relatively much stronger than that in ZnSe and ZnS, indicating greater hydrogen bonding in CdSe. This result, combined with the scissoring mode analysis, leads to the implication that the amine bound to Se sites in CdSe after washing did so through hydrogen bonding. As crashing removed chalcogen-bound ligands in ZnSe and ZnS, the hydrogen bonding signal enhancement was reduced since the amine binds through the lone pair to the metal site rather than through hydrogen bonding. If the ligands bound to Se sites in CdSe were oriented toward the Se, the lone pair would be pointed perpendicular to the crystal surface, allowing for hydrogen bonding with adjacent Cd-bound ligands oriented similarly. An example as to how this may look in CdSe on the 0001 Cd-terminated surface is provided in **Figure 7** for clarity, which was simply generated as a suggested model but is not a computationally minimized geometry. It is still unclear how exactly this configuration of ligands would result in activation of only the symmetric stretching mode over the anti-symmetric mode.

Figure 7. Proposed bonding scheme of aliphatic primary amines (Nitrogen: blue) on the 001 surface of CdSe wurtzite crystal as bonded to Se (orange) and Cd (off-white) atoms demonstrating hydrogen bonding interactions between capping ligands at approximately 1.8 Å.

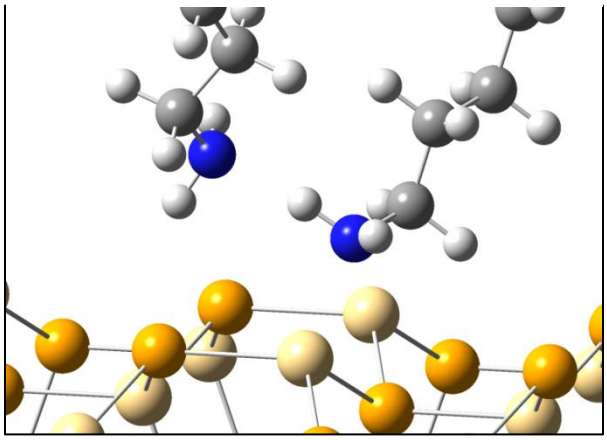

1.4.4.3 Remaining Low Frequency Modes

In all cases, the CH_2 bending and rocking modes appeared to be unaffected by MeOH crashing. However, the C-N stretching mode intensity and shape was inconsistently affected by crashing, though it did not grossly change its frequency. The NH_2 out-of-plane bending was observed at 801 cm^{-1} for CdSe and was unaffected by crashing; however, it was not observed ever in ZnSe or ZnS.

1.5 Conclusion

FT-IR spectroscopy, in conjunction with other experimental techniques, have been utilized to study the structure of aliphatic primary amines ranging from C8-C16 carbon chain lengths on the surface QDs with emphasis on probing their interaction with the QD surface. A sharp N-H stretching peak was observed at 3314 cm^{-1} in the CdSe and ZnSe systems while a splitting of the NH_2 scissoring peak was observed in all three, in which the frequency was dependent on the sample. A difference in the spectra was observed after the QDs were crashed with methanol, a common cleanup step of the synthesis. Here, a substantial broadening of the N-H stretching peak and the elimination of one of the two split NH_2 scissoring peaks was observed. It was concluded that selective removal of either metal or chalcogen associated ligands had been observed during crashing, depending on the sample. The two scissoring modes were assigned to ligands associated with chalcogen and metal sites, respectively. The results demonstrate that FT-IR is a powerful technique for probing surface properties of QDs that are of interest for both basic research and various emerging technologies applications.

1.6 References

(1) Yu, W. W.; Chang, E.; Drezek, R.; Colvin, V. L., *Biochem. Biophys. Res. Commun.* **2006**, 348, 781-786.

(2) Sholin, V.; Breeze, A. J.; Anderson, I. E.; Sahoo, Y.; Reddy, D.; Carter, S. A., *Sol. Energy Mater. Sol. Cells* **2008**, 92, 1706-1711.

(3) Brown, P.; Kamat, P. V., *J. Am. Chem. Soc.* **2008**, 130, 8890-8891.

(4) Kongkanand, A.; Tvrdy, K.; Takechi, K.; Kuno, M.; Kamat, P. V., *J. Am. Chem. Soc.* **2008**, 130, 4007-4015.

(5) Leschkies, K. S.; Divakar, R.; Basu, J.; Enache-Pommer, E.; Boercker, J. E.; Carter, C. B.; Kortshagen, U. R.; Norris, D. J.; Aydil, E. S., *Nano Lett.* **2007**, 7, 1793-1798.

(6) Robel, I. n.; Kuno, M.; Kamat, P. V., *J. Am. Chem. Soc.* **2007**, 129, 4136-4137.

(7) Robel, I. n.; Subramanian, V.; Kuno, M.; Kamat, P. V., *J. Am. Chem. Soc.* **2006**, 128, 2385-2393.

(8) Lee, Y.-L.; Chi, C.-F.; Liau, S.-Y., *Chem. Mater.* **2009**, 22, 922-927.

(9) Hensel, J.; Wang, G.; Li, Y.; Zhang, J. Z., *Nano Lett.* **2010**, 10, 478-483.

(10) Li, Y.; Zhang, J. Z., *Laser & Photonics Reviews* **2010**, 4, 517-528.

(11) Wang, G.; Yang, X.; Qian, F.; Zhang, J. Z.; Li, Y., *Nano Lett.* **2010**, 10, 1088-1092.

(12) Colvin, V. L.; Schlamp, M. C.; Alivisatos, A. P., *Nature* **1994**, 370, 354-357.

(13) Rath, A. K.; Bhaumik, S.; Pal, A. J., *Appl. Phys. Lett.* **2010**, 97.

(14) Sun, Q.; Wang, Y. A.; Li, L. S.; Wang, D.; Zhu, T.; Xu, J.; Yang, C.; Li, Y., *Nat Photon* **2007**, 1, 717.

(15) Tan, Z.; Zhang, F.; Zhu, T.; Xu, J.; Wang, A. Y.; Dixon, J. D.; Li, L.; Zhang, Q.; Mohney, S. E.; Ruzyllo, J., *Nano Lett.* **2007**, 7, 3803.

(16) Manzoor, K.; Vadera, S. R.; Kumar, N.; Kutty, T. R. N., *Appl. Phys. Lett.* **2009**, 84, 284-286.

(17) Wood, V.; Halpert, J. E.; Panzer, M. J.; Bawendi, M. G.; Bulovic, V., *Nano Lett.* **2009**, 9, 2367-2371.

(18) Yang, H.; Holloway, P. H.; Ratna, B. B., *J. Appl. Phys.* **2003**, 93, 586.

(19) Nag, A.; Hazarika, A.; Shanavas, K. V.; Sharma, S. M.; Dasgupta, I.; Sarma, D. D., *J. Phys. Chem. Lett.* **2011**, 706-712.

(20) Schapotschnikow, P.; Hommersom, B.; Vlugt, T. J. H., *J. Phys. Chem. C* **2009**, 113, 12690-12698.

(21) Ji, X.; Copenhaver, D.; Sichmeller, C.; Peng, X., *J. Am. Chem. Soc.* **2008**, 130, 5920-5926.

(22) Nose, K.; Fujita, H.; Omata, T.; Otsuka-Yao-Matsuo, S.; Nakamura, H.; Maeda, H., *J. Lumin.* **2007**, 126, 21-26.

(23) Pokrant, S.; Whaley, K., *Eur. Phys. J. D* **1999**, 6, 255-267.

(24) Pradhan, N.; Reifsnyder, D.; Xie, R.; Aldana, J.; Peng, X., *J. Am. Chem. Soc.* **2007**, 129, 9500-9509.

(25) Jose, R.; Ishikawa, M.; Thavasi, V.; Baba, Y.; Ramakrishna, S., *J. Nanosci. Nanotechnol.* **2008**, 8, 5615-5623.

(26) Zhong, X.; Feng, Y.; Zhang, Y., *J. Phys. Chem. C* **2007**, 111, 526-531.

(27) Nag, A.; Hazarika, A.; Shanavas, K. V.; Sharma, S. M.; Dasgupta, I.; Sarma, D. D., *J. Phys. Chem. Lett.* **2011**, 706-712.

(28) Liu, H.; Owen, J. S.; Alivisatos, A. P., *J. Am. Chem. Soc.* **2007**, 129, 305-312.

(29) Li, L. S.; Pradhan, N.; Wang, Y.; Peng, X., *Nano Lett.* **2004**, 4, 2261-2264.

(30) Solomons, T. W. G.; Fryhle, C. B., *Organic Chemistry*. 8th ed.; John Wiley & Sons, Inc.: Hoboken, NJ, 2004.

(31) Rempel, J. Y.; Trout, B. L.; Bawendi, M. G.; Jensen, K. F., *J. Phys. Chem. B* **2006**, 110, 18007-18016.

(32) Puzder, A.; Williamson, A. J.; Zaitseva, N.; Galli, G., *Nano Lett.* **2004**, 4, 2361-2365.

(33) Green, M., *J. Mater. Chem.* **2010**, 20, 5797-5809.

(34) Bullen, C.; Mulvaney, P., *Langmuir* **2006**, 22, 3007-3013.

(35) Lim, I. I. S.; Maye, M. M.; Luo, J.; Zhong, C.-J., *J. Phys. Chem. B* **2005**, 109, 2578-2583.

(36) Nuzzo, R. G.; Dubois, L. H.; Allara, D. L., *J. Am. Chem. Soc.* **1990**, 112, 558-569.

(37) Salem, L., *J. Chem. Phys.* **1962**, 37, 2100.

(38) von Holt, B.; Kudera, S.; Weiss, A.; Schrader, T. E.; Manna, L.; Parak, W. J.; Braun, M., *J. Mater. Chem.* **2008**, 18, 2728-2732.

(39) Jasieniak, J.; Smith, L.; Embden, J. v.; Mulvaney, P.; Califano, M., *J. Phys. Chem. C* **2009**, 113, 19468-19474.

(40) Efros, A. L.; Rosen, M.; Kuno, M.; Nirmal, M.; Norris, D. J.; Bawendi, M., *Physical Review B* **1996**, 54, 4843.

(41) Kambhampati, P., *Acc. Chem. Res.* **2011**, 44, 1-13.

(42) Roberti, T. W.; Cherepy, N. J.; Zhang, J. Z., *J. Chem. Phys.* **1998**, 108, 2143.

(43) Zhang, J. Z., *J. Phys. Chem. B* **2000**, 104, 7239-7253.

(44) Wageh, S.; Ling, Z. S.; Xu-Rong, X., *J. Cryst. Growth* **2003**, 255, 332-337.

(45) Hassinen, A.; Moreels, I.; de Mello Donega , C.; Martins, J. C.; Hens, Z., *J. Phys. Chem. Lett.* **2010**, 1, 2577-2581.

(46) Berrettini, M. G.; Braun, G.; Hu, J. G.; Strouse, G. F., *J. Am. Chem. Soc.* **2004**, 126, 7063-7070.

(47) Gomes, R.; Hassinen, A.; Szczygiel, A.; Zhao, Q.; Vantomme, A.; Martins, J. C.; Hens, Z., *J. Phys. Chem. Lett.* **2011**, 2, 145-152.

(48) Fritzinger, B.; Capek, R. K.; Lambert, K.; Martins, J. C.; Hens, Z., *J. Am. Chem. Soc.* **2010**, 664.

(49) Ratcliffe, C. I.; Yu, K.; Ripmeester, J. A.; Badruz Zaman, M.; Badarau, C.; Singh, S., *Phys. Chem. Chem. Phys.* **2006**, 8, 3510-3519.

(50) Sachleben, J. R.; Colvin, V.; Emsley, L.; Wooten, E. W.; Alivisatos, A. P., *J. Phys. Chem. B* **1998**, 102, 10117-10128.

(51) Gottlieb, H. E.; Kotlyar, V.; Nudelman, A., *J. Org. Chem.* **1997**, 62, 7512-7515.

(52) Segal, L.; Eggerton, F. V., *Appl. Spectrosc.* **1961**, 15, 112-116.

(53) Vollhardt, D.; Wittig, M.; Maulhardt, H.; Kunath, D., *Colloid & Polymer Sci* **1984**, 262, 574-578.

(54) Vollhardt, D.; Wittig, M.; Petrov, J. G.; Malewski, G., *J. Colloid Interface Sci.* **1985**, 106, 28-32.

(55) Jones, R. N.; Sandorfy, C., *Chemical Applications of Spectroscopy*. W. West, Ed., Interscience: N.Y., 1956; p 247-580.

(56) Silverstein, R. M.; Webster, F. X.; Kiemle, D. J., *Spectrometric Identification of Organic Compounds*. 7th ed.; John Wiley & Sons, Inc.: Danvers, 2005; p 512.

(57) Pierson, R. H.; Fletcher, A. N.; Gantz, E. S. C., *Anal. Chem.* **1956**, 28, 1218-1239.

(58) Dijkstra, Z. J.; Doornbos, A. R.; Weyten, H.; Ernsting, J. M.; Elsevier, C. J.; Keurentjes, J. T. F., *J. Supercrit. Fluids* **2007**, 41, 109-114.

(59) George, M.; Weiss, R. G., *J. Am. Chem. Soc.* **2001**, 123, 10393-10394.

(60) Nyquist, R. A., *Spectrochimica Acta* **1973**, 29A, 1635-1641.

(61) Randall, H. M.; Fowler, R. G.; Fuson, N.; Dangl, J. R., *Infrared Determination of Organic Structures*. D. Van Nostrand Company, Inc.: N.Y., 1949.

(62) West, A. R., *Basic Solid State Chemistry*. Second ed.; John Wiley & Xons, LTD: W. Sussex, England, 1999.

(63) Bhinde, T.; Clarke, S. M.; Phillips, T. K.; Arnold, T.; Parker, J. E., *Langmuir* **2010**, 26, 8201-8206.

(64) Wallwork, M. L.; Smith, D. A.; Zhang, J.; Kirkham, J.; Robinson, C., *Langmuir* **2001**, 17, 1126-1131.

CHAPTER 2: Ultrafast charge carrier dynamics and photoelectrochemical properties of ZnO nanowires decorated with Au nanoparticles

2.1 Abstract

This study was designed to examine the possible photosensitization effect of zinc oxide (ZnO) nanowires (NWs) by Au nanoparticles (AuNPs) by directly monitoring the charge carrier lifetime in AuNP-decorated ZnO NWs. ZnO-Au nanocomposite structures showed reduced photocurrent compared to pristine ZnO NWs due to the combined effect of ZnO etching during the AuNPs growth and competitive absorption/scattering effects from AuNPs of incident UV photons. Ultrafast transient pump-probe spectroscopy was utilized to characterize the charge carrier dynamics. The bleach recovery of ZnO indicates electron-hole recombination on the 150 ps time scale attributed to shallow donor recombination. The AuNP-decorated ZnO NWs exhibit a fast decay of 3 ps in addition to the decays observed for ZnO NWs. This fast decay is similar to the hot electron relaxation lifetime observed for AuNPs in solution. Overall, the dynamics features for AuNP-decorated ZnO NWs appear as a simple sum of those from AuNPs and ZnO NWs alone. There is no evidence of photosensitization of the ZnO NWs by AuNPs investigated in this study.

2.2 Introduction

Seeking renewable energy sources has driven interest in several research fields, one of which is in the use of metal oxide (MO) semiconductors for solar-driven water splitting.[1] The advances in nanoscience have resulted in tunable

structural and electronic properties of MO materials to better suit the demands for photoelectrodes. One material of increasing interest is ZnO for several reasons including: wide-ranging options for shape control,[2] high electron mobility, abundance, non-toxic, and inexpensive cost. One dimensional (1D) ZnO nanowires are particularly interesting as they provide not only large surface area but also excellent vectorial charge carrier transport along nanowire growth axis.

While ZnO offer many benefits, it is a wide bandgap semiconductor (3.37 eV) which limits light absorption in the visible. There have been many studies aimed at extending the absorption range of such wide band-gap MOs into the visible including: sensitization with dyes,[3] quantum dots,[4-5] or doping.[6] Another approach suggested recently has been the use of noble metal nanoparticles to extend the absorption range. By using the size- and shape-tunable surface plasmon resonance (SPR) of metal nanoparticles, it is possible to shift the absorption range of these structures from the UV to the near IR.[7] An additional benefit to using noble metal nanoparticles could improve stability over organic dyes. A recent report showed that CdSe QD sensitized Au/TiO_2 hybrid films had improved PEC performance as compared to CdSe-TiO_2 while the Au/TiO_2 had reduced performance.[8] The performance enhancement was attributed to increased light absorption from the CdSe due to scattering by the AuNPs. The performance reduction in the Au/TiO_2 system was found to be due to electron trapping from the Au. There have been other reports which have claimed sensitization effects by the Au *via* transference of photoexcited electrons to the conduction band (CB) of the MO.[9-10] Other reports suggest that AuNPs facilitate charge separation by

trapping excited electrons to minimize recombination in the MO.[11] These studies suggest that the effect of AuNPs is closely related to the coordination environment and the experimental conditions. To better understand the role of AuNPs in the metal-semiconductor composite structure for water splitting, we managed to probe the excited state dynamics of the ZnO NWs both with and without decoration by AuNPs. The results will provide direct evidence for the role of AuNPs as a quencher or sensitizer. Carrier trapping would have the effect of shortening the ZnO lifetime while sensitization with AuNPs would inject electrons into ZnO and result in shorter hot electron lifetime in AuNPs or longer electron lifetime for ZnO.

We observed that the charge carrier dynamics of ZnO NWs and AuNPs act independently and no sensitization effects could be determined. From these results, AuNPs alone do not appear function as photosensitizers for ZnO.

2.3 Experimental

2.3.1 Synthesis

2.3.1.1 Synthesis of ZnO NW arrays

ZnO NWs were grown on a ZnO nanoparticle seeded FTO substrate (Hartford Glass Company Inc.) using a hydrothermal method reported previously.[12] 5 mM zinc acetate in ethanol was deposited drop-wise (2 drops) onto FTO substrate and air dried. This step was repeated five times following by annealing at 350 °C for 30 minutes. The zinc acetate deposition and annealing processes were carried out twice to ensure a uniform coating of ZnO nanocrystals on the FTO substrate. This substrate was placed into a Teflon-lined stainless steel autoclave, filled with 20 mL aqueous

solution containing 0.05 M zinc nitrate and 0.05 M hexamethylenetetramine. The sealed autoclave was heated in an electric oven at 90 °C for 6 hours. A uniform white film was coated on the FTO substrate. It was rinsed with deionized water and air dried. Finally, the sample was annealed in air at 550 °C for 3 hours to increase the crystallinity of ZnO nanowires and improve their contact to the substrate.

2.3.1.2 Gold nanoparticle synthesis

Gold nanoparticles were grown on ZnO nanowire surfaces using a hydrothermal method reported previously.[10] FTO substrate coated with ZnO nanowires was placed into a Teflon-lined stainless steel autoclave filled with 10 mL of 1 mM chloroauric acid ($HAuCl_4$) solution with a pH range of 7 and 8, adjusted by sodium citrate ($Na_3C_6H_5O_7 \cdot 3H_2O$). The sealed autoclave was heated in an electric oven at 120 °C for 1 hour. Finally, Au-attached ZnO NW array films were rinsed with deionized water and air dried.

2.3.2 Instrumentation

2.3.2.1 UV-vis and photoluminescence spectroscopy

Absorption and photoluminescence (PL) spectra were collected at room temperature with a Hewlett Packard 8452A diode array UV-Visible spectrometer with a spectral resolution of 2 nm and a Jobin Yuon Horiba FluoroMax-3 fluorometer. Fluorescence measurements were collected at room temperature on the solid substrates at 45˚ from both the excitation and emission windows with the excitation wavelength 340±5nm.

2.3.2.2 Microscopy

Scanning electron microscopy (SEM) was conducted using a FEI Quanta 3D FEG Dualbeam microscope. Histograms were created by measuring a minimum of 100 structures of interest using the ImageJ software package.[13]

2.3.2.3 Femtosecond laser and transient absorption measurement

The details of TA laser system have been previously described.[14] Briefly, <150 fs 1mJ pulses centered at 795 nm were split to a optical parametric amplifier (OPA) and sapphire crystal. Samples were excited with 360 nm and 450 nm light at 220 nJ/pulse perpendicular to the film surface. The white light continuum (WLC), ranging from 430-800 nm, interrogated the sample and was monitored by a CCD detector where 500 pulses were averaged for each data point. A forward and reverse scan was collected and averaged resulting in 1000 averages per data point. The delay stage allowed for generation of a 1000 ps delay with temporal resolution of 10 fs. The decay traces were verified to ensure a linear response with excitation power.

2.3.2.4 Fabrication of NW photoanodes and PEC measurement

NW arrays were fashioned into photoanodes by soldering a copper wire onto a bare portion of FTO substrate. The substrate was then sealed on all edges with epoxy resin except for a working area of *c.a.* 0.15 cm^2. All PEC measurements were carried out in a three-electrode electrochemical cell, with a coiled Pt wire as a counter electrode and an Ag/AgCl electrode as a reference. The electrolyte was a 0.5 M Na_2SO_4 aqueous solution with a pH of 7. Linear sweep voltammograms were measured by a CHI 660D electrochemical station under simulated sunlight with a 150

W xenon lamp (Newport 6255) coupled with an AM 1.5 global filter (Newport 81094). All measurements were conducted with front side illumination.

2.4 Results and Discussion

2.4.1 Electron microscopy

SEM images show that the as-grown ZnO NWs are uniform and vertically aligned with length of 1800±300 nm, and a diameter of 75±22 nm (**Figure 1**), and with uniform thickness and hexagonal morphology. The AuNPs grown on ZnO NWs samples (ZnO-Au) appear to have a random distribution around the circumference of the wires. The AuNP average size was measured to be 22±3 nm and appeared as fully formed spheres with little deformation at the interface of the Au and ZnO. The average ZnO NW diameter in this sample is slightly shrunk to 60±20 nm due to the Au formation reaction with the $HAuCl_4$ solution. Additionally, the wire morphology became conically shaped which is indicative of etching.

Figure 1. SEM images and histograms of the two samples: A) ZnO, B) ZnO-Au.

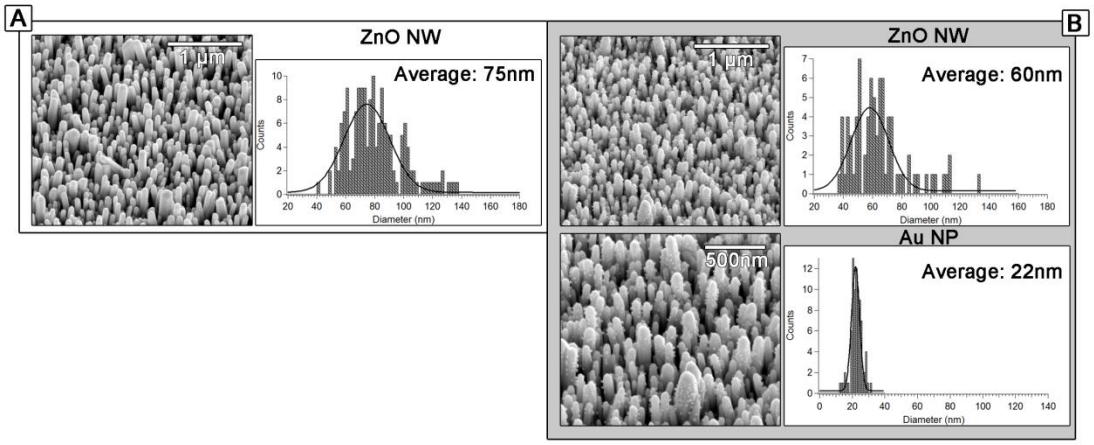

2.4.2 Optical Spectroscopy

2.4.2.1 UV-Vis

The UV-Vis spectra of the two samples studied had very similar characteristics dominated by absorption and scattering, as shown in **Figure 2**. While band-edge absorption for ZnO with a bandgap of 3.37eV was expected to occur about 370 nm, this feature is overwhelmed by the large amount of scattering due to the large physical features of the sample. The monotonic increase in intensity towards shorter wavelength is consistent with Rayleigh scattering. The spectrum of the ZnO-Au sample has a distinguishable shoulder at 527 nm, attributed to SPR of the AuNPs, and

Figure 2: UV-Vis spectrum and digital images of ZnO (blue) and ZnO-Au (red).

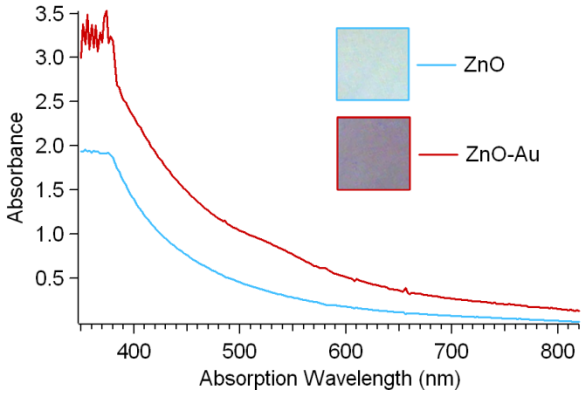

increased absorbance across the entire wavelength range by a factor of about 1.6, likely due to increased light absorption and scattering from the AuNPs. Images of the two samples are shown in the inset of **Figure 2**.

2.4.2.2 Photoluminescence

The PL spectra of the two samples studied are shown in **Figure 3A** and **3B** presented "as-collected" and normalized to the maximum, respectively. The most notable feature is the near band-edge emission between 370-390 nm for the samples. The peak is at 387 nm (3.20 eV) for ZnO and 385 nm (3.22 eV) for ZnO-Au. These features have been attributed to donor recombination in ZnO.[15] The ZnO and ZnO-Au samples had essentially identical spectra, upon normalization, with the exception of a dip in intensity centered about 524 nm which is attributed to re-absorption by the AuNPs. Due to the difference in absorption/scattering between the samples, we attribute the decreased emission in the ZnO-Au to re-absorption and increased scattering by AuNPs over the UV region as well. This

Figure 3: A) Fluorescence spectrum taken at 23°C of ZnO (blue) and ZnO-Au (red), "as-collected." B) Normalized fluorescence spectrum of the same samples. Excitation wavelength: 340nm.

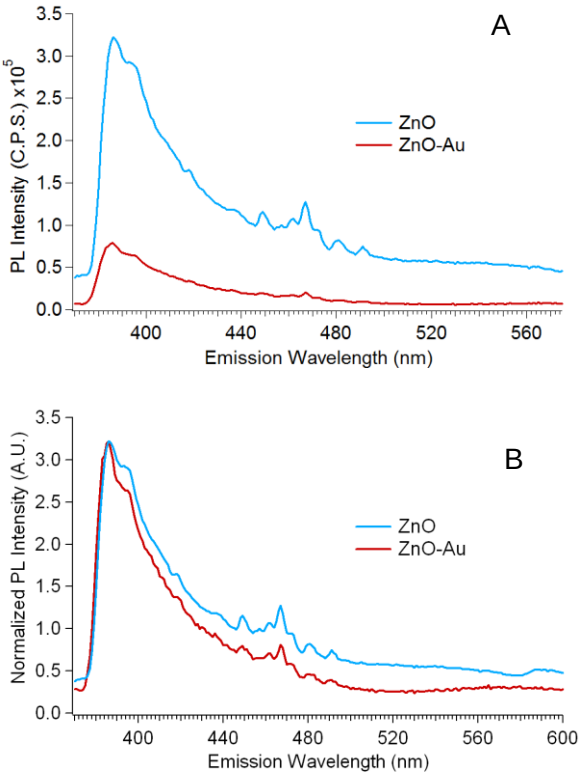

assignment is supported by observations made in the transient absorption studies to be discussed later. In addition, both samples show some green emission centered at 550 nm which has been previously described due to neutral oxygen vacancies (V_O);[16] however, this feature had a very low intensity as compared to the bluer feature.

2.4.3 Photoelectrochemical Water Splitting

The linear sweep voltammograms for the pristine ZnO NW arrays and ZnO decorated with AuNPs are illustrated in **Figure 4**. In comparison to pristine ZnO, ZnO-Au show a dramatic decrease in photocurrent density at applied potentials above 0.6 V vs. RHE. Based on the morphology change observed by SEM, the reduced photocurrent for the ZnO-Au sample could be attributed to decreased available UV photons for absorption by ZnO due to the surface-attached AuNPs as well as the reduced volume of ZnO NWs due to the etching effect of acidic $HAuCl_4$. The reduced photocurrent in this type of system as observed in this work is consistent with our previous studies.[8]

Figure 4: Linear sweep voltammograms collected for ZnO (blue) and ZnO-Au (red) in 0.5 M Na_2SO_4 electrolyte (pH = 7) under simulated sunlight illumination at 100 mW/cm^2. Dark scans are also reported with the same coloring but dashed lines.

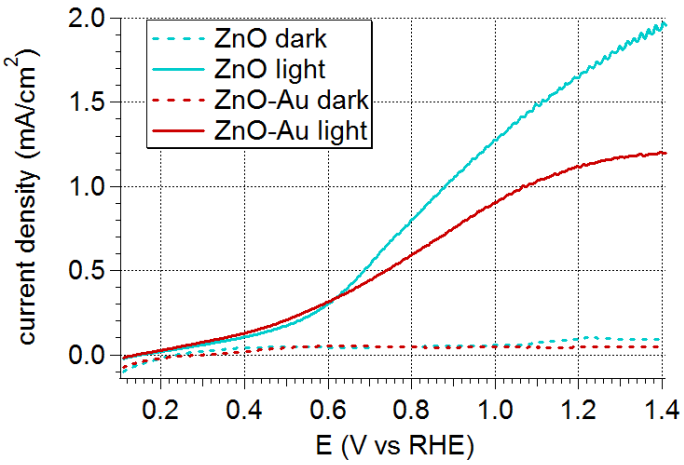

2.4.4 Transient Absorption Spectroscopy

In an effort to understand the electron dynamics in the ZnO-AuNP composite and if AuNPs can sensitize ZnO, we used transient absorption (TA) pump probe

Figure 5. Contour plots of TA data of ZnO (top-white background), ZnO-Au (middle-gray background), and AuNP in H_2O (bottom-white background) over the 50 and 500ps delay ranges as pumped with 450nm (turquoise line) and 360nm (blue line). Each plot is of wavelength (nm), delay (ps), and TA (mOD) color as reported on the right of each figure; see top left figure for units.

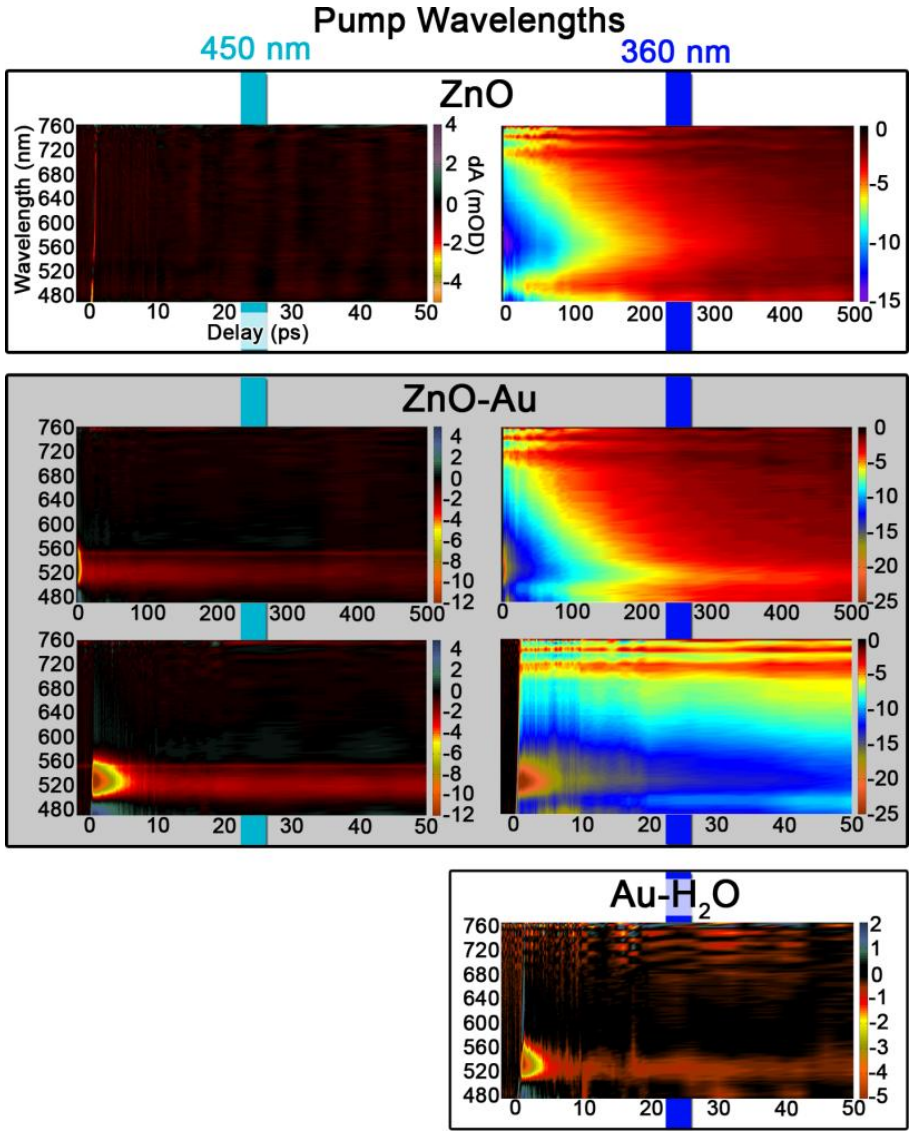

spectroscopy to determine the exited state lifetimes of the composite and constituent materials. The TA system is equipped with a tunable pump source and white light probe (420-800 nm) making it is possible to excite the AuNP only (450 nm) or to excite both materials at the same time (360 nm).

The transient time profiles for the different samples and two excitation wavelengths are shown as contour plots in **Figure 5.** The TA signals with intensity indicated by color are plotted as a function of probe wavelength and delay time between the pump and probe pulses. The pump wavelengths used are indicated at the top of each row (450 nm and 360 nm).

As a control experiment, the decant from the synthesis of the ZnO-Au sample was collected which contained a suspension of only the AuNPs in water. This sample, when excited with 360 nm pump (**Figure 5**, bottom right), displays a very fast component with a time constant of 2.3±0.4 ps and a small amplitude slow decay component with a lifetime of 360±70 ps. The feature is Gaussian shaped and centered at around 525 nm which is strictly due to the SPR from AuNPs. The fast component is due to electron-phonon coupling and the slower decay is due to phonon relaxation.[17]

The TA spectrum of ZnO following 360 nm excitation (**Figure 5**, top right) has its highest intensity toward the blue and tails to lower intensity toward the red. This transient bleach feature mostly decays within 250 ps however a longer lived component was observed extending through the 500 ps time window. Under 450 nm excitation, the signal is entirely absent indicating that the transient bleach observed

with the 360 nm pump is due to excitons. For a typical sample, a bleach signal indicates reduced ground state absorption under pumped perturbation. While ZnO does not absorb over our white light range, it is important to note that optical density is the sum of both absorption and scattering. Inspection of the UV-Vis spectrum in **Figure 1** indicates that the ZnO NW sample scatters strongly. The origin of the bleach signal would therefore imply that there was less scattering under pump pulse excitation, which would result in more probe light reaching the detector, making the differential absorption negative. In order for less scattering to occur, the refractive index of the material would have increased while electrons were in the excited state following photoexcitation. The excited state electrons effectively increase the permittivity of the material thereby increasing the refractive index.[18] While increased permittivity under UV-illumination of ZnO nanowires has been reported[19], it has not yet been used to characterize the lifetime of the material with this method, to the best of our knowledge. The monotonic increase in intensity towards shorter wavelengths, as observed in **Figure 5**, supports this assignment.

The ZnO-Au sample under 450 nm pump (**Figure 5**, middle panel top left) has a very weak longer lived component centered around 525 nm, as can be observed in the 500 ps time window, with a much faster and intense feature which is only seen at the very beginning of the TA spectrum. The expanded time domain of this spectrum, shows that this feature is very fast (3-4ps) and is Gaussian-shaped centered around 525 nm. The same feature can be seen in the 360 nm pump data. The longer component appears in the 500 ps time window centered around 525 nm as a pointed

streak feature on-top of a feature that mirrors the ZnO signal. There is a fast component observed in the 50 ps window which has the same features as those observed in the 450 nm pump plot. We attribute the fastest Gaussian feature to the AuNP electron-phonon coupling.

The ZnO-Au sample under 450 nm pump, therefore, has transient bleach signal from the AuNPs only. As a result it is clear that they do not result in any signal that can be attributed to electron injection into the CB of ZnO. In addition, while both materials are excited in the ZnO-Au sample with the 360 nm pump, there does not appear to be any changes in the transient decay profiles as compared to the ZnO sample alone. These results also suggest that excited electrons in the ZnO are not affected by the AuNPs, as the ZnO sample was expected to have a shortened lifetime if the excited electrons could decay through a AuNP pathway or AuNP induced trap states.

To make it easier to obtain time constants of the lifetimes, we plotted the TA signal as a function of time for a particular probe wavelength. For example, the TA signal with the 524 nm probe wavelength is shown in **Figure 6**. This particular wavelength was selected as it illustrates the maximum bleach signal for the Au yet also contains the bleach recovery signal for the ZnO. All the samples characterized have pulse width limited rise times. The AuNPs alone in H_2O, shown in a 50 ps window only, have a very fast initial decay with an incomplete return to baseline. Examination of the ZnO decay plot shows a single exponential bleach recovery which has a small amplitude longer component that manifests as an incomplete return to

baseline within the examined time window. The ZnO-Au under 450 nm pump has a very fast initial decay which also has an additional component which is slow to return to baseline. The same sample under 360 nm excitation appears as the sum of the ZnO-Au (450 nm) and the ZnO (360 nm) decays with a very fast component which decays to a single exponential followed by an additional low amplitude component which is much slower. Furthermore, the full time window (**Figure 6**, left panel) shows the ZnO and ZnO-Au bleach recoveries are identical. This would not be expected if the ZnO electrons could decay through AuNP pathways which would shorten the ZnO lifetime. This indicates is that there is a lack of interaction or charge transfer between the two materials; as a result, the charge carriers in both act independently from one another.

Figure 6: Transient bleach recovery traces of the 524 nm probe of ZnO pump 360 nm (blue triangle), ZnO-Au pump 360 nm (red cross), ZnO-Au pump 450 nm (purple circle), Au in water (Au-H_2O) pump 360 nm (yellow square).

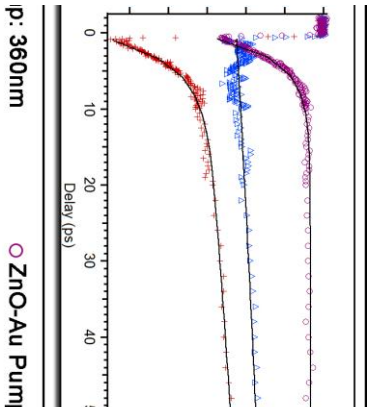

To better understand the lifetime of these components, the decay traces were fit with single or double exponentials with an offset to account for the slowest unresolved component. The fit results are shown as black lines in **Figure 6** and the time constants and amplitudes are reported in **Table 1**. The fit results show that under 360 nm pump the Au-H_2O could be fit with a double exponential with a time constant of 2.3±0.4 ps and 360±70 ps, the ZnO sample could be fit with a single exponential with time a time constant of 160±20 ps, the ZnO-Au was fit with a double exponential with time constants of 3.5±0.5 ps and 150±20 ps. The ZnO-Au pumped with 450 nm was fit with a single exponential with time constant of 3.2±0.5 ps.

Table 1: Fitting results of the ZnO, ZnO-Au, and Au-H_2O 524 nm probe showing the pump wavelength, amplitude (A), and lifetime (τ).

Sample	Pump (nm)	Probe (nm)	A_1	τ_1 (ps)	A_2	τ_2 (ps)
ZnO	360	524			-10	160 (20)
	450	524				
ZnO-Au	360	524	-15	3.5 (0.5)	-13	150 (20)
	450	524	-15	3.2 (0.5)		
Au-H2O	360	524	-8	2.3 (0.4)	-6	360 (70)

The ZnO components are consistent with other observations, however assignments of these components are varied.[20-22] Charge carrier cooling is reported to be <200 fs[23] and typical observations of the electron-hole plasma (EHP) are within the first few ps,[20, 24-25] while green trap state emission due to V_O is reported in the μs range.[16, 26-27] Radiative recombination has been reported to be single exponential with a lifetime of 259 ps at 2K from the Γ_5 free excitons.[28] As the pump power used in this experiment was low and generated a linear relationship between power and signal intensity, we attribute the observed component to shallow donor bound exciton recombination. This recombination lifetime was identical between the ZnO and ZnO-Au sample, considering error. Therefore, the addition of AuNPs on the surface of the NWs did not affect the ZnO lifetime by introducing trap states or charge transfer mechanisms to the exciton recombination.

The hot electron lifetime of the AuNPs on the ZnO NWs under 360 and 450 nm are identical within the error of measurement. However, it is slightly longer for the ZnO-Au sample than was the AuNPs in water, 3.2±0.5ps *vs.* 2.3±0.4ps. This is likely due to the difference in the dielectric constant between ZnO/air and water. These results confirm the assertion that the reduced photocurrent seen in the ZnO-Au sample is not due to electron trapping by the AuNPs but rather due to competitive absorption and increased back scattering of UV photons by the AuNPs.

2.5 Conclusion

We have characterized pristine ZnO NWs and ZnO NWs decorated with AuNPs with the intention of understand if AuNP could act as a sensitizer for the ZnO in the

visible. From the increased absorption in the UV-Vis spectra we concluded that the AuNPs increase the scattering and absorption. The PL spectra showed reduced emission with the AuNPs which we attributed to re-absorption and scattering. The PEC data showed decreased photocurrent in the AuNP-decorated ZnO NW sample as compared to pristine ZnO NWs. Time dependent bleach recovery the ZnO-Au sample under 360 nm excitation is essentially a simple sum of the results of the ZnO-Au and ZnO samples. The fitting results confirmed there was no effect on the lifetime of ZnO NWs due to the presence of AuNPs and visa versa. We therefore conclude that the reduced PEC performance in the ZnO-Au sample was due to increased scattering/absorption of charge carrier generating photons by the AuNPs. The results therefore do not provide any indication that AuNPs sensitize ZnO under the conditions used in our study. Further research is clearly needed to determine if photosensitization of MO with metal nanoparticles if possible and, if yes, what the necessary conditions are.

2.6 References

[1] Yang, X., Wolcott, A., Wang, G., Sobo, A., Fitzmorris, R. C., Qian, F., Zhang, J. Z.; Li, Y., "Nitrogen-doped ZnO nanowire arrays for photoelectrochemical water splitting," Nano Lett. 9(6), 2331-2336 (2009).

[2] Wang, Z. L., "Nanostructures of zinc oxide," Materials Today 7(6), 26-33 (2004).

[3] Law, M., Greene, L. E., Johnson, J. C., Saykally, R.; Yang, P., "Nanowire dye-sensitized solar cells," Nat. Mater. 4(6), 455-459 (2005).

[4] Leschkies, K. S., Divakar, R., Basu, J., Enache-Pommer, E., Boercker, J. E., Carter, C. B., Kortshagen, U. R., Norris, D. J.; Aydil, E. S., "Photosensitization of ZnO nanowires with CdSe quantum dots for photovoltaic devices," Nano Lett. 7(6), 1793-1798 (2007).

[5] Wang, G., Yang, X., Qian, F., Zhang, J. Z.; Li, Y., "Double-sided CdS and CdSe quantum dot co-sensitized ZnO nanowire arrays for photoelectrochemical hydrogen generation," Nano Lett. 10(3), 1088-1092 (2010).

[6] Ahn, K. S., Yan, Y., Shet, S., Deutsch, T., Turner, J.; Al-Jassim, M., "Enhanced photoelectrochemical responses of ZnO films through Ga and N codoping," Appl. Phys. Lett. 91, 231909 (2007).

[7] Preciado-Flores, S., Wang, D., Wheeler, D. A., Newhouse, R., Hensel, J. K., Schwartzberg, A., Wang, L., Zhu, J., Barboza-Flores, M.; Zhang, J. Z., "Highly reproducible synthesis of hollow gold nanospheres with near infrared surface plasmon absorption using PVP as stabilizing agent," J. Mater. Chem., (2010).

[8] Liu, L., Wang, G., Li, Y.; Zhang, J. Z., "CdSe quantum dot-sensitized Au/TiO 2 hybrid mesoporous films and their enhanced photoelectrochemical performance," Nano Research 4(3), 249-258 (2011).

[9] Du, L., Furube, A., Yamamoto, K., Hara, K., Katoh, R.; Tachiya, M., "Plasmon-Induced Charge Separation and Recombination Dynamics in Gold- TiO2 Nanoparticle Systems: Dependence on TiO2 Particle Size," J. Phys. Chem. C 113(16), 6454-6462 (2009).

[10] Chen, Z. H., Tang, Y. B., Liu, C. P., Leung, Y. H., Yuan, G. D., Chen, L. M., Wang, Y. Q., Bello, I., Zapien, J. A., Zhang, W. J., Lee, C. S.; Lee, S. T., "Vertically Aligned ZnO Nanorod Arrays Sentisized with Gold Nanoparticles for Schottky Barrier Photovoltaic Cells," J. Phys. Chem. C 113(30), 13433-13437 (2009).

[11] Dawson, A.; Kamat, P. V., "Semiconductor-metal nanocomposites. photoinduced fusion and photocatalysis of gold-capped TiO2 (TiO2/gold) nanoparticles," The Journal of Physical Chemistry B 105(5), 960-966 (2001).

[12] Greene, L. E., Law, M., Goldberger, J., Kim, F., Johnson, J. C., Zhang, Y., Saykally, R. J.; Yang, P., "Low Temperature Wafer Scale Production of ZnO Nanowire Arrays," Angewandte Chemie International Edition 42(26), 3031-3034 (2003).

[13] Abramoff, M. D., Magalhaes, P. J.; Ram, S. J., "Image Processing with ImageJ," Biophotonics International 11(7), 36-42 (2004).

[14] Newhouse, R. J., Wang, H., Hensel, J. K., Wheeler, D. A., Zou, S.; Zhang, J. Z., "Coherent Vibrational Oscillations of Hollow Gold Nanospheres," J. Phys. Chem. Lett. 2(3), 228-235 (2011).

[15] Meyer, B., Alves, H., Hofmann, D., Kriegseis, W., Forster, D., Bertram, F., Christen, J., Hoffmann, A., Straßburg, M.; Dworzak, M., "Bound exciton and donor–

acceptor pair recombinations in ZnO," physica status solidi (b) 241(2), 231-260 (2004).

[16] De Angelis, F.; Armelao, L., "Optical properties of ZnO nanostructures: a hybrid DFT/TDDFT investigation," Phys. Chem. Chem. Phys. 13, 467-475 (2011).

[17] Hartland, G. V., "Measurements of the material properties of metal nanoparticles by time-resolved spectroscopy," Phys. Chem. Chem. Phys. 6(23), 5263-5274 (2004).

[18] Katkar, R. A., Ramanathan, S., Bandyopadhyay, S.; Tait, G., "Wire-size-dependent optical activity in electrochemically self-assembled II-VI semiconductor nanowire arrays," Physica E: Low-dimensional Systems and Nanostructures 40(3), 556-560 (2008).

[19] Katkar, R. A.; Tait, G. B., "The effect of stationary ultraviolet excitation on the optical properties of electrochemically self-assembled semiconductor nanowires," J. Appl. Phys. 101(5), 053508-053508-7 (2007).

[20] Yamamoto, A., Kido, T., Goto, T., Chen, Y., Yao, T.; Kasuya, A., "Dynamics of photoexcited carriers in ZnO epitaxial thin films," Appl. Phys. Lett. 75, 469 (1999).

[21] Mehl, B. P., Kirschbrown, J. R., House, R. L.; Papanikolas, J. M., "The End is Different than the Middle: Spatially Dependent Dynamics in ZnO Rods Observed by Femtosecond Pump-Probe Microscopy," J. Phys. Chem. Lett. 2, 1777-1781 (2011).

[22] House, R. L., Mehl, B. P., Kirschbrown, J. R., Barnes, S. C.; Papanikolas, J. M., "Characterizing the Ultrafast Charge Carrier Trapping Dynamics in Single ZnO Rods Using Two-Photon Emission Microscopy," J. Phys. Chem. C 115, 10806-10816 (2011).

[23] Sun, C. K., Sun, S. Z., Lin, K. H., Zhang, K. Y. J., Liu, H. L., Liu, S. C.; Wu, J. J., "Ultrafast carrier dynamics in ZnO nanorods," Appl. Phys. Lett. 87, 023106 (2005).

[24] Kwok, W., Djuriši , A., Leung, Y., Chan, W.; Phillips, D., "Time-resolved photoluminescence from ZnO nanostructures," Appl. Phys. Lett. 87, 223111 (2005).

[25] Hendry, E., Koeberg, M.; Bonn, M., "Exciton and electron-hole plasma formation dynamics in ZnO," Physical Review B 76(4), 045214 (2007).

[26] Zhang, S., Wei, S. H.; Zunger, A., "Intrinsic n-type versus p-type doping asymmetry and the defect physics of ZnO," Physical Review B 63(7), 075205 (2001).

[27] Lany, S.; Zunger, A., "Anion vacancies as a source of persistent photoconductivity in II-VI and chalcopyrite semiconductors," Physical Review B 72(3), 035215 (2005).

[28] Reynolds, D., Look, D., Jogai, B., Hoelscher, J., Sherriff, R., Harris, M.; Callahan, M., "Time-resolved photoluminescence lifetime measurements of the and free excitons in ZnO," J. Appl. Phys. 88, 2152 (2000).

CHAPTER 3: Effects of Hydrogen Treatment and Air Annealing on Ultrafast Charge Carrier Dynamics in ZnO Nanowires Under *In Situ* Photoelectrochemical Conditions

3.1 Abstract

ZnO nanowires (NWs) grown by the hydrothermal method on fluorine-doped tin oxide (FTO) glass substrate were characterized by scanning electron microscopy (SEM), optical absorption, photoelectrochemical (PEC) photocurrent density, and ultrafast transient absorption pump probe spectroscopy (TAS). The as-grown NWs were annealed in air, pure hydrogen atmosphere, or annealed first with air annealing followed by hydrogen treatment. By TA spectroscopy, the samples exhibited a triple exponential transient bleach recovery with lifetimes on the fast (10-15 ps), medium (100-200 ps), and slow (>1 ns) time scale, attributed to shallow donor mixed with electron hole plasma recombination, donor bound recombination, and donor acceptor pair recombination (DAP), respectively. The as-grown samples were dominated by donor and DAP recombination. Air annealing improved the crystal structure but had little effect on hole trapping. Significantly, the hydrogen-treated NWs showed a

reduction in hole trapping and DAP recombination. Hole trapping was attributed to zinc vacancies (V_{Zn}) and hydrogen was proposed to passivate these defects. The photocurrent density of the air annealed and co-treated NWs were measured, the latter of which showed improved performance which was attributed to, in part by, decreased hole trap states and improved electrical conductivity. *In situ* ultrafast TA spectroscopy was used to study the photoanodes under working conditions as a function of applied bias. For both samples, the medium time constant become faster with increasing applied bias. A model was proposed to extract the electron-hole separation time constant.

3.2 Introduction

ZnO has been a material of focused research across a wide range of potential applications including blue lasers[1,2] and photodetectors,[3,4] in part due to its large exciton binding energy (60 meV) which allows for stable excitons at room temperature. Recent advancement in the field of nanomaterials has made it possible to synthesize ZnO nanostructures with a variety of shapes and sizes, including nanoribbons, wires/rods, tubes, and propellers.[5-9] The low material cost, high electron mobility,[10] relative natural abundance, and non-toxicity of ZnO make it an increasingly attractive for various applications. For instance, one-dimensional (1D) nanostructures, such as nanowires (NWs), are of special interest in the fabrication of photovoltaic (PV)[10-14] and photoelectrochemical (PEC) devices.[15-18] NWs offer improved charge transport over zero-dimensional (0D) nanostructures while

maintaining high surface area desired for increasing loading of dye[19] or quantum dots (QDs),[11,15,16] or for creating core shell structures.[20,21]

In ZnO, many intrinsic defects have been identified which can significantly influence charge carrier recombination and photoluminescence properties. It is therefore important to understand defect related recombination dynamics so their effects can be mediated if desired. The electronic band structure of ZnO has been extensively studied by computational and experimental methods. Intrinsic defects such as zinc and oxygen vacancies (V_{Zn}, V_O) and interstitial zinc (Zn_i) are abundant due to its low formation enthalpy.[22] These defects, which are responsible for the main intermediate states, and their relative energy in relation to conduction and valence bands (CB and VB respectively) are summarized in **Figure 1.**

Figure 1. Proposed band structure of ZnO, considering the relative energy levels estimated for its main defects, (Zn_i),[22,23] (H_i),[24] (V_{Zn}),[25,26] and (V_{Zn}^{-}, V_{Zn}^{-2}).[26,27]

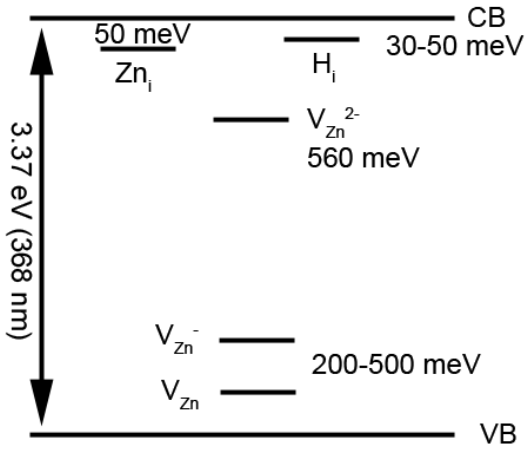

The Zn_i defect is a shallow donor defect[28] located 30 meV below the CB,[22] which has been proposed to be the primary contributing defect to the *n*-type behavior of the material. Other defects like V_O, proposed to be responsible for the yellow luminescence in the ZnO NWs[29] and persistent photoconductivity,[22] is a non-conducting localized acceptor trap state,[28] which lies 800 meV above the VB.[29] The V_{Zn} is reported to have a high formation enthalpy and lies between 200-500 meV

above the VB.[25] However, the V_{Zn} has been identified as the dominant acceptor state by positron annihilation spectroscopy (PAS) and the presence of the Zn_i has also been confirmed by this method.[30,31] Interstitial hydrogen (H_i) has been identified as an extrinsic, shallow, *n*-type dopant,[28,32,33] which lies 35 meV below the CB.[24] The presence of the interstitial hydrogen donor in the crystal lattice has been verified by FT-IR[34] and temperature dependent muon spin-rotation[35] as was predicted by Van de Walle.[32]

It is well known that ZnO is intrinsically *n*-type due to the shallow donor Zn_i and deep donor V_O, both of which have low formation enthalpy.[22] The latter defect can become doubly ionized to form V_O^{2+} after accepting two valence band holes and undergo a lattice distortion contributing to a long μs lifetime and persistent photoconductivity.[28] The V_O defect can also accept a single hole to form V_O^{+}, which has also been described as the origin of the commonly observed yellow luminescence (515-590 nm).[22,29,36] ZnO can also exhibit orange emission (600 nm) that has been proposed to involve excess interstitial oxygen, O_i;[36,37] however, assignments are unsettled.[38] In this work we will focus on the acceptor state V_{Zn} which has been shown to be the dominate hole acceptor in ZnO by positron annihilation spectroscopy (PAS).[26,30,39]

Many attempts have been made to control the densities of these defects through high temperature annealing in a variety of atmospheres including air, oxygen, hydrogen, and ammonia.[36,37,40-42] However, the effect of annealing is also disputed in the literature as photoluminescence has been shown to be an inconsistent measure of

defect concentration.[26] H_2 plasma and annealing has been used to increase the donor density[33] and conductivity[43] of ZnO films, however, the reported effects on trap states are inconsistent. Hydrogen treated TiO_2 nanostructures have very recently been reported for use in PEC water oxidation with improved performance which was attributed to increased donor density due to increased V_O.[44] While it has been proposed that hydrogen annealing can increase V_O, we will present evidence suggesting that hydrogen can also passivate the V_{Zn}.

The objective of this work was to study the effect of annealing treatments on the charge carrier dynamics and PEC properties of hydrothermally grown ZnO NWs, including *in situ* conditions. Photoexcitation of ZnO and collection of the resultant charge carriers is a dynamic, multistep process, the time scale of which spans many orders of magnitude. For *n*-type ZnO photoanodes, upon photoexcitation, hot carriers relax to the bandedge (BE) or shallow traps, the bound exciton will then be driven to separate by favorable band bending and applied bias such that the hole migrates rapidly toward the surface through the space charge layer and the electron will proceed to the back contact. While carrier cooling often occurs in the sub picosecond time regime, electron diffusivity in ZnO NWs has been reported to be between 0.05-0.5 cm^2/s,[10] and the hole reaction rate with a solution species has been found to be on the μs to ms time scale in TiO_2 [45,46], N:TiO_2 [47] and WO_3 [47]. To gain further insight into ZnO as well as other semiconducting materials, knowledge of carrier lifetimes from the second to the femtosecond time scales under working conditions can help better understand device performance. In this work we considered the variation of the

ZnO refractive index under irradiation to investigate the initial phases of electron hole separation on the picosecond time scale by recording the TA dynamics *in situ* for the photoanodes under working conditions.

In addition, we have measured the photocurrent density of the annealed and hydrogen treated films which can be used in PEC water splitting and PV applications. Annealing in air and separately in hydrogen was found to improve PEC performance, and electron hole separation was more efficient in air annealed samples suggesting the improved performance was due to increased NW conductivity and donor density upon annealing.

3.3 Experimental

3.3.1 Synthesis of ZnO NWs

ZnO NWs were grown on a ZnO nanoparticle seeded glass coated with F-doped SnO_2, (glass-FTO) substrate using hydrothermal method reported elsewhere.[37] Briefly, glass-FTO was coated drop-wise (2 drops) with 5 mM zinc acetate in ethanol and allowed to dry. This procedure was repeated five times. The sample was annealed at 350 °C for 30 min. The zinc acetate deposition and annealing processes were carried out twice to ensure a uniform coating of ZnO nanocrystal seeds on the glass-FTO. The glass-FTO coated with ZnO seeds was placed into a Teflon-lined stainless steel autoclave, filled with 20 mL aqueous solution containing 0.05 M zinc nitrate and 0.05 M hexamethylenetetramine. The sealed autoclave was heated in an electric oven at 90 °C for 6 hours. This procedure resulted in a glass-FTO coated with a uniform white film, which was rinsed with deionized water and air dried. Finally,

the as-grown glass-FTO|ZnO sample was annealed to improve the crystallinity and contact to the substrate of the ZnO NWs. The annealing was performed in air at 550 °C for 3 hours (aa-ZnO sample) or in hydrogen atmosphere at 400 °C for 15 min (Ha-ZnO), using a home-built tube furnace filled with ultrahigh purity hydrogen gas (Praxair).

3.3.2 Optical and morphological characterization of ZnO NW films

Absorption spectra were collected at room temperature with a Hewlett Packard 845A diode array UV-Visible spectrometer. Scanning electron microscopy (SEM) was conducted using a FEI Quanta 3D FEG Dualbeam microscope (5.00 kV,). Grazing incidence X-ray diffraction was collected of the thin films using a Rigaku SmartLab X-ray diffractometer with a Cu-Kα source (0.0100 degrees step, 1.0000 deg/sec scan speed, 0.3° incidence angle).

3.3.3 Femtosecond laser and transient absorption measurement

The TA laser system has been previously described elsewhere.[48] Briefly, 150 fs 1mJ pulses centered at 795 nm were split 9:1 to a optical parametric amplifier (OPA) and sapphire crystal, respectively. Samples were excited with 360 nm (3.44 eV) excitation at low (130 nJ/pulse) and high (560 nJ/pulse) pump power perpendicular to the film surface. The white light continuum generated from the sapphire crystal ranged from 430-800 nm which was monitored by CCD where 500 pulses were averaged for each data point. A forward and reverse scan was collected and averaged resulting in 1000 averages per data point. The delay stage allowed for

generation of a 1 ns delay with temporal resolution of 10 fs. The decay traces were verified to ensure a linear response with excitation power.

3.3.4 Fabrication of NW ZnO photoanodes, photoelectrochemical and transient absorption measurements in aqueous solution

ZnO NW arrays were fashioned into photoanodes by soldering a copper wire onto a bare portion of FTO substrate. The substrate was then sealed on all edges with epoxy resin except for a working area of c.a. 0.15 cm^2. All PEC measurements were carried out in a three-electrode electrochemical cell, with a coiled Pt wire as a counter electrode and an Ag/AgCl electrode as a reference. The electrolyte was a 0.5 M Na_2SO_4 aqueous solution with a pH of 7. Electrochemical measurements were acquired by a CHI 660D electrochemical station.

The PEC properties of the ZnO photoanodes were investigated with front side illumination, under simulated sunlight with a 150 W xenon lamp (Newport 6255) coupled with an AM 1.5 global filter (Newport 81094).

Investigation of each sample included the collection of TA spectra in "air" prior to immersing in the aqueous electrolyte; then, for *in situ* PEC dynamics, the photoanode was excited with a 360 nm pump (250 nJ/pulse) from the TA laser. Each data point represents the average of 400 spectra. The experiments were collected under potentiostatic control, at 0.0; 0.2 and 0.4 V in supporting electrolyte and with addition of MeOH (1% vol.) as hole scavenger. The results represent consistent findings over a minimum of eight separate experiments for the two different sample treatments.

3.4 Results and Discussion

3.4.1 Morphological and optical characteristics of ZnO NW films

The structure and surface morphology of the ZnO NWs grown by the hydrothermal method on glass-FTO, glass-FTO|ZnO, after air annealing at 550 ^{o}C for 3 h (aa-ZnO sample) was characterized by SEM. The NWs are vertically aligned hexagonal rods with a diameter of 80±20 nm and length of 1.8±0.3 µm, **Figure 2**. A similar morphology was observed after hydrogen annealing for 15 min at 400 °C (Ha-ZnO). Hydrogen annealing for longer than 20 minutes can alter the color of the sample from white to black; this effect, which has also been observed for TiO_2, has not yet been fully understood however some evidence in TiO_2 suggests absorption from defect states.[49]

Figure 2. SEM images of ZnO NWs grown on glass-FTO after annealing in air (aa-ZnO, a/b) or hydrogen (aHa-ZnO c/d) collected at 35° tilt (a, c) and side view (b, d).

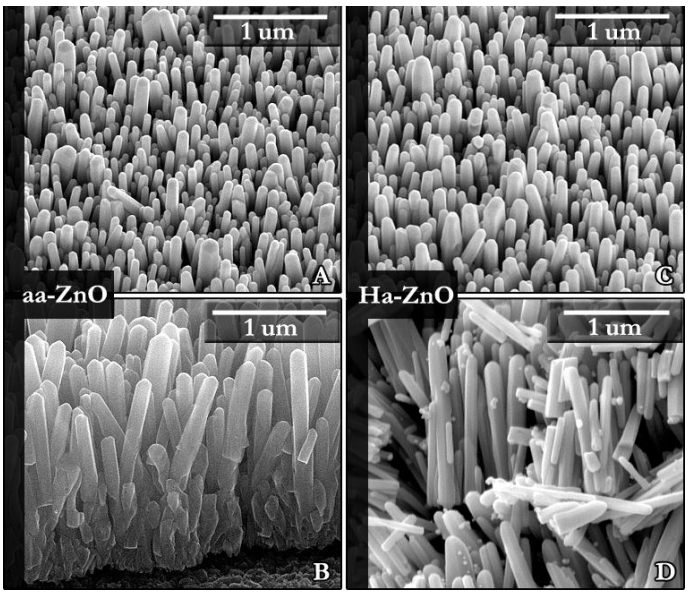

Grazing incidence X-ray diffraction of the as grown ZnO NWs (ag-ZnO), aa-ZnO, and Ha-ZnO was

Figure 3. X-ray diffraction pattern of the thin film as-grown ZnO (ag-ZnO) NWs and after air annealing (aa-ZnO) and hydrogen annealing (Ha-ZnO); as-well-as the substrate diffraction patterns from FTO and hydrogen annealed FTO (Ha-FTO).

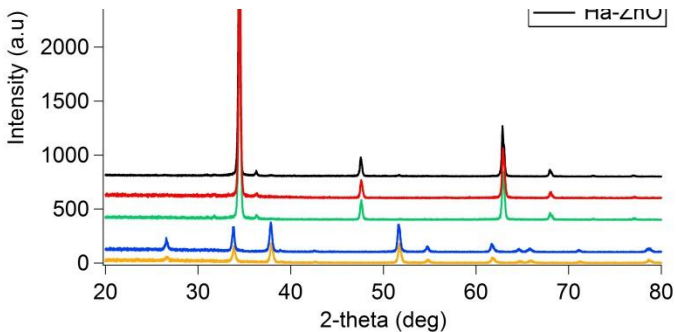

collected for the films on the FTO substrate, **Figure 3**. Bare FTO substrate diffraction patterns were collected for the FTO and hydrogen annealed FTO (Ha-FTO) as well. Substrate peaks were eliminated in the ZnO NWs diffraction pattern by setting the grazing angle to 0.3 degrees where the substrate peaks were minimized and the ZnO peaks were unaffected. The ZnO NWs did not show any significant changes between any of the samples analyzed. Likewise, the substrate peaks did not show any changes due to hydrogen annealing.

The optical absorption spectra of the ZnO NWs for both air annealed and hydrogen treated samples are reported in **Figure 4.** The spectra show strong absorptivity up to 390 nm upon which the absorptivity decreases toward the red with a 4^{th} order wavelength dependence. The absorptivity up to 375 nm is due to both absorption and scattering while the decay feature toward longer wavelengths is consistent with only scattering by the small NW dimensions.

Figure 4. UV-Vis spectra of glass-FTO|ZnO NWs annealed in air (aa-ZnO, solid line) or hydrogen (Ha-ZnO, dotted line).

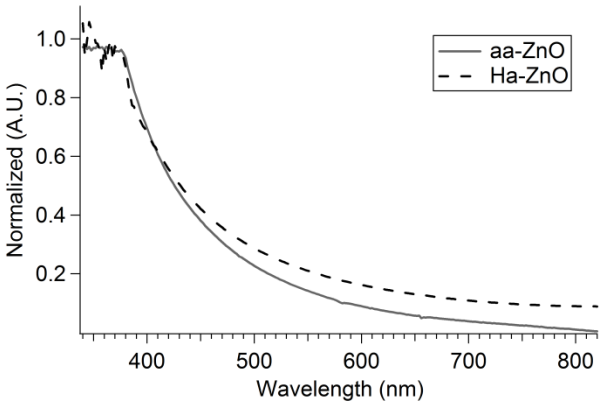

3.4.2 Transient Absorption Spectroscopy of Annealed ZnO NW Films

Using a white light continuum probe (460-800 nm), a bleach signal was recorded for the ZnO NW samples after excitation with a 360 nm pump. For a common sample, a bleach signal indicates reduced ground state absorption under

pumped perturbation. While ZnO does not absorb over our white light range, it is relevant to state that optical density is the sum of both absorption and scattering. Based on the UV-Vis spectra in **Figure 4**, the ZnO NW samples scatter strongly over the range of the white light probe. The observed bleach signal would therefore indicate less scattering under pump perturbation as the result of increased refractive index of the material while electrons were in the excited state. As the ZnO changes from insulator to conductor, the excited state electrons effectively increase the permittivity of the material thereby increasing the refractive index as has been reported previously in ZnO under UV illumination.[50,51] Thus, in an innovative approach, this feature was used to characterize the charge carrier lifetime in ZnO with TA spectroscopy. The measurements were performed using low or high pump power, for four NW ZnO samples: the as-grown (ag-ZnO); after air annealing at 550 ^{o}C for 3 h, (aa-ZnO); after hydrogen annealing at 400 ^{o}C for 15 min (Ha-ZnO) and for a sample first annealed in air and then in hydrogen (aHa-ZnO).

3.4.2.1 Transient Absorption using low pump power

The differential absorption (dA) spectra as a function of delay time for the four samples are shown in **Figure 5**, with 360 nm excitation (130 nJ/pulse). The dA spectra decreased in intensity with increasing wavelength, similar to that observed in the UV-Vis spectra. The UV-Vis absorptivity in this range was attributed to Rayleigh scattering. With increasing delay between pump and probe pulses, the dA spectra of this scattering feature recovered uniformly toward zero. The dA spectra time dependence was multiexpontential for each of the four samples tested. To more

easily compare the bleach recovery dynamics, the single wavelength time dependence was also plotted.

Figure 5. 3-dimensional (3D) plots of transient absorption profiles after excitation with a 360 nm pump (130 nJ/pulse). as a function of probe wavelength and time for glass-FTO|ZnO nanowires samples: as-grown (ag-ZnO); after air annealing (aa-ZnO); after H_2 annealing (Ha-ZnO) and after air and H_2 annealing (aHa-ZnO).

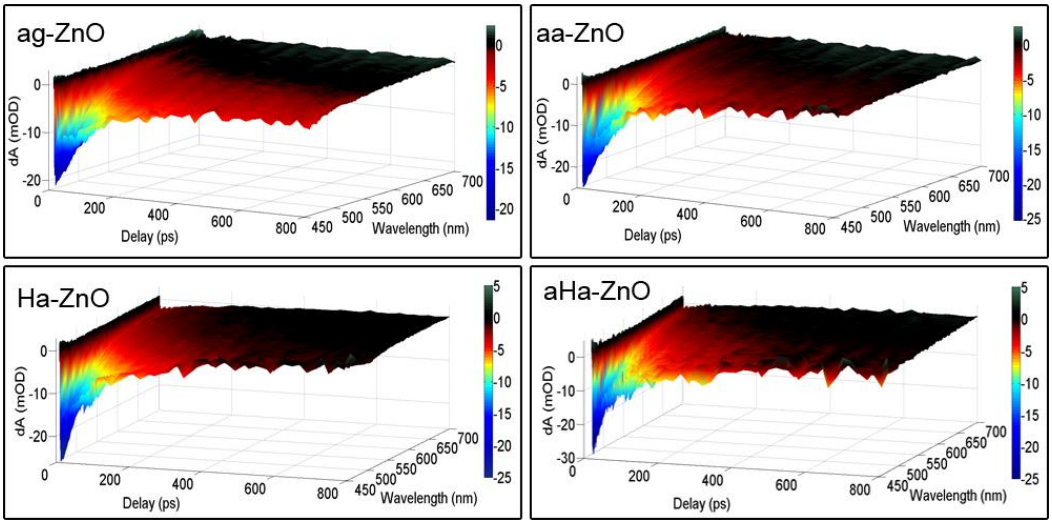

The normalized 500 nm probe bleach recovery and fitting results are shown in **Figure 6**. The ag-ZnO sample was fit with a bi-exponential recovery with time constants of 120±10 ps and >1 ns. The longest time constant could not be fully characterized by our delay stage which has a maximum time span of 1 ns. After annealing in air (aa-ZnO), the bleach recovery required a triple exponential fit with time constants15±5 ps, 130±20 ps and >1 ns. The sample annealed in hydrogen (Ha-ZnO) had similar fast and long components but a medium component of 150±20 ps. The air annealed and hydrogen treated sample (aHa-ZnO) was fit with a bi-exponential decay with lifetimes of 15±5 and 180±20 ps.

Figure 6. Transient bleach recovery time profile monitored at 500 nm for the four NW samples as excited with a 360 nm pump (130 nJ/pulse).

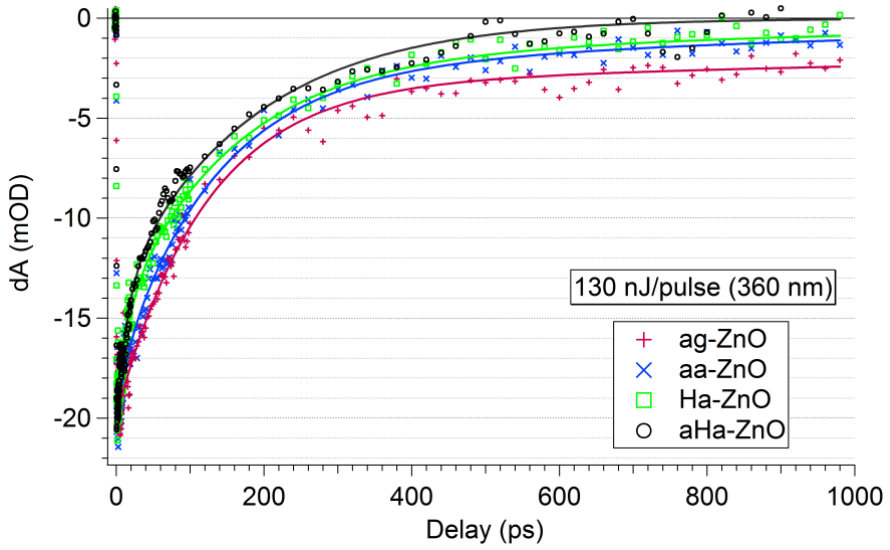

The fastest two components are consistent with other observations.[52-54] Charge carrier cooling is reported to be <200 fs[55] and typical observations of the electron-hole plasma (EHP) are within the first few ps.[2,52,56,57] Shallow trap exciton recombination has been found to be around 30 ps.[53,54] At room temperature, hole bound acceptors have been characterized to recombine with a ~200 ps lifetime while longer 1.5 ns components were attributed to donor acceptor pair recombination (DAP).[54] Green trap state emission due to V_O is reported in the μs range.[22,28,29] It is, therefore, unlikely that dynamics influenced by the V_O defect would be observed in the present data so we will focus the discussion on the V_{Zn} and exciton recombination.

While there were only slight changes in the charge carrier lifetimes of the ZnO NWs from the various treatments, a more substantial effect was observed on the amplitude of each decay component. For the as-grown NWs, the medium and slow components made up 83 and 17% of the initial amplitude. After air annealing, the fastest component increased to 10% of the initial amplitude with the remaining two components decreasing to 75 and 15%, respectively. The as-grown sample annealed in hydrogen atmosphere was composed of 23, 68, and 9% fast, medium, and slow components. The air annealed followed by hydrogen annealing sample had no contribution from the longest component with the decay being split 33:67 between fast and medium components. The fitting results for the lifetimes and relative amplitudes for the low pump power were reported in **Table 1**.

Table 1. Fitting results of the transient recovery dynamics at low (130 nJ/pulse) pump power (Figure 6) with percent intensity, lifetime (ps), and (errors) of the four diferent ZnO NW samples.

Sample	%fast	τ(fast)	%medium	τ(medium)	%slow	τ(slow)
ag-ZnO	0	0	83	120 (10)	17	1000
aa-ZnO	10	15 (5)	75	130 (10)	15	1000
Ha-ZnO	23	15 (5)	68	150 (20)	9	1000
aHa-ZnO	33	15 (5)	67	180 (20)	0	1000

Air annealing has been reported to have little effect on the [V_{Zn}] while improving overall crystal quality and increasing donor bound emission.[26] As XPS studies typically find ZnO to be oxygen deficient after any annealing treatment,[26] we attribute the donor bound recombination to Zn_i. After annealing in air, the results

indicate more shallow donor bound exciton recombination along with decreased acceptor bound recombination and essentially the same contribution from DAP recombination. Interestingly, after only a 15 minute 400 ˚C treatment in hydrogen atmosphere of the NWs, the donor bound recombination component increased to twice that of the air annealed sample, which is attributed to the increased donor density from shallow H_i states. The longest component was reduced to 9%, which represents a 2 fold reduction compared to the as grown wires. We propose that the molecular hydrogen can bind to V_{Zn} site by dissociating into atomic hydrogen and protonate two of the dangling oxygen atoms in the vacancy, thereby passivating the vacancy. This is also reflected in the medium acceptor bound recombination component having decreased as well. The air annealed sample followed by annealing in hydrogen was observed to have no contribution from longest component which is consistent with the combined effect of improved cyrstallinity with air annealing as well as V_{Zn} healing with hydrogen treatment.

3.4.2.2 TA Measurements with High Pump Power

The same samples were investigated with high pump power (560 nJ/pulse) using 360 nm light. The dA intensity response was verified to be within a linear power regime. The bleach recovery profile of the normalized 500 nm probe wavelength is reported in **Figure 7** for the four sample treatments. The as-grown sample exhibits an additional component, as compared to the low power experiment, requiring a three exponential fit of the recovery with lifetimes of 15±5 ps, 110±10 ps, and >1 ns. The air-annealed treatment had similar fast, medium, and slow

components of 13±3 ps, 105±10 ps, and >1 ns. The as-grown sample with hydrogen treatment was fit with lifetimes of 15±5 ps, 140±10 ps, and >1 ns with the remaining air annealed and hydrogen treated sample being fit with a bi-exponential recovery with lifetimes of 13±3 ps and 87±7 ps.

Figure 7. Transient bleach recovery time profile dependence monitored at 500 nm for annealed ZnO NWs pumped with 360 nm at 560 nJ/pulse.

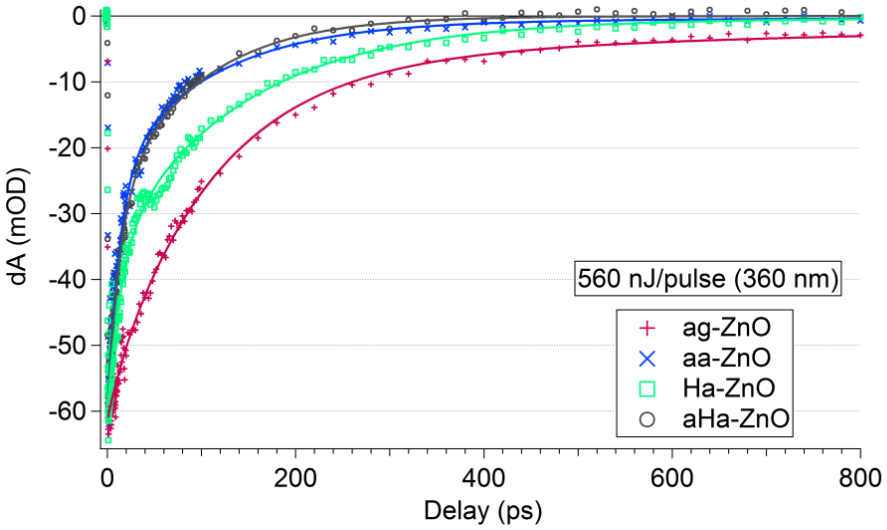

The percent contribution to the initial intensity along with the lifetime fits for the high pump power was reported in **Table 2**. The as-grown sample maintained a large relative contribution from the medium component of 84 % with the fast and slow components contributing 5 and 11% respectively. Air annealing the NWs shifted the fast/medium/slow contribution to 59/40/1. The hydrogen annealed samples maintained a larger medium component of 58% with the remaining 40% due to the fast component and a small 1% contribution from the long component. Annealing in air followed by hydrogen resulted in a 50:50 split between fast and

medium components with the complete absence of the slow component from the bleach recovery.

The reduced amplitude of the slowest component under high pump power in the as-grown sample as compared to the low power results is consistent with hole acceptor trap state saturation of the DAP recombination channel by deep hole traps. The slight increase in contribution from the fast component is attributed to increased EHP recombination under the higher pump power while the overall dynamics were dominated by acceptor bound recombination. After air annealing, the large increase in the amplitude of the fast component is consistent with improved crystal structure and enhanced effects from EHP recombination. DAP recombination was completely saturated as there was very little contribution from the long component. Interestingly, the hydrogen treated sample had more contribution from the medium component as compared to the air annealed sample implying that improved crystallinity is critical for EHP effects. Performing both air annealing and hydrogen treatment resulted in a 50/50 split between fast and medium components with the complete absence of any long component. In addition, the faster medium component could be due to decreased V_{Zn} density making the medium component take on more donor bound recombination characteristics.

Table 2. Fitting results of the ZnO transient recovery at high (560 nJ/pulse) pump power (Figure 7) with percent intensity, lifetime (ps), and (errors) of the four sample treatments.

Sample	%fast	τ(fast)	%medium	τ(medium)	%slow	τ(slow)
ag-ZnO	5	15 (5)	84	110 (10)	11	1000
aa-ZnO	59	13 (3)	40	105 (10)	1	1000
Ha-ZnO	40	15 (5)	58	140 (10)	1	1000
aHa-ZnO	50	13 (3)	50	90 (5)	0	1000

3.4.3 Photoelectrochemical and Transient Absorption Spectroscopy of ZnO NW Photoanodes in Aqueous Solution

The electrochemical properties of the air annealed and combined air/hydrogen annealed ZnO samples was investigated in 0.5M Na_2SO_4 as supporting electrolyte, using a three electrode electrochemical cell containing a platinum counter electrode and Ag/AgCl reference electrode. **Figure 8** shows the current density under applied potential, obtained in the dark and under AM 1.5G simulated solar illumination (100 mW/cm^2). The hydrogen treated sample (aHa-ZnO)

Figure 8. Linear sweep voltammograms collected for air (aa-ZnO, blue) and H_2 (aHa-ZnO ,red) annealed photoanodes ,with Ag/AgCl reference and Pt counter electrode in aqueous 0.5 M Na_2SO_4 electrolyte (pH 7) in the dark and under simulated solar illumination.

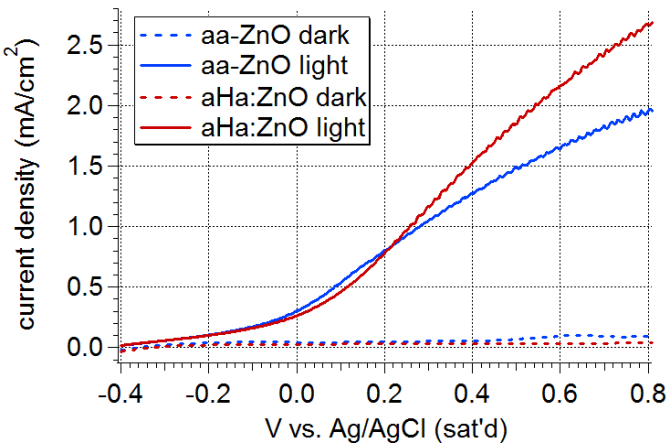

shows increased photocurrent density at biases higher than 0.22 V vs. Ag/AgCl, compared to the air annealed (aa-ZnO) sample. The observed enhancement is consistent with previous studies which also recorded improved photocurrent density using hydrogen treated TiO_2.[44]

We attribute the improved photoactivity, in part, to passivated V_{Zn} trap states upon treatment with H_2 and an increased donor density from H_i shallow donors or also V_O. Mott-Schottky plots were collected for the aa-ZnO and aHa-ZnO at 10,000 Hz in which the donor density was found to be $1.17x10^{21}$ and $2.74x10^{21}$ cm^{-3}, respectively. As previously mentioned, the V_{Zn} is a deep acceptor state which acts to trap photogenerated holes. Further discussion of this defect and its effects on PEC dynamics will be presented below.

This electrochemical cell configuration was also used to study *in situ* the dynamics of photoexcited charge carriers in the air or H_2 annealed photoanodes, aa-ZnO and aHa-ZnO, using a laser pump power of 250 nJ/pulse (3 mW/cm^2). These experiments were performed under potentiostatic control, with applied potential corresponding to 0.0; 0.2 and 0.4 V vs Ag/AgCl, in supporting electrolyte (Na_2SO_4 aqueous solution) as well as in the presence of MeOH (1% by volume), which can act as hole scavenger. **Figure 9** shows the photocurrent registered during the TAS measurements (Fig. 9a, 9b and 9c), collected simultaneously.

Figure 9. Photocurrent (μA) of two ZnO photoanodes: annealead in air (aa-ZnO) or in H_2 atmosphere after annealing first in air (aHa-ZnO) under potentiostatic control (biased at 0.0, 0.2 or 0.4 V) in an electrochemical cell with Ag/AgCl and Pt electrodes, in aqueous 0.5 M Na_2SO_4 as supporting electrolyte (pH 7) or in the presence of MeOH (1% by volume) as hole scavenger. The variation of photocurrent was recorded with excitation by 360 nm at 250 nJ/pulse (3 mW/cm^2). Photocurrent recorded as a function of the transient absorption experiment data collection time. Dark current was recorded by blocking the pump laser as indicated.

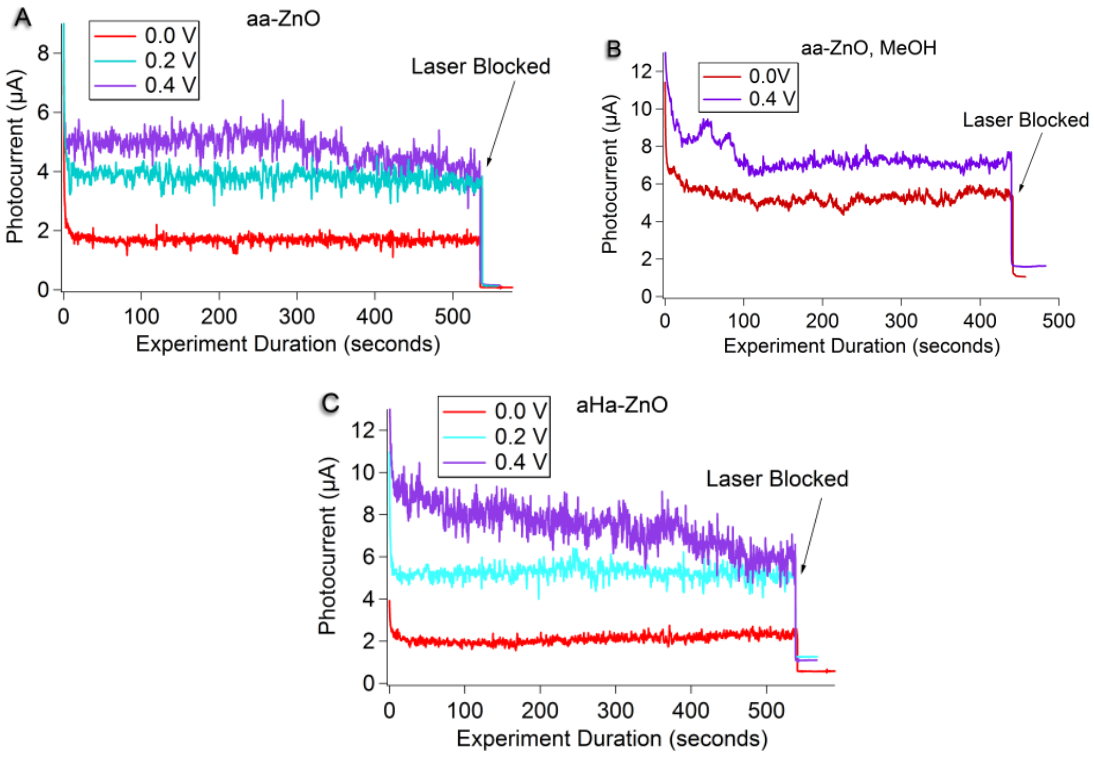

Considering first the PEC properties in supporting electrolyte (Figs. 9a, c) the aa-ZnO and aHa-ZnO photoanodes yielded similar photocurrents of 2.1 and 1.7 μA, respectively, under 0.0 V vs. Ag/AgCl. However, considerable differences were observed with increasing bias; polarization at 0.2 and 0.4 V resulted in 5.3 and 7.4 μA for the aHa-ZnO, and, for aa-ZnO, the values corresponded respectively to 3.7 and

4.9 μA; this result is consistent with the PEC results previously described. The dark current, measured by blocking the pump and probe lasers, was lower than 1 μA for polarization in these potential bias (as shown by the instantaneous drop in photocurrent as indicated). In the presence of MeOH, which acts as a hole scavenger, the aa-ZnO photoanode exhibited higher photocurrent values, 5.1 and 7.2 μA when biased at 0.0 V and 0.4 V, respectively.

Shown in **Figure 10** is the collection of *in situ* TA data displayed as: 1) 3D dA spectra for 0.0 and 0.4V vs. Ag/AgCl (top and middle row, respectively) and 2) single wavelength time dependence for 0.0, 0.2, 0.4V applied bias (vs. Ag/AgCl). The two samples studied *in situ* were the air annealed (aa-ZnO), **Figure 10 (A, D, G)**, and combined air annealed with H_2 treatment (aHa:ZnO), **Figure 10 (C, F, I)**, both on FTO glass.

The 3D dA spectra shows a wavelength dependent amplitude which is consistent with the previously described results. The TA spectra have the largest intensity toward 450 nm which decrease rapidly toward 600 nm. In general, the spectra decays faster with increased applied bias with the fastest decay observed in the 0.4V ZnO NW sample submerged with MeOH hole scavenger in the electrolyte. This is reflected in the single wavelength plots, as well, where it is clear the bias dependence has its most prominent effect on the medium length component.

Figure 10. *In situ* TA dynamics of photoexcited charge carriers in ZnO photoanodes (annealed in air or H_2 atmosphere) under potentiostatic control (biased at 0.0, 0.2, and 0.4V) in an electrochemical cell with Ag/AgCl and Pt electrodes, in aqueous 0.5 M Na_2SO_4 as supporting electrolyte (pH 7) or in the presence of MeOH (1% by volume) as hole scavenger. Top two rows: 3D TA spectra of the 0.0 V bias (top row) and 0.4 V bias (middle row). Bottom row: transient bleach recovery of the probe pulse (dotted lines) monitored at 475 nm for *in situ* photoanodes with different applied bias as well as *ex situ* ("air") samples, dry, and in air. Triple exponential fits of the transient bleach recoveries are shown as solid traces.

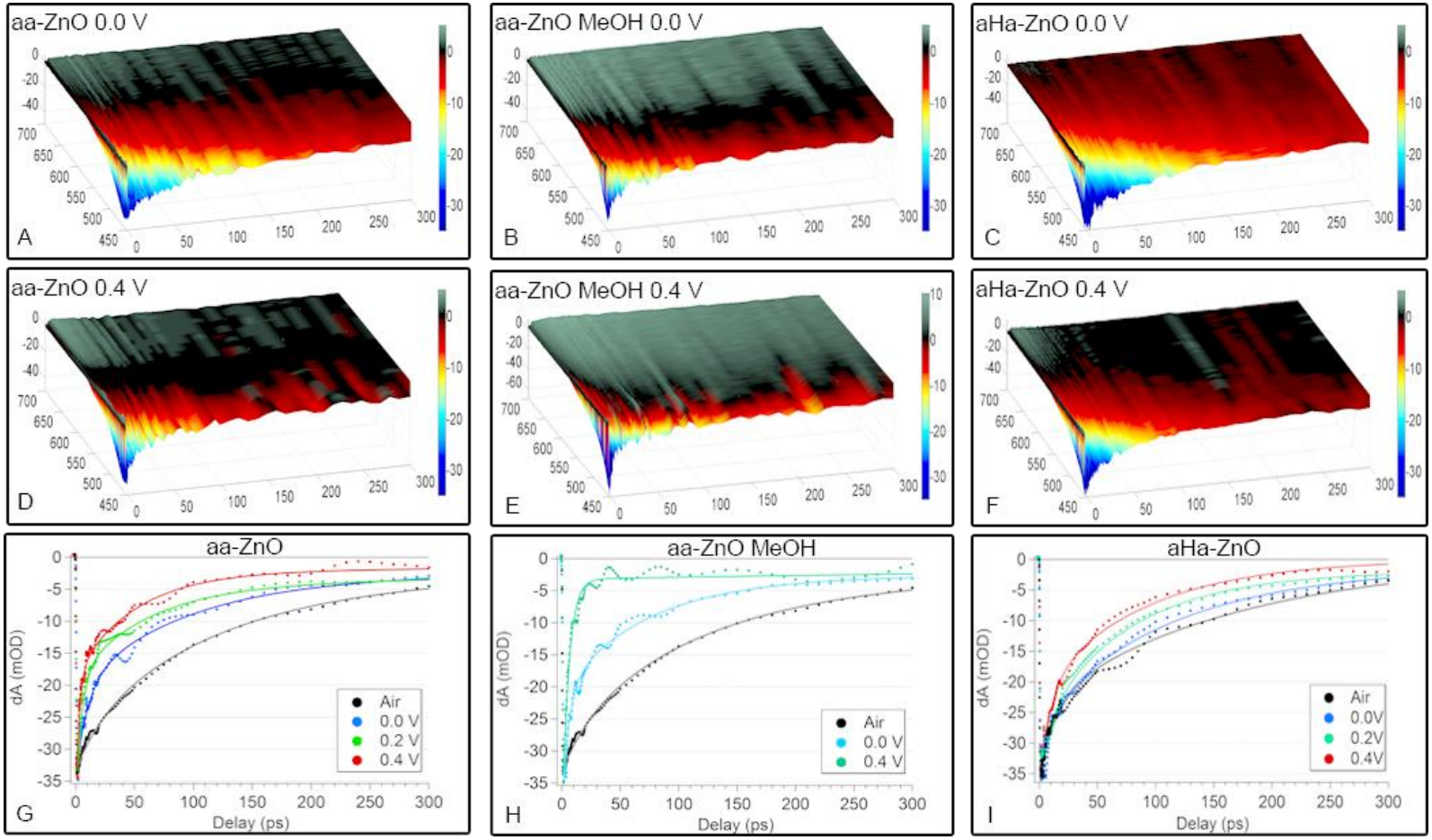
aa-ZnO 0.0 V
A
aa-ZnO MeOH 0.0 V
B
aHa-ZnO 0.0 V
C
aa-ZnO 0.4 V
D
aa-ZnO MeOH 0.4 V
E
aHa-ZnO 0.4 V
F
aa-ZnO
dA (mOD)
Delay (ps)
Air
0.0 V
0.2 V
0.4 V
G
aa-ZnO MeOH
dA (mOD)
Delay (ps)
Air
0.0 V
0.4 V
H
aHa-ZnO
dA (mOD)
Delay (ps)
Air
0.0V
0.2V
0.4V
I

The *in situ* single wavelength time dependence (at 475 nm) for measurements taken at 0.0, 0.2, 0.4V (vs. Ag/AgCl) were presented in **Figs. 10G, 10I** (aa-ZnO and aHa-ZnO in supporting electrolyte) and Fig. 10h for aa-ZnO in the electrolyte containing MeOH. For comparison, the TA data obtained *ex situ,* for each sample of dry glass-FTO|ZnO samples in air ("air") was also included.

The transient recovery data, represented by dotted lines, were fit to a triple exponential (Fig. 10 G, H, I solid lines). For the aa-ZnO film, the bleach recovery profiles show a bias dependence primarily of the medium component that became faster with increasing bias. The dry sample ("air") was fit with a triple exponential with time constants of 20 ps, 115 ps, and >1 ns. Under 0.0, 0.2, and 0.4V bias, the fast and medium components quickened from 10 and 90 ps to 5 and 60 ps, to 3 and 50 ps, respectively. In addition, the fast component increased in percent amplitude from 16% in air to 40, 50, and 53% with increasing bias. The medium and slow components in air were 71 and 13%, respectively; however, they did not show any amplitude trend with increasing bias but rather fluctuated around 43 and 7%, respectively. The fit results for this and the remaining samples have been reported in **Table 3**.

For the aHa-ZnO NW film, similar lifetime effects were observed to those in ZnO. The dry sample (measured *ex situ,* "air") could be fit with a double exponential with time constants of 15 ps and 170 ps. In the working cell under 0.0 V applied bias, both fast and medium time constants quickened to 10 ps and 110 ps and gained a third long component fit to 1 ns. With 0.2 V bias, the fast component remained the same

however the medium component decreased to 90 ps while maintaining the long component. Lastly, with 0.4 V bias, the medium time constant decreased to 75 ps. Similar to the aa-ZnO photoanode *in situ*, the % intensity from all the components remained essentially constant with increasing bias.

One model to explain the observed lifetime changes for the sample in solution and under bias is to consider an additional pathway being added to the medium component with respect to the dry sample in air. It is understood that for a semiconductor electrode in solution after photon absorption, the electron hole pair will relax to form a bound exciton and, in the closed circuit, a space charge layer is naturally established which will act as a driving force to facilitate electron-hole separation prior to recombination. For measurements taken in supporting electrolyte, we attribute the solution hole acceptor to oxygen as the solution was not purged and was at neutral pH. This pathway is otherwise not as favorable in the dry sample ("air"). As the bias is increased, there is ever more driving force to separate the electron-hole pair and we would expect a faster lifetime with increasing bias. An alternative explanation could be due to hole de-trapping from non-conductive deep traps. As both proposals involve a reaction with the hole, we expect the greatest effects to be observed in the medium length component. As we described previously, we have attributed the medium component to a bound hole recombination, likely at a V_{Zn} or other from the many reported in ZnO.[23] If we take the additional pathway to describe the hole reaction time, the additional component lifetime can be calculated using **Equation 1**, where $\tau_{obs}(V)$ is the bias dependent observed lifetime of the

medium component, τ_{air} is the medium component lifetime of the dry sample in "air," and $\tau_{e/h}(V)$ is the bias dependent lifetime of the proposed electron hole separation process.

$$\frac{1}{\tau_{obs}(V)} = \frac{1}{\tau_{air}} + \frac{1}{\tau_{e/h}(V)} \quad (1)$$

For aa-ZnO photoanode in the working electrochemical cell under 0.0, 0.2, and 0.4V bias, the hole reaction lifetime was calculated to be 400, 120, and 90 ps, respectively. For the aHa-ZnO electrode we calculate it to be 300 ps at 0.0 V, 190 ps at 0.2 V, and 130 ps at 0.4 V. At this time it is difficult to speculate about the differences between the aHa-ZnO and aa- ZnO *in situ* dynamics. However, it appears that the improved NW conductivity post H_2 annealing[43] may contribute more to the improved PEC performance than the proposed V_{Zn} hole trap passivation effects suggested previously.

To confirm that the faster lifetime of the medium component under external bias was infact due to the hole, *in situ* dynamics were collected for the ZnO NWs with the addition of 1% MeOH to the 0.5 M Na_2SO_4 to act as a hole scavenger. Under 0.0 V bias the bleach recovery was fit with three exponentials with time constants of 6 ps, 70 ps, and 1 ns. With 0.4 V bias the middle component was completely absent and the recovery was fit with two exponentials with time constants of 6 ps and 1 ns. The percent intensity of the middle component compared to the previous results were again similar with the long component remaining constant. Therefore, aleviation of the hole bottle neck causes a faster time constant with MeOH addition.

Table 3. Parameters estimated by fitting TAS data for electrodes of ZnO annealed in air (aa-ZnO) or in H_2 (aHa-ZnO) acquired at low (250 nJ/pulse) pump power *ex situ* for dry samples (air) or *in situ* in a working electrochemical cell containing aqueous Na_2SO_4 as supporting electrolyte and in the presence of the hole scavenger MeOH, under different applied potential.

	%fast	τ(fast)	%medium	τ(medium)	%slow	τ(slow)
			aHa-ZnO in supporting electrolyte			
Air	34	15 (5)	66	170 (20)	0	1000
0.0 V	30	10 (5)	65	110 (10)	5	1000
0.2 V	39	10 (5)	55	90 (5)	5	1000
0.4 V	37	10 (5)	60	75 (5)	3	1000
			aa-ZnO in supporting electrolyte			
Air	16	20 (5)	71	115 (10)	13	1000
0.0 V	40	10 (2)	49	90 (5)	11	1000
0.2 V	50	5 (2)	38	60 (5)	12	1000
0.4 V	53	3 (1)	41	50 (5)	6	1000
			aa-ZnO in electrolyte containing MeOH			
0.0 V	47	6 (2)	44	70 (5)	9	1000
0.4 V	93	6 (2)	0	na	7	1000

3.5 Conclusions

We have investigated ZnO NWs after several annealing treatments by TA pump-probe spectroscopy including as-grown wires, air annealed, pure hydrogen atmosphere, and samples first annealed in air followed by hydrogen treatment. The as-grown samples were defect rich attributed to intrinsic defect states were including V_O and V_{Zn} acceptor states. After air annealing, the TA results suggested improved crystal structure and reduced defects. Hydrogen treatment also reduced defect related recombination as proposed by passivating V_{Zn} trap states. The combination of air annealing and hydrogen treatments created films with no detectable DAP recombination on the ps time scale. The improved photocurrent density of the aHa-

ZnO compared to air annealed aa-ZnO was attributed to decreased hole trapping and increased conductivity of the films. *In situ* TA spectroscopy confirmed the medium (100-200 ps) component was due to the hole lifetime. The bias dependence of this component suggested an electron-hole separation rate in the range of 90-400 ps, depending on bias and annealing treatments.

3.6 References

1. Song, J. K.; Willer, U.; Szarko, J. M.; Leone, S. R.; Li, S.; Zhao, Y. *J. Phys. Chem. C* **2008**, *112*, 1679-1684.

2. Shih, T.; Mazur, E.; Richters, J. P.; Gutowski, J.; Voss, T. *J. Appl. Phys.* **2011**, *109*, 043504-043505.

3. Soci, C.; Zhang, A.; Xiang, B.; Dayeh, S.; Aplin, D.; Park, J.; Bao, X.; Lo, Y.; Wang, D. *Nano Lett.* **2007**, *7*, 1003-1009.

4. Zheng, X.; Li, Q. S.; Zhao, J.; Chen, D.; Zhao, B.; Yang, Y.; Zhang, L. C. *Appl. Surf. Sci.* **2006**, *253*, 2264-2267.

5. Tian, Z. R.; Voigt, J. A.; Liu, J.; McKenzie, B.; McDermott, M. J. *J. Am. Chem. Soc.* **2002**, *124*, 12954-12955.

6. Wang, Z. L. *Mater. Today* **2004**, *7*, 26-33.

7. Wang, Z. L. *ACS Nano* **2008**, *2*, 1987-1992.

8. Joo, J.; Chow, B. Y.; Prakash, M.; Boyden, E. S.; Jacobson, J. M. *Nat. Mater.* **2011**, *10*, 596-601.

9. Tian, Z. R.; Voigt, J. A.; Liu, J.; Mckenzie, B.; Mcdermott, M. J.; Rodriguez, M. A.; Konishi, H.; Xu, H. *Nat. Mater.* **2003**, *2*, 821-826.

10. Law, M.; Greene, L. E.; Johnson, J. C.; Saykally, R.; Yang, P. *Nat. Mater.* **2005**, *4*, 455-459.

11. Leschkies, K. S.; Divakar, R.; Basu, J.; Enache-Pommer, E.; Boercker, J. E.; Carter, C. B.; Kortshagen, U. R.; Norris, D. J.; Aydil, E. S. *Nano Lett.* **2007**, *7*, 1793-1798.

12. Horiuchi, H.; Katoh, R.; Hara, K.; Yanagida, M.; Murata, S.; Arakawa, H.; Tachiya, M. *J. Phys. Chem. B* **2003**, *107*, 2570-2574.

13. Xu, J.; Yang, X.; Wang, H.; Chen, X.; Luan, C.; Xu, Z.; Lu, Z.; Roy, V. A. L.; Zhang, W.; Lee, C.-S. *Nano Lett.* **2011**, *11*, 4138-4143.

14. Yuhas, B. D.; Yang, P. *J. Am. Chem. Soc.* **2009**, *131*, 3756-3761.

15. Kim, H.; Seol, M.; Lee, J.; Yong, K. *J. Phys. Chem. C* **2011**, *115*, 25429-25436.

16. Wang, G.; Yang, X.; Qian, F.; Zhang, J. Z.; Li, Y. *Nano Lett.* **2010**, *10*, 1088-1092.

17. Yang, X.; Wolcott, A.; Wang, G.; Sobo, A.; Fitzmorris, R. C.; Qian, F.; Zhang, J. Z.; Li, Y. *Nano Lett.* **2009**, *9*, 2331-2336.

18. Cooper, J. K.; Ling, Y.; Li, Y.; Zhang, J. Z. In *SPIE Proc.*; Tachibana, Y., Ed. 2011; Vol. 8109.

19. Zheng, Y.-Z.; Tao, X.; Wang, L.-X.; Xu, H.; Hou, Q.; Zhou, W.-L.; Chen, J.-F. *Chem. Mater.* **2009**, *22*, 928-934.

20. Wang, X.; Zhu, H.; Xu, Y.; Wang, H.; Tao, Y.; Hark, S.; Xiao, X.; Li, Q. *ACS Nano* **2010**, *4*, 3302-3308.

21. Myung, Y.; Jang, D. M.; Sung, T. K.; Sohn, Y. J.; Jung, G. B.; Cho, Y. J.; Kim, H. S.; Park, J. *ACS Nano* **2010**, *4*, 3789-3800.

22. Zhang, S.; Wei, S. H.; Zunger, A. *Phys. Rev. B* **2001**, *63*, 075205-075212.

23. Gavryushin, V.; Raciukaitis, G.; Juodzbalis, D.; Kazlauskas, A.; Kubertavicius, V. *J. Cryst. Growth* **1994**, *138*, 924-933.

24. Hofmann, D. M.; Hofstaetter, A.; Leiter, F.; Zhou, H.; Henecker, F.; Meyer, B. K.; Orlinskii, S. B.; Schmidt, J.; Baranov, P. G. *Phys. Rev. Lett.* **2002**, *88*, 45504-45508.

25. Chanier, T.; Opahle, I.; Sargolzaei, M.; Hayn, R.; Lannoo, M. *Phys. Rev. Lett.* **2008**, *100*, 26405-026409.

26. Tam, K. H.; Cheung, C. K.; Leung, Y. H.; Djurišić, A. B.; Ling, C. C.; Beling, C. D.; Fung, S.; Kwok, W. M.; Chan, W. K.; Phillips, D. L.et al. *J. Phys. Chem. B* **2006**, *110*, 20865-20871.

27. Nikitenko, V. In *Zinc Oxide—A Material for Micro-and Optoelectronic Applications*; Nickel, N. H., Terukov, E., Eds.; Springer: The Netherlands, 2005, p 69-81.

28. Lany, S.; Zunger, A. *Phys. Rev. B* **2005**, *72*, 035215-035228.

29. De Angelis, F.; Armelao, L. *Phys. Chem. Chem. Phys.* **2011**, *13*, 467-475.

30. Tuomisto, F.; Ranki, V.; Saarinen, K.; Look, D. C. *Phys. Rev. Lett.* **2003**, *91*, 205502-205508.

31. De La Cruz, R.; Pareja, R.; Gonzalez, R.; Boatner, L.; Chen, Y. *Phys. Rev. B* **1992**, *45*, 6581-6586.

32. Van de Walle, C. G. *Phys. Rev. Lett.* **2000**, *85*, 1012-1015.

33. Strzhemechny, Y. M.; Mosbacker, H. L.; Look, D. C.; Reynolds, D. C.; Litton, C. W.; Garces, N. Y.; Giles, N. C.; Halliburton, L. E.; Niki, S.; Brillson, L. J. *Appl. Phys. Lett.* **2004**, *84*, 2545-2547.

34. McCluskey, M.; Jokela, S.; Zhuravlev, K.; Simpson, P.; Lynn, K. *Appl. Phys. Lett.* **2002**, *81*, 3807-3809.

35. Cox, S. F. J.; Davis, E. A.; Cottrell, S. P.; King, P. J. C.; Lord, J. S.; Gil, J. M.; Alberto, H. V.; Vilão, R. C.; Piroto Duarte, J.; Ayres de Campos, N.et al. *Phys. Rev. Lett.* **2001**, *86*, 2601-2604.

36. Liu, X.; Wu, X.; Cao, H.; Chang, R. *J. Appl. Phys.* **2004**, *95*, 3141-3147.

37. Greene, L. E.; Law, M.; Goldberger, J.; Kim, F.; Johnson, J. C.; Zhang, Y.; Saykally, R. J.; Yang, P. *Angew. Chem.* **2003**, *42*, 3031-3034.

38. Djurišić, A.; Leung, Y.; Tam, K.; Hsu, Y.; Ding, L.; Ge, W.; Zhong, Y.; Wong, K.; Chan, W. K.; Tam, H. *Nanotechnology* **2007**, *18*, 095702-095710.

39. Zhang, Y.; Du, G.; Yang, X.; Zhao, B.; Ma, Y.; Yang, T.; Ong, H. C.; Liu, D.; Yang, S. *Semicond. Sci. Technol.* **2004**, *19*, 755-758.

40. Chen, Z.; Yamamoto, S.; Maekawa, M.; Kawasuso, A.; Yuan, X.; Sekiguchi, T. *J. Appl. Phys.* **2003**, *94*, 4807-4812.

41. Dutta, S.; Chakrabarti, M.; Chattopadhyay, S.; Jana, D.; Sanyal, D.; Sarkar, A. *J. Appl. Phys.* **2005**, *98*, 053513-053518.

42. Wu, L.; Wu, Y.; Pan, X.; Kong, F. *Opt. Mater.* **2006**, *28*, 418-422.

43. Studenikin, S.; Golego, N.; Cocivera, M. *J. Appl. Phys.* **2000**, *87*, 2413-2421.

44. Wang, G.; Wang, H.; Ling, Y.; Tang, Y.; Yang, X.; Fitzmorris, R. C.; Wang, C.; Zhang, J. Z.; Li, Y. *Nano Lett.* **2011**, *11*, 3026-3033.

45. Tang, J.; Durrant, J. R.; Klug, D. R. *J. Am. Chem. Soc.* **2008**, *130*, 13885-13891.

46. Cowan, A. J.; Tang, J.; Leng, W.; Durrant, J. R.; Klug, D. R. *J. Phys. Chem. C* **2010**, *114*, 4208-4214.

47. Tang, J.; Cowan, A. J.; Durrant, J. R.; Klug, D. R. *J. Phys. Chem. C* **2011**, *115*, 3143-3150.

48. Newhouse, R. J.; Wang, H.; Hensel, J. K.; Wheeler, D. A.; Zou, S.; Zhang, J. Z. *J. Phys. Chem. Lett.* **2011**, *2*, 228-235.

49. Wheeler, D. A.; Wang, G.; Fitzmorris, B. C.; Adams, S. A.; Li, Y.; Zhang, J. Z. *MRS Proc* **2012**, *e04-07*, 1387-1396.

50. Katkar, R. A.; Ramanathan, S.; Bandyopadhyay, S.; Tait, G. *Physica E* **2008**, *40*, 556-560.

51. Katkar, R. A.; Tait, G. B. *J. Appl. Phys.* **2007**, *101*, 053508-053515.

52. Yamamoto, A.; Kido, T.; Goto, T.; Chen, Y.; Yao, T.; Kasuya, A. *Appl. Phys. Lett.* **1999**, *75*, 469-471.

53. Mehl, B. P.; Kirschbrown, J. R.; House, R. L.; Papanikolas, J. M. *J. Phys. Chem. Lett.* **2011**, *2*, 1777-1781.

54. House, R. L.; Mehl, B. P.; Kirschbrown, J. R.; Barnes, S. C.; Papanikolas, J. M. *J. Phys. Chem. C* **2011**, *115*, 10806-10816.

55. Sun, C. K.; Sun, S. Z.; Lin, K. H.; Zhang, K. Y. J.; Liu, H. L.; Liu, S. C.; Wu, J. J. *Appl. Phys. Lett.* **2005**, *87*, 023106-023109.

56. Kwok, W.; Djuriši , A.; Leung, Y.; Chan, W.; Phillips, D. *Appl. Phys. Lett.* **2005**, *87*, 223111-223114.

57. Hendry, E.; Koeberg, M.; Bonn, M. *Phys. Rev. B* **2007**, *76*, 045214-045220.

Chapter 4. Ab-Initio Calculation of Ionization Potential and Electron Affinity of Six Common Explosive Compounds

4.1 Abstract

The vertical and adiabatic ionization potential (IP_V and IP_A) and vertical electron affinity (EA_V) for six explosives: RDX (hexogen), HMX (octogen), TATP (triacetone triperoxide), HMTD (hexamethylene triperoxide diamine), TNT (2,4,6-trinitrotoluene), and PETN (pentaerythritol tetranitrate); have been studied using *ab initio* computational methods. The IP_V was calculated using MP2 and CBS-QB3 and Koopmans' theory, while the IP_A was calculated with B3LYP, CAM-B3LYP, ωB97XD, B2PLYP, and MP2 using the ΔE method for the ground state B3LYP optimized geometries. IP_As of RDX and TNT were also calculated using CBS-QB3 using relaxed geometries of the ions. Of the methods tested, B3LYP and B2PLYPD provided superior and more consistent results for calculating the IP compared to CBS-QB3 level IP_A calculations and experimental data (where available). CBS-QB3 was used as a benchmark for calculating the EA_V as experimental data has not been reported. For calculations of the EA_V, B3LYP performed the worst while MP2 and B2PLYPD predicted values closest to those made by CBS-QB3. Basis set effects were evaluated using 6-31+G(d,p), 6-311+G(d,p), and 6-311+G(3df,2p) for both IP and EA. 6-31+G(d,p) gave satisfactory results for calculating IP while 6-311+G(3df,2p) had improved results for calculating the EA. The four nitro-containing compounds have exothermic reduction potentials while the peroxides are endothermic. In addition, it was determined that RDX, HMX, TATP and HMTD had

unstable geometries in their reduced forms. The results should be useful in developing detection and screening methods including ionization methods for mass spectroscopy (MS) and fluorescence quenching methods of detection.

4.2 Introduction

Chemical screening and detection of common explosives in environments such as automobiles, airports, and mail have become the focus of intense research after events such as the 2001 attempt to destroy American Airlines Flight 63 from Paris in mid-flight using explosives hidden in his shoe. There have been many successful methods for explosives detection,[1,2] which include pulse laser ionization time of flight,[3,4] laser induced photofragmentation,[5] ion mobility spectrometry,[6,7] HPLC-diode array detection,[8,9] electrochemical microfluidic device,[10] LC/MS-atmospheric pressure chemical ionization,[11] and Raman.[12] Other methods utilizing colorimetric[13,14] detection (when a reagent is exposed to an explosive produces a color change) or fluorescence detection have been developed. Fluorescence techniques typically offer improved sensitivity. Fluorescence methods utilize a probe whose emission is quenched by the analyte. While these methods are not as selective as mass spectroscopy (MS) techniques, they offer rapid screening for use in the field.[15,16] Several approaches for choosing the fluorescent probe have been studied. For instance, conjugated fluorescent polymers have been applied to the detection of gas phase TNT[17] and to a wide range of explosives in solution.[18-21] Coupling of the fluorescent polymer to an orthogonal technique such as thin layer chromatography has proven effective in improving selectivity while maintaining low detection

limits.[22] Quantum dot (QD) fluorescent probes have successfully been applied to detecting TNT through use of amine capped ZnS:Mn^{2+},[23] L-cysteine capped CdTe[24], and CdTe/CdS core/shell hybrid Au-nanorod assemblies[25]. Detection limits as low as 5 ng mm^{-2} have been achieved on manila envelopes.[26] However, the application of QD based techniques to a variety of explosives is limited.

Several studies suggest fluorescence quenching by a charge transfer mechanism where an excited electron in the conduction band (CB) of the probe (for example a conjugated polymer or quantum dot) is transferred to a lower lying acceptor state (likely the LUMO level) in the explosive where it can thereafter transfer back to the valence band (VB) of the probe.[19,23,24] To help validate this model, a an estimate of the vertical ionization potential (IP_V) will help place the HOMO level of the explosive with respect to the CB and VB energies. In addition, the electron affinity (EA) for the explosive analytes is needed to place the LUMO level with respect to the VB to determine if the reduction reaction is favorable. Sanchez *et al* calculated B3LYP/6-31G* level Kohn Sham HOMO and LUMO orbital eigenvalues for a number of explosives to explain quenching trends observed in conjugated fluorescent polymers.[19] This knowledge may in turn aid in a better understanding of the fluorescence quenching mechanism and help expand methods to include a broader range of common and home-made explosives.

The calculated adiabatic ionization potential (IP_A) can aid in optimization of ionization methods and techniques for MS detection and quantification.[4] Some groups have focused on utilization of laser ionization rather than chemical or electron

impact to generate analyte ions prior to MS analysis.[3] The high energy needed to ionize these molecules using single photon absorption would necessitate the use of 100-150 nm laser light. In order to avoid the complications inherent in working in the deep UV, laser ionization is accomplished via non-linear absorption (for example two or three photon absorption) of a pulsed excitation laser. Optical paramagnetic amplifiers have provided tunable excitation lasers between 230 nm – 22 μm in some cases,[27,28] allowing for tunable excitation using a wavelength multiple of the ionization energy of the target analyte. As non-linear absorption is sensitive to input power density and is typically very inefficient for organic molecules,[29] knowledge of the target ionization potential can allow for careful tuning of the excitation so as to optimize analyte ionization while minimizing background.

Six explosive compounds were studied in this report, including two nitroamines: RDX (hexogen) and HMX (octogen); two peroxide explosives: TATP (triacetone triperoxide) and HMTD (hexamethylene triperoxide diamine); as well as TNT (2,4,6-trinitrotoluene) and PETN (pentaerythritol tetranitrate). The molecular structures are provided in **Figure 1**. These classes of compounds offer an additional

Figure 1. Molecular structures of the six explosive compounds: RDX, HMX, TNT, PETN, TATP, and HMTD.

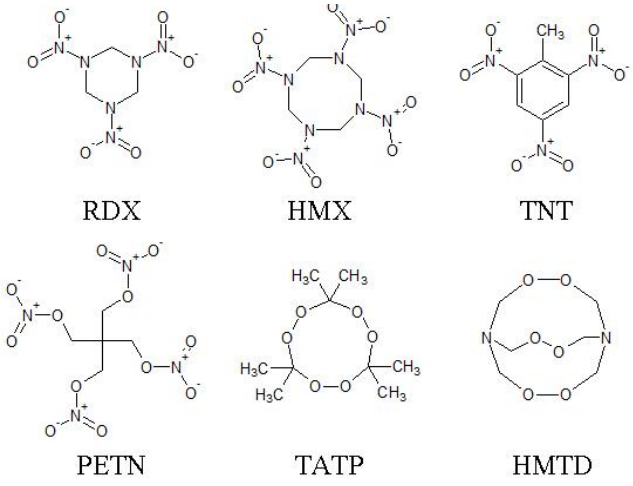

interesting test of current DFT methods as the systems are highly correlated.

The accuracy of the calculated IP and EA is expected to vary depending both on the level of theory and basis set. These values were compared between several DFT methods including: B3LYP,[30] CAM-B3LYP,[31] and ωB97XD;[32] the double hybrid method B2PLYPD,[33] and the MP2 method. While B3LYP has been successfully applied in a wide range of applications including: the prediction of heats of formation for a number of explosives,[34] the decomposition reaction pathway of RDX and HMX[35,36] as well as TATP;[37] we wanted to test the success of two long-range corrected functionals in predicting IP and EA as well. CAM-B3LYP is the long range corrected version of B3LYP which uses 0.19 Hartree Fock (HF) and 0.81 B88 exchange for short range interactions and 0.65 HF and 0.35 B88 at long range.[31] ωB97XD is a long range corrected function which uses 100% HF exchange for long-range interactions whose cutoff is controlled by the value ω which was optimized by Chai *et al*.[32] This functional has an adjustable parameter (X) to include short-range exact exchange while adding empirical dispersion correction (D).[32] B2PLYPD is a double hybrid semi-empirical method that uses an optimized 0.53 mixing between HF and Becke (B) exchange while attempts to improve the correlation energy as obtained by (LYP) by applying a second-order correlation to the Kohn-Sham orbitals, like MP2, the contribution of which was optimized to 0.27. This functional was also used with added empirical dispersion correction (D).[33,38] Other mixed WF and DFT double hybrid methods have proven successful in predicting IP and EA as compared to CBS-Q.[39,40] Finally, these results were compared to the MP2 values. The methods

were tested with three basis sets including 6-31G+(d,p), 6-311+G(d,p), and 6311+G(3df,2p).

To provide a comparison for the above results, complete basis set method CBS-QB3[41] calculations were performed on each of the six compounds, as experimental data are unavailable in most cases. The CBS-QB3 method performs five successive calculations starting with geometry optimization and frequency calculation using B3LYP followed by three single point calculations using CCSD(T), MP4SDQ, and MP2 methods. The result can produce bond energies to within 1 kcal/mol (0.043 eV) accuracy.[41] These calculations are excessively costly for these large systems; however, they provided a critical comparison method for the above described DFT and MP2 calculations. Discussion of the HOMO and LUMO molecular orbitals has not been addressed as it was not the direct focus of this work; however, detailed analysis of these and other orbitals of interest have been conducted and will be reported in detail in a separate study. The combination of DFT and wave function methods included in this study should provide a guide to future analytical efforts, it has been reported that DFT tends to overestimate the EA while HF methods underestimate it.[42]

4.3 Computational Methods

All calculations were performed using the Gaussian 09[43] program on a Sunfire X2200 M2 x64 server (2x Opteron quad core). Calculations were performed on geometry optimized structures in the gas phase. The geometries of the six common organic explosive molecules: RDX, β-HMX TATP, TNT, PETN, and HMTD were

minimized using B3LYP/6-31+G(d,p) which has been reported to produce accurate ground state geometries.[44] The minimized geometries were verified by calculating the vibrational energies to confirm there were no imaginary frequencies.

Single point energies were calculated on the geometry optimized structures for the neutral, cationic, and anionic form of each compound. The ionization potential (IP) and electron affinities (EA) were calculated from the single point energies using several methods including: B3LYP, CAM-B3LYP, ωB97XD, MP2, and B2PLYPD. Three basis sets were used for each method which included 6-31+G(d,p), 6-311+G(d,p), and 6-311+G(3df,2p). IP and EA were calculated from the absolute energies by using **Equations 1** and **2**, respectively, in which M, M^+, and M^-, were the neutral, cationic, and anionic, forms of the optimized structures.[45]

$$-IP = E(M^+) - E(M) \quad \textbf{(1)}$$

$$-EA = E(M^-) - E(M) \quad \textbf{(2)}$$

CBS-QB3 level calculations were performed for each of the compounds starting with the B3LYP/631+G(d,p) geometries described above. The IP and EA were taken from the HOMO and LUMO orbital energies, respectively. The ionized forms of TNT and RDX were calculated using CBS-QB3 by which the IP was calculated with **Equation 1**. These values are taken to be close to what would be measured experimentally for the EA and used as the reference comparisons and for calculating mean absolute deviation (MAD).

4.4 Results and Discussion

4.4.1 Total Energy

The minimized total energy (E_h) for the six explosives (RDX, HMX, PETN, HMTD, TATP, and TNT) in the three charge states (neutral, cationic, and anionic) as calculated by the six methods tested (B3LYP, CAM-B3LYP, ωB97XD, B2PLYPD, MP2, and CBS-QB3) using the 6-311+G(3df,2p) basis set is reported in **Table 1**. With the exception of the peroxides (TATP and HMTD), the remaining four explosives consistently has exothermic reduction potentials. As expected from the hybrid DFT methods (B3LYP, CAM-B3LYP, ωB97XD, B2PLYPD), the minimized energy was well below the CBS-QB3 energy for each of the explosive molecules. This result is consistent with previous works that have concluded that methods like B3LYP are not variational.[46] The double hybrid method, B2PLYPD, also reported a lower total energy than CBS-QB3; however, the magnitude of this result was less than in the single hybrid methods.

Table 1. Total energy (Hartree) of the six explosives studied by DFT methods: B3LYP, CAM-B3LYP, and ωB97XD; the double hybrid method: B2PLYPD; the wave function method: MP2; and the complete basis set method: CBS-QB3; for three charge states, neutral (0), cationic (1), and anionic (-1) using the 6-311+G(d,p) basis set.

Molecule	Charge	B3LYP	CAM-B3LYP	WB97XD	B2PLYPD	MP2	CBS-QB3
RDX	0	-897.7363731	-897.4104675	-897.4492990	-897.1493959	-895.9971866	-896.311576
	1	-897.3440172	-896.9918423	-897.0345343	-896.7580594	-895.6083858	-895.944449
	-1	-897.7801896	-897.4402900	-897.4707777	-897.1651901	-896.0219732	
HMX	0	-1196.988577	-1196.554303	-1196.611459	-1196.216815	-1194.681904	-1195.025756
	1	-1196.608644	-1196.154708	-1196.216050	-1195.837660	-1194.308424	
	-1	-1197.037038	-1196.592148	-1196.641206	-1196.250659	-1194.708759	
PETN	0	-1316.969595	-1316.505568	-1316.543794	-1316.134064	-1314.479010	-1314.511793
	1	-1316.564141	-1316.067883	-1316.103971	-1315.709997	-1314.064153	
	-1	-1317.023642	-1316.535193	-1316.562584	-1316.164315	-1314.494719	
HMTD	0	-796.6869007	-796.3779696	-796.4325716	-796.1280074	-795.0421864	-795.2729270
	1	-796.3753051	-796.0497395	-796.1090113	-795.8130225	-794.7156923	
	-1	-796.6576837	-796.3374652	-796.3810768	-796.0902273	-794.9970718	
TATP	0	-805.1801970	-804.8350192	-804.9224283	-804.5796483	-803.4364440	-803.6523030
	1	-804.8644437	-804.5007266	-804.5934464	-804.2653381	-803.1299843	
	-1	-805.1438201	-804.7890122	-804.8615303	-804.5366606	-803.3868315	
TNT	0	-885.3659690	-885.0109916	-885.0646472	-884.7736948	-883.5995416	-883.9237220
	1	-884.9786462	-884.6071939	-884.6637417	-884.3768578	-883.1744860	-883.5310470
	-1	-885.4485079	-885.0871265	-885.1360175	-884.8408476	-883.6108086	

This effect is further emphasized in **Figure 2** where the total energy (E_h) for RDX(0), RDX(+), and RDX(-) for all six methods and three basis sets tested. The trend reported in **Figure 2** was the same for all the molecules studied. It is clear from this plot that B3LYP has the largest deviation from the CBS-QB3 energy while B2PLYPD has the least with CAM-B3LYP and ωB97XD being essentially identical and between the B3PLYP and B2PLYPD energies. Also as expected, the MP2 energy was higher than the CBS-QB3 energy.

Figure 2. Plot of the total energy (E_h) in Hartree for three charge states of RDX [neutral (blue), ionized (red), and reduced (green)] as a function of method (left to right: B3LYP, CAM-B3LYP, ωB97XD, B2PLYPD, MP2, and CBS-QB3) for the three basis sets tested: 6-31+G(d,p), 6-311+G(d,p), and 6-311+G(3df,2p).

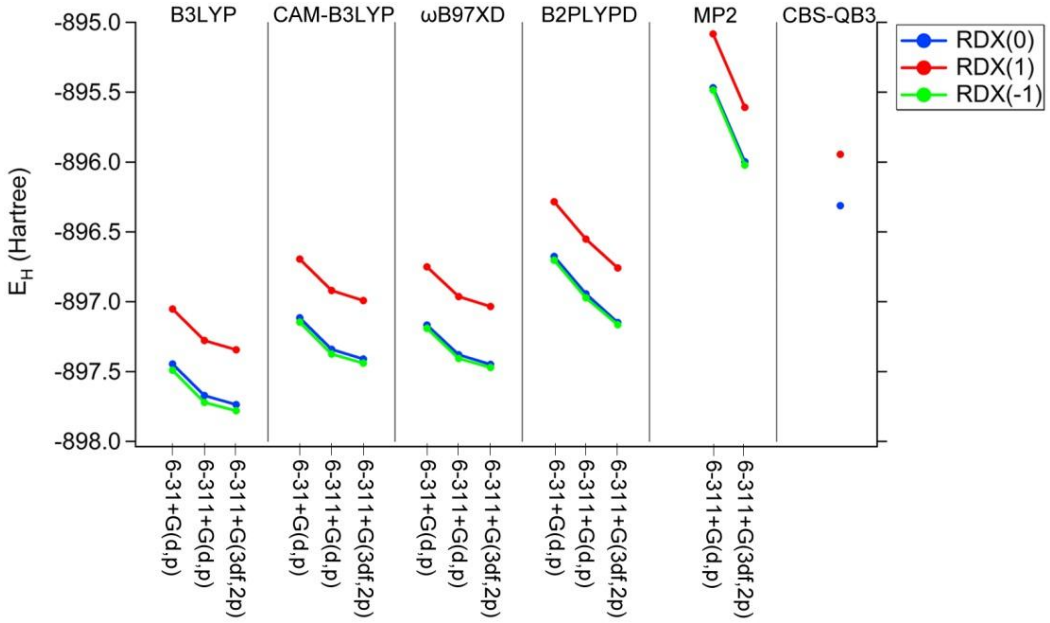

4.4.2 Ionization Potential

For wave function (WF) based methods, the orbital eigenvalues correspond to measurable quantities where the HOMO and LUMO energies are the vertical IP (IP_V) and EA (EA_V), respectively, according to Koopmans' theory. This is not necessarily the case for DFT methods, as the Kohn-Sham HOMO orbitals are well known to not accurately reproduce IP's without corrections.[45,47,48] However, comparisons of the IP_V and EA_V to the IP and EA as calculated by taking the difference between the cation and neutral molecule or anion and neutral molecule absolute energies, respectively, also known as the ΔE method, often results in large differences[49] with experimental data matching more closely the ΔE method.[44] Therefore, single point energies of the neutral, cation, and anion explosives were calculated for each of the

explosives. An additional step may be taken to match experimental data more accurately in which a geometry optimization of the cation and anion is performed to calculate the adiabatic IP (IP_A) and EA (EA_A). This method was also applied to the compound set studied for the IP.

The IP as calculated by the ΔE method (Equation 1) using B2PLYPD with three basis sets [6-31+G(d,p), 6-311+G(d,p), and 6-311+G(3df,2p)] was compared to the Koopmans' theory method of calculating the IP by taking the HOMO orbital eigenvalue (ε) as calculated by MP2 and CBS-QB3, **Figure 3**. The ΔE method more closely represents the IP_A while the Koopmans' theory method is equivalent to the IP_V. There was a clear difference in the IP values calculated by Koopmans' theory and those calculated by the ΔE method, the IPs were higher (between 0.77 and 3.04 eV) using Koopmans' theory. The MP2 6-311+G(3df,2p) level eigenvalues were very similar to those calculated by CBS-QB3 making MP2 a much more cost effective approach. As has been previously mentioned, the ΔE method generates IPs that more accurately represent experimentally determined values, which are typically equal to the IP_A rather than the IP_V. The IP_v represents a Franck Condon transition from the vibrational ground state to ionization while not changing the nuclear coordinates while the IP_A represents the energy difference between the vibrational ground states of the ion and neutral molecule. If the geometry of the ion does not change much from the neutral molecule, the IP and EA as calculated by the ΔE method without optimization of the ion geometry can be quite close to the IP_A after accounting for relaxation of the ion geometry.[49] A major focus of this work is in

predicting experimental IP; therefore, we concentrated on the ΔE approach. However the IP_V is expected to be an important factor in fluorescence quenching experiments when determining band alignment between QD or fluorescent polymers and acceptor levels in the explosives.

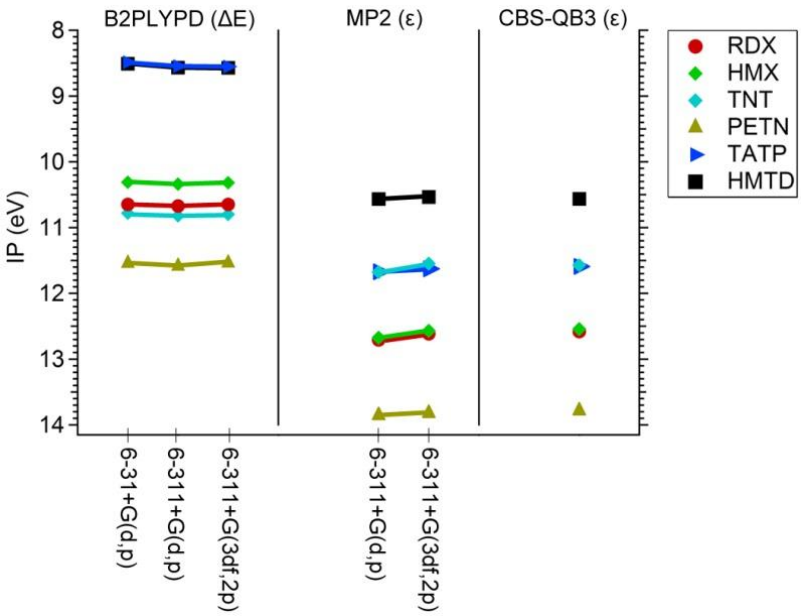

Figure 3. Ionization potential (IP) of the six explosives: RDX (red), HMX (green), TNT (cyan), PETN (gold), TATP (blue), and HMTD (black) as calculated by B2PLYPD using the ΔE method (Equation 1), and the MP2 and CBS-QB3 orbital eigenvalues (ε) using Koopmans' theory.

The IP for the six explosives was calculated using **Equation 1** for the hybrid DFT methods as well as the MP2 method without geometry optimization of the ionized form. The IP_A was calculated for two explosives (RDX and TNT) by CBS-QB3, however, the application of this method was strictly limited due to the tremendous cost of the calculations. The results are presented in **Figure 4** for the six methods and three basis sets. The CBS-QB3 IPs are expected to be the experimental IPs that are applicable in electrochemistry studies as well as optimizing ionization methods for mass spectroscopy.

In general, CAM-B3LYP and ωB97XD both predicted IPs higher than that predicted by B3LYP and B2PLYPD. It is interesting to note that the IPs had little basis set dependence compared to the deviation between methods. The average standard deviation of the IPs within a DFT method between basis sets was 0.037 eV. The average standard deviation between methods for the same basis set was 1.25, 1.23, and 1.22 eV for 6-31+G(d,p), 6-311+G(d,p), and 6-311+G(3df,2p), respectively. Therefore, the choice of method is more important than that of the basis set. The smallest basis set used was adequate over the more computational costly ones.

Figure 4. Plot of the ionization potential (IP) determined by Equation 1 (ΔE) in eV of the six explosives: RDX (red), HMX(green), TNT(cyan), PETN (gold), TATP (blue), and HMTD (black); as calculated using (from left to right): B3LYP, CAM-B3LYP, ωB97XD, B2PLYPD, MP2, and CBS-QB3 for the three basis sets 6-31+G(d,p), 6-311+G(d,p), and 6-311+G(d,p). Adiabatic IP using CBS-QB3 was reported for RDX and TNT (ΔE method).

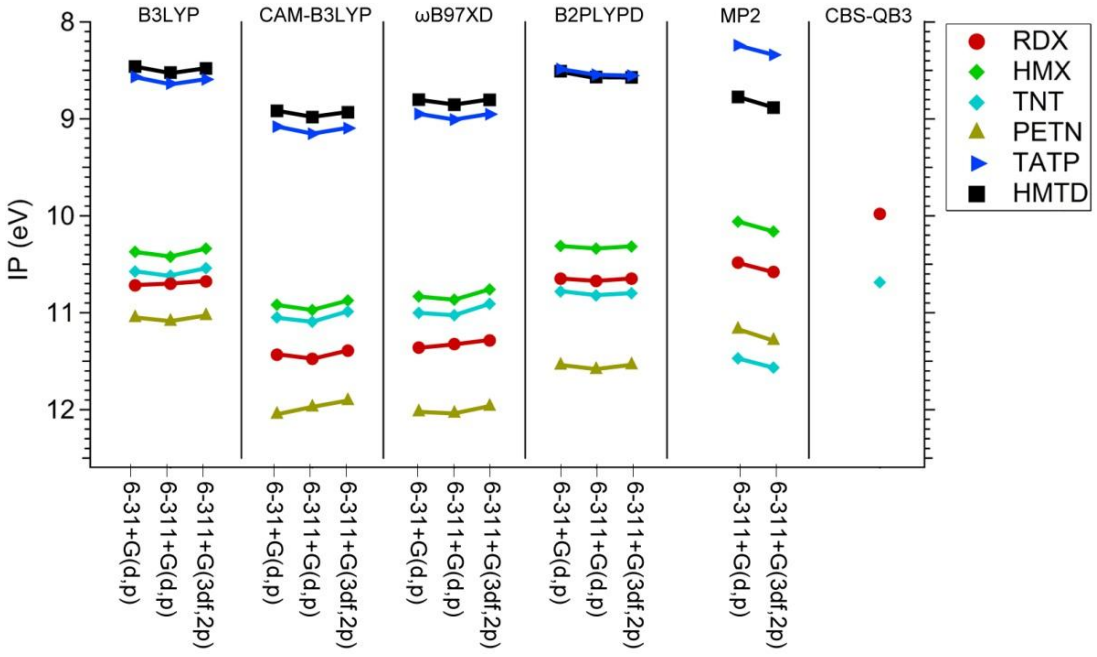

With the exception of TNT, comparisons of the results to experimental data were not possible as experimental IPs for the explosives are not available, to the best of our knowledge. GC-MS techniques have been applied to approximate the IP for TNT by other groups. Langford *et al* reported the expected IP of TNT to be between 10.4 eV and 13.4 eV,[50] Mullen *et al* reported a value below 10.49 eV,[4] while Patapov *et al* reported the IP as 10.59 eV.[51] For this reason, we calculated the IP_A for TNT by CBS-QB3 which was found to be 10.685 eV. In this context, B3LYP (10.54 eV) and B2PLYPD (10.80 eV) outperformed CAM-B3LYP (10.99 eV) and ωB97XD (10.91 eV). B2PLYPD is, however, much more costly than B3LYP. MP2 failed as the IP was calculated to be 11.57 eV using the ΔE method. Interestingly, B2PLYPD reproduced the adiabatic IP calculated using CBS-QB3 accurately.

The IP_A was calculated as well by performing a geometry optimization on the cation with B3LYP and the 6-31+G(d,p) basis set followed by a single point energy calculation using B2PLYPD with the 6-31+G(d,p) basis set. The resulting IP for all the explosives was on average 0.25 ± 0.03 eV less (with the exception of RDX that was 0.50 eV less) than the calculated IP without including the geometry optimization. If we take into account the stabilization energy from optimizing the cation geometry of TNT, the B2PLYPD predicted IP_A was found to be 10.56 eV. This result makes B2PLYPD level calculations at least consistent with CBS-QB3 at a fraction of the cost.

TATP was reported by Mullen *et al* to have an expected IP between 9.4 and 9.7 eV using pulsed laser ionization mass spectroscopy.[3] These values were obtained

by the assertions that the 9.4 eV IP energy was the six photon energy of their laser (795 nm) which they used to cause ionization of TATP and the 9.7 eV IP is that of acetone. B3LYP and B2PLYPD calculations determined the IP to be 8.59 eV and 8.55 eV, respectively, which is considerably lower than the expected result. However, it is not clear if this is due to inaccuracy of our calculations or if a 575 nm laser would also produce ionization through a four photon reaction. Further experimental evidence is required to validate our results.

The experimental IP for RDX could not be found in the literature. Our results from CBS-QB3 calculations found the IP_A to be 9.99 eV. B3LYP and B2PLYPD calculated the IP to be 10.68 and 10.65 eV, respectively. If the geometry optimized cation was used, IP_A calculated using B2PLYPD is 10.15 eV, which again is consistent with CBS-QB3. These results are consistent with the remaining explosives studied herein.

4.4.3 Electron Affinity (EA)

It was the case for RDX, HMX, HMTD, and TATP that their molecular geometries were unstable when a geometry optimization was performed on the anionic form. For instance, HMTD in the reduced form was seen to break one of the oxygen to oxygen bonds. As a result, we have focused on the EA from the perspective of an equilibrium ground state geometry rather than attempting to make the same adiabatic correction which was made to the IP calculations. The EA for the six compounds, as calculated by **Equation 2,** was reported in **Figure 5** for the hybrid DFT, double hybrid, and MP2 methods. The MP2 level calculation yielded orbital

eigenvalues for the LUMO level which were inconsistent in magnitude and sign with those calculated using the other methods tested herein; however, the ΔE method produced consistent and improved results for calculating the EA_V. The vertical EA (EA_V) was calculated using CBS-QB3 and were taken to be the negative of orbital eigenvalues of the LUMO state using Koopmans' theory. These values were taken to be the expected experimental results and have henceforth been used to compare the accuracy of the other methods tested. A positive value of the EA indicates that the reduction reaction is exothermic. RDX, HMX, TNT, and PETN had positive reduction potentials as expected while the peroxides have negative values. The values ranged between 2.5 and 0.4 eV for the former and -0.6 and -2.0 eV for the latter compounds. The EAs were very dependent on the computational method and to a lesser extent on the basis set.

Using CBS-QB3, the EAs for RDX, HMX, PETN, and TNT were found to be 0.61, 0.70, 0.40, and 0.11 eV, respectively, while the EAs TATP and HMTD were both found to be -1.12 eV. There are no experimentally determined EAs of these compounds, with the exception of TNT which has been determined to be between 0.6-0.7 eV.[52,53] The difference between the experimental EA for TNT and the one calculated herein could be a combination of experimental error (minimum of 0.2 eV)[53] as well as an expected difference between the EA_V and EA_A. The EA_A for TNT as approximated by a B3LYP geometry optimization and B2PLYPD 6-311+G(d,p) single point calculation of the anionic TNT which resulted in a correction of 0.16 eV making the EA_A for TNT approximately 0.27 eV.

It is clear from **Figure 5** that the single and double hybrid DFT methods did not perform well on TNT. The error in the TNT EA was essentially consistent between the methods; however, it is not clear as to the source of such a deviation. These methods did perform relatively well for the remaining unconjugated systems. ωB97XD had a larger deviation from the benchmark CBS-QB3 value for TATP and HMTD than the other methods tested though.

Figure 5. Electron affinities (EA) of the six explosives studied: RDX (red), HMX (green), TNT (cyan), PETN (gold), TATP (blue), and HMTD (black); as calculated by: B3LYP, CAM-B3LYP, ωB97XD, B2PLYPD, MP2, and CBS-QB3; using the basis sets: 6-31+G(d,p), 6-311+G(d,p), and 6-311+G(3df,2p).

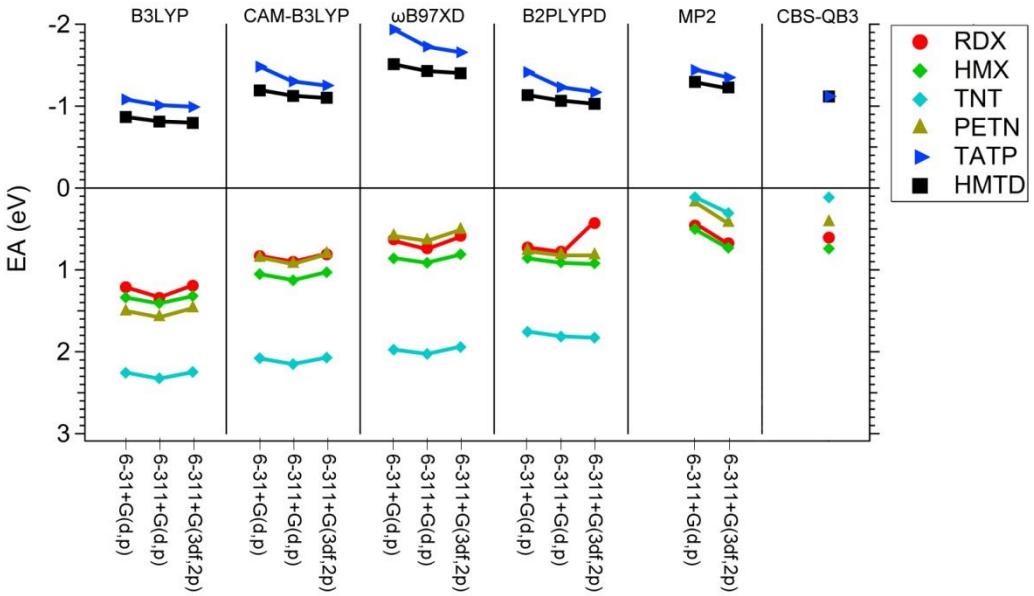

The mean average deviation (MAD) was calculated with respect to the CBS-QB3 value and has been reported in **Figure 6**. It is clear that while B3LYP performed well for predicting the IP, it performed the worst for EAs. CAM-B3LYP and ωB97XD were comparable but marked a large improvement over B3LYP while B2PLYPD outperformed the three. The EA as calculated by MP2 matched most

closely with the EA predicted by CBS-QB3 even though the former was calculated using the ΔE method and the latter was from Koopmans' theory. As B2PLYPD is similar in cost to MP2, the next cost effective method tested, by comparison, was ωB97XD/6-311+G(3df,2p).

Figure 6. Electron affinity (EA) mean average deviation (MAD) from the CBS-QB3 LUMO orbital eigenvalue as calculated by the B3LYP, CAM-B3LYP, ωB97XD, B2PLYPD, and MP2 methods using the 6-31+G(d,p), 6-311+G(d,p), and 6-311+G(d,p) basis sets.

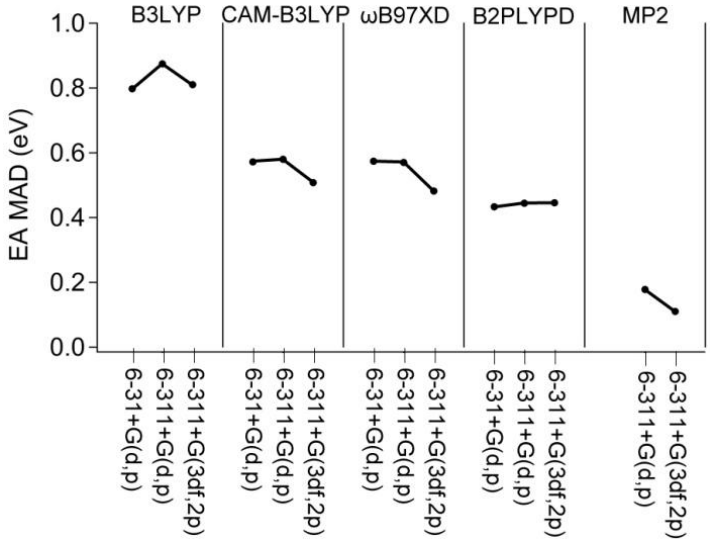

4.5 Conclusions

Three hybrid DFT methods (B3LYP, CAM-B3LYP, and ωB97XD), the double hybrid B2PLYPD, and the wave function method MP2 were tested with three basis sets (6-31+G(d,p), 6-311+G(d,p), and 6-311+G(d,p)) along with a complete basis set method, CBS-QB3, in their application to predicting the IPs and EAs for six common explosive molecules. Calculations were performed on minimized neutral ground state geometries optimized by B3LYP as well as the geometry optimized ionized forms. The IP was found using both Koopmans' theory and the ΔE method with the latter being representative of experimental evidence reported in previous works which were also consistent with the IP_A calculated by CBS-QB3 for two test molecules. The predictive quality of the various methods depended on the property

of interest (IP or EA) with B3LYP and B2PLYPD performing well for IP while MP2 and B2PLYPD performed the best for EAs. B2PLYPD consistently outperformed the other DFT methods; however, it is substantially more costly. The long-range correlated DFT functionals performed well for EAs but poorly for predicting IPs. The results should be useful in guiding further research in the field of explosives detection via fluorescence quenching and mass spectroscopy.

4.6 References

1. Moore D. Instrumentation for trace detection of high explosives. *Rev. Sci. Instrum.* 2004;752499.

2. Marshall M, Oxley JC. *Aspects of explosives detection.* The Netherlands: Elsevier; 2009.

3. Mullen C, Huestis D, Coggiola M, Oser H. Laser photoionization of triacetone triperoxide (TATP) by femtosecond and nanosecond laser pulses. *Int. J. Mass Spectrom.* 2006;252(1):69-72.

4. Mullen C, Irwin A, Pond BV et al. Detection of explosives and explosives-related compounds by single photon laser ionization time-of-flight mass spectrometry. *Anal. Chem.* 2006;78(11):3807-3814.

5. Cabalo J, Sausa R. Trace detection of explosives with low vapor emissions by laser surface photofragmentation-fragment detection spectroscopy with an improved ionization probe. *Appl. Opt.* 2005;44(6):1084-1091.

6. Oxley JC, Smith JL, Kirschenbaum LJ, Marimganti S, Vadlamannati S. Detection of explosives in hair using ion mobility spectrometry. *J. Forensic Sci.* 2008;53(3):690-693.

7. Creaser CS, Griffiths JR, Bramwell CJ et al. Ion mobility spectrometry: a review. Part 1. Structural analysis by mobility measurement. *Analyst.* 2004;129(11):984-994.

8. Borch T, Gerlach R. Use of reversed-phase high-performance liquid chromatography–diode array detection for complete separation of 2, 4, 6-trinitrotoluene metabolites and EPA Method 8330 explosives: influence of temperature and an ion-pair reagent. *J. Chromatogr., A.* 2004;1022(1):83-94.

9. Schulte-Ladbeck R, Kolla P, Karst U. Trace Analysis of Peroxide-Based Explosives. *Anal. Chem.* 2003;75(4):731-735.

10. Hilmi A, Luong JHT. Electrochemical detectors prepared by electroless deposition for microfabricated electrophoresis chips. *Anal. Chem.* 2000;72(19):4677-4682.

11. Crowson A, Beardah MS. Development of an LC/MS method for the trace analysis of hexamethylenetriperoxidediamine (HMTD). *Analyst.* 2001;126(10):1689-1693.

12. Tuschel DD, Mikhonin AV, Lemoff BE, Asher SA. Deep Ultraviolet Resonance Raman Excitation Enables Explosives Detection. *Appl. Spectrosc.* 2010;64(4):425-432.

13. Lin H, Suslick KS. A Colorimetric Sensor Array for Detection of Triacetone Triperoxide Vapor. *J. Am. Chem. Soc.* 2010;132(44):15519-15521.

14. Reynolds J, Nunes P, Whipple R, Alcaraz A. On-site analysis of explosives in various matrices. In: Schubert H, Kuznetsov A, editors. *Detection and Disposal of Improvised Explosives.* The Netherlands: Springer; 2006: 27-32.

15. Schulte-Ladbeck R, Kolla P, Karst U. A field test for the detection of peroxide-based explosives. *Analyst.* 2002;127(9):1152-1154.

16. Girotti S, Ferri E, Maiolini E et al. A quantitative chemiluminescent assay for analysis of peroxide-based explosives. *Anal. Bioanal. Chem.* 2011;400313-320.

17. McQuade DT, Pullen AE, Swager TM. Conjugated polymer-based chemical sensors. *Chem. Rev.* 2000;100(7):2537-2574.

18. Sanchez JC, Trogler WC. Efficient blue-emitting silafluorene–fluorene-conjugated copolymers: selective turn-off/turn-on detection of explosives. *J. Mater. Chem.* 2008;18(26):3143-3156.

19. Sanchez JC, DiPasquale AG, Rheingold AL, Trogler WC. Synthesis, Luminescence Properties, and Explosives Sensing with 1, 1-Tetraphenylsilole-and 1, 1-Silafluorene-vinylene Polymers. *Chem. Mater.* 2007;19(26):6459-6470.

20. Toal SJ, Magde D, Trogler WC. Luminescent oligo (tetraphenyl) silole nanoparticles as chemical sensors for aqueous TNT. *Chem. Commun.* 2005;1(43):5465-5467.

21. Sohn H, Sailor MJ, Magde D, Trogler WC. Detection of nitroaromatic explosives based on photoluminescent polymers containing metalloles. *J. Am. Chem. Soc.* 2003;125(13):3821-3830.

22. Martinez HP, Grant CD, Reynolds JG, Trogler WC. Silica anchored fluorescent organosilicon polymers for explosives separation and detection. *J. Mater. Chem.* 2012;22(7):2908-2914.

23. Tu R, Liu B, Wang Z et al. Amine-capped ZnS-Mn2+ nanocrystals for fluorescence detection of trace TNT explosive. *Anal. Chem.* 2008;80(9):3458-3465.

24. Chen Y, Chen Z, He Y et al. L-cysteine-capped CdTe QD-based sensor for simple and selective detection of trinitrotoluene. *Nanotechnology.* 2010;21125502.

25. Xia Y, Song L, Zhu C. Turn-On and Near-Infrared Fluorescent Sensing for 2, 4, 6-Trinitrotoluene Based on Hybrid (Gold Nanorod)-(Quantum Dots) Assembly. *Anal. Chem.* 2011;83(4):1401-1407.

26. Zhang K, Zhou H, Mei Q et al. Instant Visual Detection of Trinitrotoluene Particulates on Various Surfaces by Ratiometric Fluorescence of Dual-Emission Quantum Dots Hybrid. *J. Am. Chem. Soc.* 2011.

27. Newhouse RJ, Wang H, Hensel JK et al. Coherent Vibrational Oscillations of Hollow Gold Nanospheres. *J. Phys. Chem. Lett.* 2011;2(3):228-235.

28. Cooper JK, Ling Y, Longo C, Li Y, Zhang JZ. Effects of Hydrogen Treatment and Air Annealing on Ultrafast Charge Carrier Dynamics in ZnO Nanowires Under in Situ Photoelectrochemical Conditions. *J. Phys. Chem. C.* 2012;116(33):17360-17368.

29. Strehmel B, Sarker AM, Detert H. The Influence of σ and π Acceptors on Two-Photon Absorption and Solvatochromism of Dipolar and Quadrupolar Unsaturated Organic Compounds. *ChemPhysChem.* 2003;4(3):249-259.

30. Becke AD. Density-functional thermochemistry. IV. A new dynamical correlation functional and implications for exact-exchange mixing. *J. Chem. Phys.* 1996;1041040.

31. Yanai T, Tew DP, Handy NC. A new hybrid exchange–correlation functional using the Coulomb-attenuating method (CAM-B3LYP). *Chem. Phys. Lett.* 2004;393(1–3):51-57.

32. Chai JD, Head-Gordon M. Long-range corrected hybrid density functionals with damped atom–atom dispersion corrections. *Phys. Chem. Chem. Phys.* 2008;10(44):6615-6620.

33. Grimme S. Semiempirical hybrid density functional with perturbative second-order correlation. *J. Chem. Phys.* 2006;124034108.

34. Byrd EFC, Rice BM. Improved Prediction of Heats of Formation of Energetic Materials Using Quantum Mechanical Calculations. *J. Phys. Chem. A.* 2006;110(3):1005-1013.

35. Chakraborty D, Muller RP, Dasgupta S, Goddard WA. A detailed model for the decomposition of nitramines: RDX and HMX. *Journal of computer-aided materials design.* 2001;8(2):203-212.

36. Chakraborty D, Muller RP, Dasgupta S, Goddard III WA. Mechanism for unimolecular decomposition of HMX (1, 3, 5, 7-tetranitro-1, 3, 5, 7-tetrazocine), an ab initio study. *J. Phys. Chem. A.* 2001;105(8):1302-1314.

37. Dubnikova F, Kosloff R, Almog J et al. Decomposition of triacetone triperoxide is an entropic explosion. *J. Am. Chem. Soc.* 2005;127(4):1146-1159.

38. Schwabe T, Grimme S. Double-hybrid density functionals with long-range dispersion corrections: higher accuracy and extended applicability. *Phys. Chem. Chem. Phys.* 2007;9(26):3397-3406.

39. Zhao Y, Lynch BJ, Truhlar DG. Multi-coefficient extrapolated density functional theory for thermochemistry and thermochemical kinetics. *Phys. Chem. Chem. Phys.* 2005;7(1):43-52.

40. Zhao Y, Lynch BJ, Truhlar DG. Doubly hybrid meta DFT: New multi-coefficient correlation and density functional methods for thermochemistry and thermochemical kinetics. *J. Phys. Chem. A.* 2004;108(21):4786-4791.

41. Montgomery Jr J, Frisch M, Ochterski J, Petersson G. A complete basis set model chemistry. VI. Use of density functional geometries and frequencies. *J. Chem. Phys.* 1999;1102822.

42. WrÓBlewski T, Hubisz K, Antonowicz J. Theoretical study of electron affinities for selected diatomic molecules. *Optica Applicata.* 2010;40(3):601-608.

43. Frisch MJ, Trucks GW, Schlegel HB et al. Gaussian 09. 2009.

44. Lewars EG. *Computational Chemistry: Introduction to the Theory and Applications of Molecular and Quantum Mechanics.* 2nd ed. New York: Springer; 2011.

45. Zhan C-G, Nichols JA, Dixon DA. Ionization Potential, Electron Affinity, Electronegativity, Hardness, and Electron Excitation Energy: Molecular Properties

from Density Functional Theory Orbital Energies. *J. Phys. Chem. A.* 2003;107(20):4184-4195.

46. Amovilli C, March NH, Bogár F, Gál T. Use of ab initio methods to classify four existing energy density functionals according to their possible variational validity. *Phys. Lett. A.* 2009;373(35):3158-3160.

47. Zhang G, Musgrave CB. Comparison of DFT Methods for Molecular Orbital Eigenvalue Calculations. *J. Phys. Chem. A.* 2007;111(8):1554-1561.

48. Stowasser R, Hoffmann R. What do the Kohn-Sham orbitals and eigenvalues mean? *J. Am. Chem. Soc.* 1999;121(14):3414-3420.

49. Ghosh D, Golan A, Takahashi LK, Krylov AI, Ahmed M. A VUV Photoionization and Ab Initio Determination of the Ionization Energy of a Gas Phase Sugar (Deoxyribose). *J. Phys. Chem. Lett.* 2011.

50. Langford ML, Todd JFJ. Negative-ion fragmentation pathways in 2,4,6-trinitrotoluene. *Org. Mass Spectrom.* 1993;28(7):773-779.

51. Potapov VK, Kardash IE, Sorokin VV, Sokolov SA, Evlasheva TI. ionization energy of TNT. *High Energy Chem.* 1972;6347-349.

52. Foster R. *Organic Charge-Transfer Complexes.* New York: Academic Press; 1969.

53. Briegleb G. Electron Affinity of Organic Molecules. *Angew. Chem., Int. Ed. Engl.* 1964;3(9):617-632.

Chapter 5: Experimental and TD-DFT Study of Optical Absorption of Six Explosive Molecules: RDX, HMX, PETN, TNT, TATP, and HMTD

5.1 Abstract

Time dependent density function theory (TD-DFT) has been utilized to calculate the excitation energies and oscillator strengths of six common explosives: RDX (1,3,5-trinitroperhydro-1,3,5-triazine), β-HMX (octahydro-1,3,5,7-tetranitro-1,3,5,7-tetrazocine), TATP (triacetone triperoxide), HMTD (hexamethylene triperoxide diamine), TNT (2,4,6-trinitrotoluene), and PETN (pentaerythritol tetranitrate). The results were compared to experimental UV-Vis absorption spectra collected in acetonitrile. Four computational methods were tested including: B3LYP, CAM-B3LYP, ωB97XD, and PBE0. PBE0 outperforms the other methods tested. Basis set effects on the electronic energies and oscillator strengths were evaluated with 6-31G(d), 6-31+G(d), 6-31+G(d,p), and 6-311+G(d,p). The minimal basis set required was 6-31+G(d); however, additional calculations were performed with 6-311+G(d,p). For each molecule studied, the natural transition orbitals (NTOs) were reported for the most prominent singlet excitations. The TD-DFT results have been combined with the IP_v calculated by CBS-QB3 to construct energy level diagrams for the six compounds. The results suggest optimization approaches for fluorescence based detection methods for these explosives by guiding materials selections for optimal band alignment between fluorescent probe and explosive analyte. Also, the role of the TNT Meisenheimer complex formation and the resulting electronic

structure thereof on of the quenching mechanism of II-VI semiconductors is discussed.

5.2 Introduction

The detection and quantification of explosive molecules continues to be an active area of research with various security and military applications. Many laboratory-based approaches have been developed to detect these types of molecules including pulse laser ionization time of flight mass spectroscopy,[1-3] laser induced photofragmentation,[4] ion mobility spectrometry,[5,6] HPLC-diode array detection,[7,8] LC/MS-atmospheric pressure chemical ionization,[9] and Raman.[10,11] In addition, detection methods based on colorimetry[12,13] and fluorescence[14,15] have been developed. While laboratory-based methods offer high sensitivity and specificity, colorimetric and fluorescence methods are both lower in cost and easier for field deployment. Colorimetric methods utilize a reagent that produces a color change when reacted with the target analyte. Fluorescence-based approaches typically monitor luminescence intensity changes of a probe exposed to an explosive analyte.

While there have been several reports utilizing different fluorescent probes, quantum dots (QDs) made from CdSe,[16] CdTe,[17,18] CdTe/CdS,[19] CdSe/ZnS,[20] and ZnS:Mn[21] have received increasing attention due to their size tunable emission spectrum, high fluorescence quantum yield, and stability against photobleaching. A recent report using QD as the fluorescence probe reported the detection of TNT on manila envelope substrates achieving detection limits of 5 ng mm^{-2}.[17] The application of QD based detection methods has been limited to TNT, wherein the

binding mechanism to the QD probe has been through the formation of Meisenheimer complexes in which QD bound primary amine capping ligands bond with the electron deficient TNT molecule at the same ring site as the methyl group.[22] Conjugated fluorescent polymers have proven to be very effective in the detection of TNT in the gas phase,[23] surfaces,[24] and to a wide range of other explosives,[25-28] while thin layer chromatographic plates containing fluorescent a polymer are effective in increasing selectivity while maintaining low detection limits.[29] For both probe types described above, the mechanism of detection is through luminescence quenching. That is, the amount of quenching is directly related to the concentration of the target analyte. One possible fluorescence quenching mechanism involves the photoexcitation to an excited state of a probe molecule or QD with subsequent excitation transfer to a nearby analyte that has an electronic acceptor state energetically below the excited state of the probe. The relaxation that follows is non-radiative, and is typically back transfer to the ground state of the probe. Therefore, detailed knowledge of the energy levels of the target analyte and its vertical and adiabatic electron affinities (EA_V and EA_A, respectively) is critical to understanding this mechanism further.

For many of the above described methods, the absorption of light by the target analyte plays a critical role in the detection methodology. For most energetic molecules, the absorption of light is in the UV to deep UV region. Consequently, pulsed laser induced photoionization can utilize multiphoton ionization from a low energy excitation source.[2,30,31] Of course, non-linear absorption is very sensitive to

pump fluence,[32] making knowledge of the ionization energy critical to the optimization of target ionization while minimizing background interference.

As a companion to our previous study in which we reported the IP and EA for the same six explosives,[33] we have characterized the singlet transitions by TD-DFT and report the natural transition orbitals (NTOs)[34] associated with the UV to deep UV excitations for six explosives: RDX (hexogen), β-HMX (octogen), TATP (triacetone triperoxide), HMTD (hexamethylene triperoxide diamine), TNT (2,4,6-trinitrotoluene), and PETN (pentaerythritol tetranitrate). Their molecular structures are shown in **Figure 1**. The excited state orbitals may play an important role in understanding fluorescence quenching, as adequate orbital overlap of the acceptor state in the analyte is critical for efficient electron transfer and related fluorescence quenching.[35] The combination of IP, EA, and absorption energies can provide a more complete picture of these molecules fluorescence quenching mechanisms.

Figure 1. Molecular structure of the six explosives studied: RDX, HMX, TNT, PETN, TATP, and HMTD.

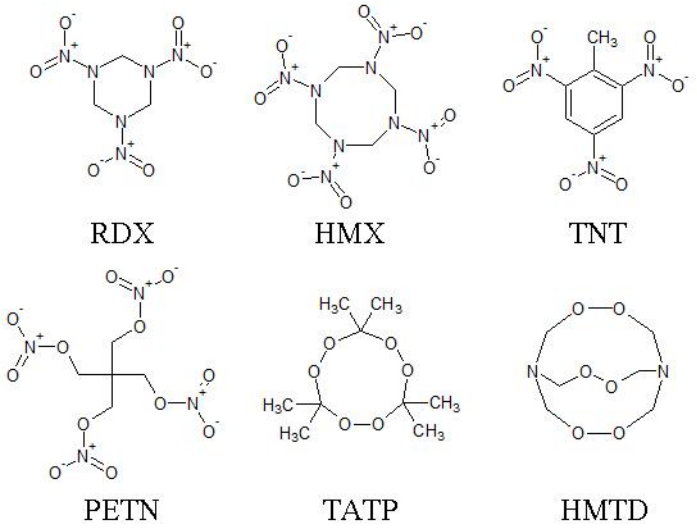

Herein, we report the experimentally determined absorptivity of the six molecules and the calculation of the component oscillators from geometry optimized

ground states with the application of B3LYP,[36] CAM-B3LYP,[37] ωB97XD,[38] and PBE0.[39] This class of compounds offers a test of current DFT methods, as the systems are highly correlated and involve charge transfer excitations. Each functional was tested against all six explosives with four basis sets to evaluate the effects on both the absorption energy and oscillator strength including: 6-31G(d), 6-31+G(d), 6-31+G(d,p), and 6-311+G(d,p). Utilization of PBE0 for TD-DFT calculations has been shown to be very effective[40] and was found to have the least mean absolute error in a study comparing 500 compounds and 29 functionals.[41] Long range corrected funcitonals like ωB97X and CAM-B3LYP have been reported to improve the prediction of charge transfer excitations.[37] We find good agreement between experimental and TD-DFT determined absorption energies.

5.3 Experimental and Computational Methods

5.3.1 Chemical Preparation and Optical Absorption

Solutions (1mg/mL) of 1,3,5-trinitro-1,3,4-triazinane (RDX), 1,3,5,7-tetranitro-1,3,5,7-tetrazocane (HMX), 2-methyl-1,3,5-trinitrobenzene (TNT), 3-nitrooxy-2,2-bis(nitrooxymethyl)propyl nitrate (PETN), 3,3,6,6,9,9-hexamethyl-1,2,4,5,7,8-hexoxonane (TATP), and 3,4,8,9,12,13-hexaoxa-1,6-diazabicyclo[4.4.4]tetradecane (HMTD) were made in acetonitrile (CHROMASOLV HPLC gradient grade). Further 1:50 dilutions were prepared for all compounds except TNT which was diluted 1:100 for UV-Vis analysis. UV-Vis absorption spectra were collected using a Hewlett Packard 8452A diode array UV-Visible spectrometer with a spectral resolution of 2 nm in a 1cm quartz cuvette.

5.3.2 TD-DFT of Singlet Excited States

All calculations were performed using the Gaussian09[42] program on a Sunfire X2200 M2 x64 server (2x Opteron quad core). Calculations were performed on geometry optimized structures in the gas phase. The geometries of the six organic explosive molecules (RDX, β-HMX, TATP, TNT, PETN, and HMTD) were minimized using B3LYP/6-31+G(d,p). The minimized geometries were verified by calculating the vibrational energies to confirm there were no imaginary frequencies. Four TD-DFT methods were compared including: B3LYP, CAM-B3LYP, ωB97XD, and PBE0. For each method, four basis sets were tested for each of the six molecules including: 6-31G(d), 6-31+G(d), 6-31+G(d,p), and 6-311+G(d,p). Vertical absorption energies and oscillator strengths were extracted and fit with a series of Gaussian peaks with a half width at half max (HWHM) of 0.333 eV, followed by summation of the Gaussian series. This value proved effective at emulating the experimental data. This standard operation was completed using GaussView5. Natural transition orbital analysis was conducted using PBE0/6-311+G(d,p).

5.4 Results and Discussion

5.4.1 Optical Absorption

The UV-Vis electronic absorption spectra of six explosives were collected in acetonitrile and shown in **Figure 2**. RDX, HMX, and TNT all exhibited a strong absorption peak near 230 nm. TNT had an additional shoulder around 260 nm and relatively low absorption that extended out to 400 nm. PETN has an absorption maximum at or below 190 nm, while TATP and HMTD had an absorption maximum

below 190 nm. Each spectrum was fit with a series sum of Gaussian peaks to identify the absorption maximum of separate absorption components. The spectral fits were reported in **Figure S1**. The RDX and HMX spectra exhibited similar absorption peaks at 236 and 230 nm with absorptivity of 10,570 and 22,460 M^{-1} cm^{-1}, respectively. The two compounds have negligible absorption at wavelengths longer than 300 nm. PETN exhibited absorption below 235 nm and an absorption max <190 nm, with an absorptivity 10,230 M^{-1} cm^{-1} at 210 nm. The TNT spectrum was more complex than that of the other molecules studied. To model this spectrum, we used a series of five Gaussian peaks with absorption maxima and absorptivity of: 198 nm (14370 M^{-1} cm^{-1}), 229 nm (14020), 254 nm (10,030), 298 nm (2710), 326 nm (2670). It is unlikely the 298 nm fit feature is significant. The measured absorptivity at 254 nm was 12,160 M^{-1} cm^{-1}. The low absorption region of the TNT

Figure 2. Experimentally determined UV-Vis absorption spectra for six explosives: RDX (black), HMX (purple), PETN (cyan), TNT (green), TATP (yellow), and HMTD (red) in the full (A) and expanded (B) perspectives.

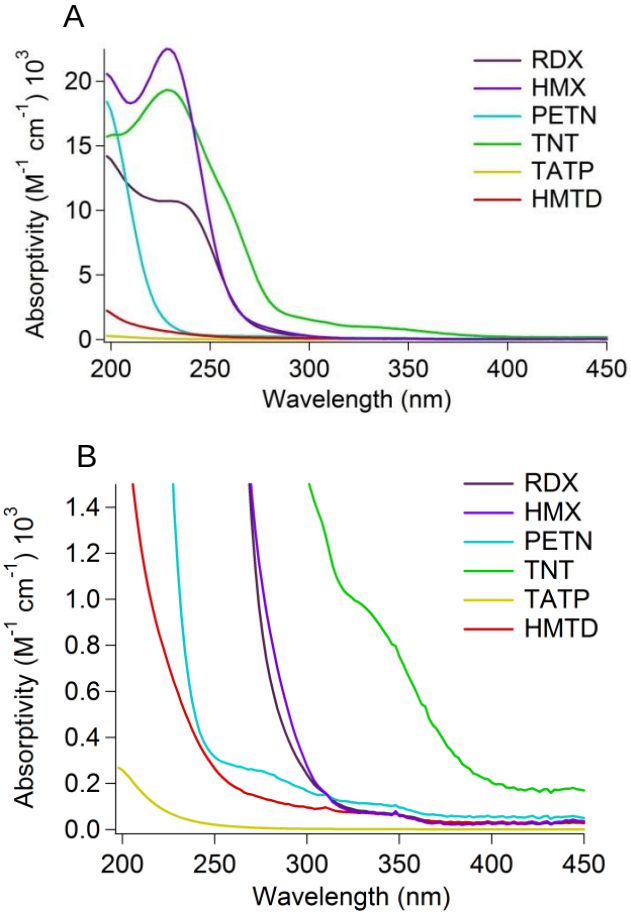

spectrum at wavelength longer than 300 nm can be more easily examined in the expanded absorption spectrum shown in **Figure 2(B).** TATP had very little recorded absorption, see **Figure 2(B)**, with an absorptivity of 260 M^{-1} cm^{-1} at 200 nm. The spectrum could be fit with two Gaussians with absorption maxima at 194 and 220 nm. HMTD exhibited a very similar absorption spectrum to TATP; however, it had approximately eight times the absorptivity at 200 nm measured to be 2,040 M^{-1} cm^{-1}. The spectrum could also be fit with two Gaussians with absorption maxima at 188 and 226 nm.

5.4.2 Predicted UV-Vis Spectra

Basis set effects were first evaluated using 6-31G(d), 6-31+G(d), 6-31+G(d,p), and 6-311+G(d,p), in which it was determined a minimal basis set 6-31+G(d) was sufficient to remove significant errors (see **Figure S2** in which PBE0 results of the absorption energies and oscillator strengths as a function of basis set were reported); however, we decided to conduct subsequent calculations with the larger 6-311+G(d,p). For each of the explosives studied, the predicted UV-Vis spectra as calculated by TD-DFT methods: B3LYP, CAM-B3LYP, ωB97XD, and PBE0 using the 6-311+G(d,p) basis set were plotted against the experimental UV-Vis spectra and reported as **Figure 3**. The resultant oscillator strength and peak position from the TD-DFT calculations were fit with Gaussian functions and summed to generate the predicted spectra.

B3LYP consistently predicted the lowest transition energies, while CAM-B3LYP and ωB97XD were consistently higher than the other methods. The latter

two methods produced essentially identical results for all the compounds studied, as can be seen in the RDX, HMX, TATP, and PETN spectra. Slight variations between CAM-B3LYP and ωB97XD in oscillator strength were seen for TNT and HMTD; however, the absorption energies were the same. All the methods failed to predict the 240 nm absorption peak position of RDX and HMX accurately. Instead, this peak appears as a shoulder in the RDX spectra at 225 nm. The oscillator strength of this feature was relatively under predicted by ωB97XD and CAM-B3LYP, but was predicted well by PBE0 and B3LYP. ωB97XD and CAM-B3LYP did not duplicate the 254 nm peak absorption energy that can be seen in the TNT spectrum, while PBE0 was in excellent agreement with the experiment.

As PBE0 was in essence an average of the methods tested and performed better in calculating the TNT spectra, we have used this method to study the molecular orbitals involved in selected transitions for the six explosives by NTO analysis. PBE0 has been previously reported to provide improved results over other DFT functionals.[41] The explosives under study are expected to have solvatochromic behavior which is the likely source of error between experimental and predicted spectra. Future studies may improve results through explicitly including the first solvation shell by MD simulations as well as including a PCM model in the TD-DFT calculations, see **Figure S3**.

Figure 3. TD-DFT predicted absorption spectra for the six explosives (RDX, HMX, TNT, PETN, TATP, and HMTD) as calculated by B3LYP (green), CAM-B3LYP (dashed-purple), ωB97XD (cyan), and PBE0 (red) using the 6-311+G(d,p) basis set. Spectra were calculated by fitting the predicted oscillators with 0.333 eV HWHM Gaussian peaks and summed to give each trace. Experimentally determined UV-Vis spectra were provided in black.

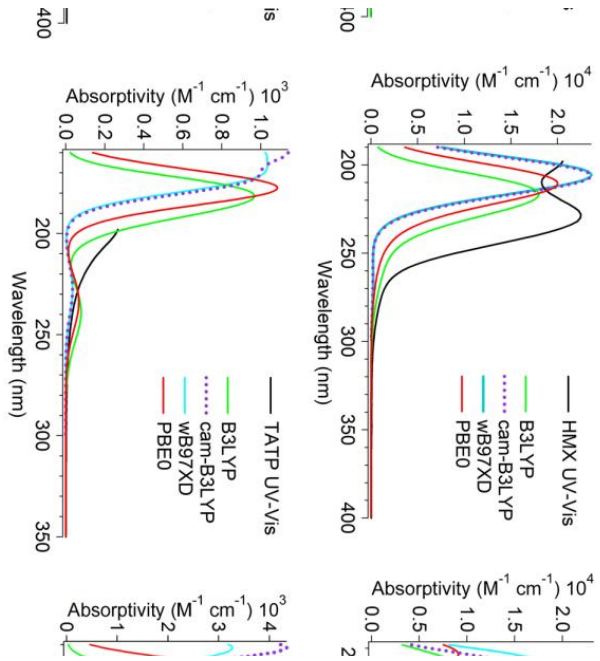

5.4.3 Molecular Orbital Analysis Using Natural Transition Orbitals

5.4.3.1 TNT

The experimentally determined absorption spectrum of TNT is presented in **Figure 4**. As previously mentioned, the spectrum was fit with a series of Gaussian functions to deconvolute the component transitions (see supporting information Figure S1 for fit). For TNT, five Gaussian line shapes were needed with λ_{max} at 198, 229, 254, and 298, and 326 nm. As previously mentioned, it is not clear from this data that the 298 nm peak is a significant feature or if it is an artifact of the data fitting procedure, as the intensity is low relative to the other Gaussian functions used. The PBE0/6-311+G(d,p) predicted absorption energies and relative oscillator strengths were displayed as vertical red lines. By using a sum of 0.333 eV HWHM Gaussian functions (which is a standard fitting protocol in the GaussView software) for each of the vertical transition energies, the predicted absorption spectrum was

generated (solid red line). The resulting spectrum agrees very well with the experimental absorption spectrum. Of the many predicted transitions, four have been selected which are both relatively large in oscillator amplitude and correlate well with the fit peaks. For these four transitions, natural transition orbitals were calculated and plotted in the lower panel of **Figure 4**.

Transition A (194 nm) has a ground state made up of primarily of O (*2p*) non-bonding (*n*) electrons located at the 2,6 positions, while the excited state is of O-N=O π^* orbitals at the 2,6 and 4 position nitro groups forming a charge transfer (CT) excitation. Transition B (230 nm) has a more complicated ground state of ring aromatic π orbitals and O (*n*) character, while the excited state is of π^* states within both the NO_2 and ring groups. Transition C (260 nm) has very similar MO structure both the ground and excited states at the transition B. The $\pi^* \leftarrow \pi$ assignment is consistent with previous reports and solvent dependent absorption energy of this peak.[43] The low oscillator strength transition D (329 nm), which causes the broadening of the absorption spectrum in that region, is of O (*n*) orbitals at the 2,6 nitro groups in the ground state and NO_2 π^* orbitals of the same 2,6 nitro groups.

Figure 4. Upper: UV-Vis absorption spectra of TNT (black line) as fit by 4 Gaussian peaks: 1 (green), 2 (blue), 3 (purple), 4 (orange), and 5 (cyan); and the sum of the fit peaks (open grey circles). Also included is the PBE0/6-311+G(d,p) predicted absorption spectra (red), including relative oscillators (vertical lines), see Figure S2 for actual values, with markers A-D pointing to transitions with the most significant oscillator strength. Lower: Natural transition orbitals of the hole and electron orbitals for the transitions corresponding to markers A-D.

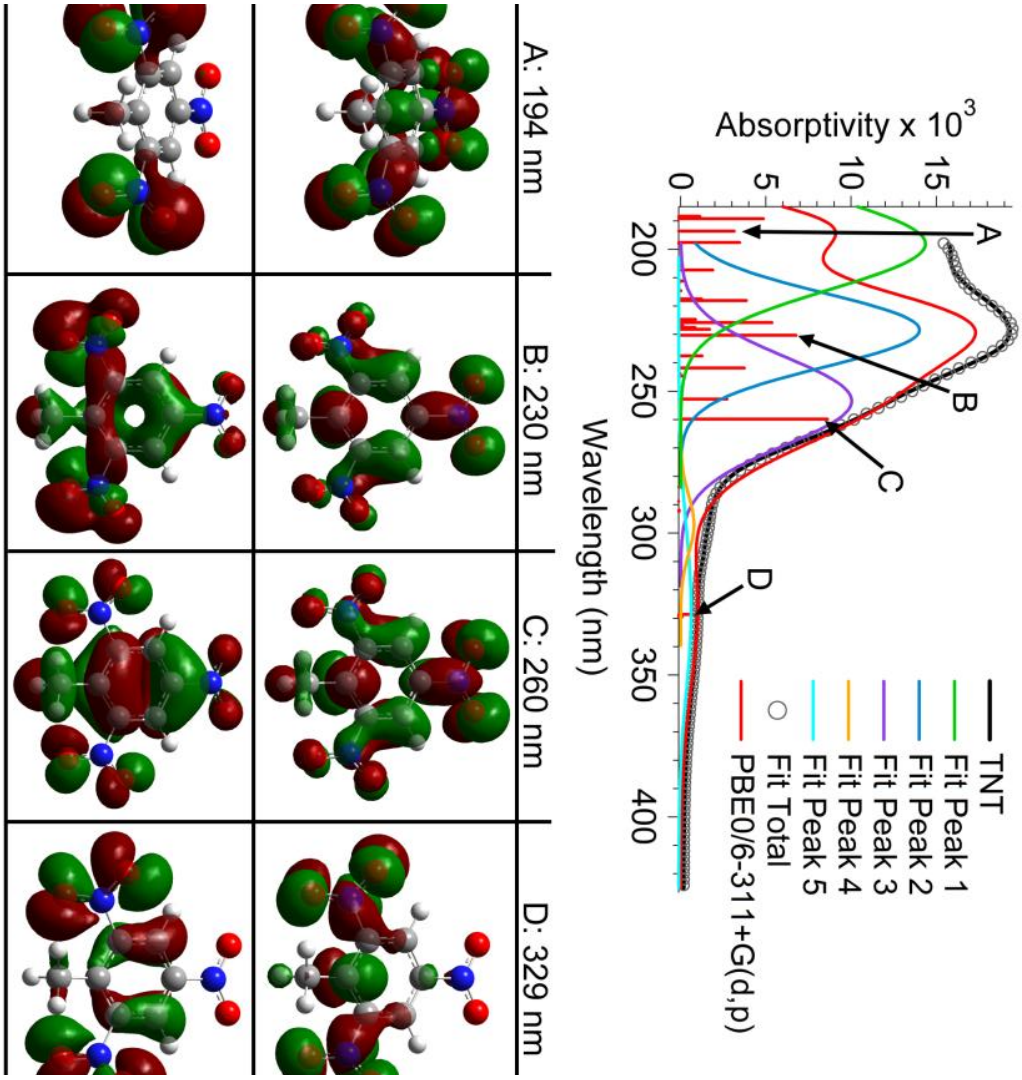

5.4.3.2 RDX

The experimentally determined UV-Vis absorption spectrum of RDX (black trace) is presented in **Figure 5**. The spectrum was fit with two Gaussian functions (green and blue traces) with λ_{max} at 196 and 237 nm. The latter transition has been described to be due to $\pi^* \leftarrow \pi$ transition[44] with the former being attributed to σ, π, σ^*, π^*, and *n* states.[10] Transition A (198 nm) has a ground state made up of a complicated mixture of states as predicted. It is mostly *n* in character, with the *n* states on the oxygens and nitrogens, which mix to form an extended pseudo-π system across the

whole molecule. The excited state is simply the N-NO_2 π^* states, the transition of which as a result, is clearly C.T. in nature. Likewise, transition B (214 nm) is an interesting π system created by the ring N atoms mixed with C-H and C-C σ bonds and some occupation due to O *n* states. Once again, the excited state is due to the N-NO_2 π^* orbitals; however, it is more equally distributed across the molecule than transition A. Finally, transition C (227 nm) is made up of mostly O *n* states mixed with the ring N *n* states; however, there is also some N-N and C-H σ bond character as well. The excited state is again the N-NO_2 π^* orbitals.

Figure 5. Left: UV-Vis absorption spectra of RDX (black line) as fit by 2 Gaussian peaks: 1 (green) and 2 (blue); and the sum of the fit peaks (open grey circles). Also included is the PBE0/6-311+G(d,p) predicted absorption spectra (red), including relative oscillators (vertical lines), see Figure S2 for actual values, with markers A-C pointing to transitions with the most significant oscillator strength. Right: Natural transition orbitals of the hole and electron orbitals for the transitions corresponding to markers A-C.

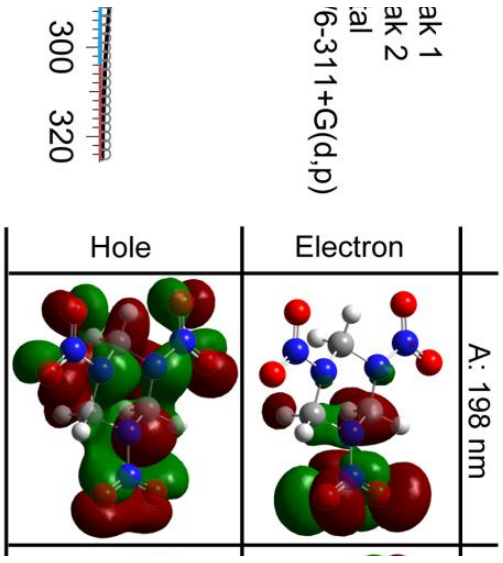

5.4.3.3 HMX

The UV-Vis spectrum for HMX is presented in **Figure 6** (black trace) along with a two Gaussian functions fit using λ_{max} at194 nm and 229 nm. The PBE0/6-311+G(d,p) predicted absorption energies and relative oscillator strengths are reported (red vertical lines) as well as the reconstructed absorption spectrum (red trace). Three absorption energies of interest were selected (A-C). The molecular orbitals relating to each transition are shown in **Figure 6** as well.

Transition A (209 nm) has a complicated ground state electronic structure consisting of O and N non-bonding with a small portion of C-H σ bonding electrons. The excited state is from N-NO_2 π^* orbitals of the nitro groups which were planar to the ring structure. Much of the electron density in the A ground state is ring centered, while the electron density of the excited state is localized on the NO_2 groups as a C.T. type excitation. The ground state of transition B (221 nm) was made up of O and ring N *n* states, while the excited state was again made up of the N-NO_2 π^* orbitals of the perpendicular nitro groups this time. Interestingly, there was a σ bond formed between the two ring N atoms made by the *p* orbitals, which with respect to the N-NO_2 group were anti-bonding but to each other formed a bonding interaction. Finally, transition C, which was low in oscillator strength in comparison to the others discussed, had a ground state made of the planar nitro group *n* states of O, while the excited state was again the planar N-NO_2 π^* states.

Figure 6. Left: UV-Vis absorption spectra of HMX (black line) as fit by 2 Gaussian peaks: 1 (green), and 2 (blue); as well as the sum of the fit peaks (open grey circles). Also included is the PBE0/6-311+G(d,p) predicted absorption spectra (red), including relative oscillators (vertical lines), see Figure S2 for actual values, with markers A-C pointing to transitions with the most significant or relevant oscillator strength. Right: Natural transition orbitals of the hole and electron orbitals for the transitions corresponding to markers A-C.

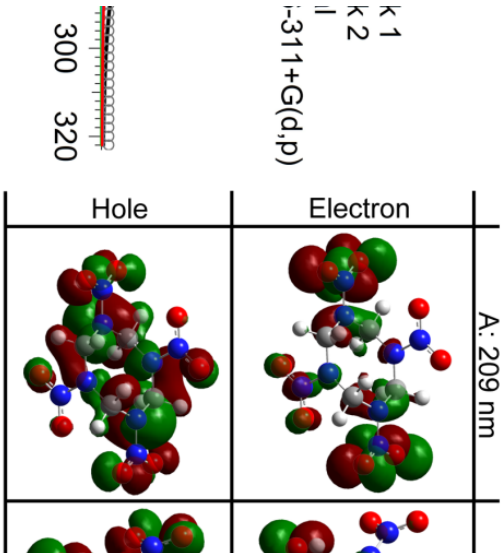

5.4.3.4 TATP

Figure 7 shows electronic absorption of TATP (black track) . The molecule had negligible absorptivity compared to the other molecules studied. The experimentally determined spectrum was not fit as the result would be meaningless. The predicted absorption energy and relative oscillator strength as calculated by PBE0/6311+G(d,p) was presented, as well as the reconstructed absorption spectrum (red). MO analysis of the transition labeled A shows a ground state of a mixed π and π* character derived from the non-bonding oxygen orbitals, while the excited state is a O-O σ^* bond. The oscillator labeled B was due to a transition between O non-bonding states and an O-O σ^* bond.

Figure 7. Left: UV-Vis absorption spectra of TATP (black line) as well as the PBE0/6-311+G(d,p) predicted absorption spectra (red), including relative oscillators (vertical lines), see Figure S2 for actual values, with marker A pointing to the transition with the most significant oscillator strength and marker B pointing to a lower energy transition. Right: Natural transition orbitals of the hole and electron orbitals for the transitions corresponding to marker A and B.

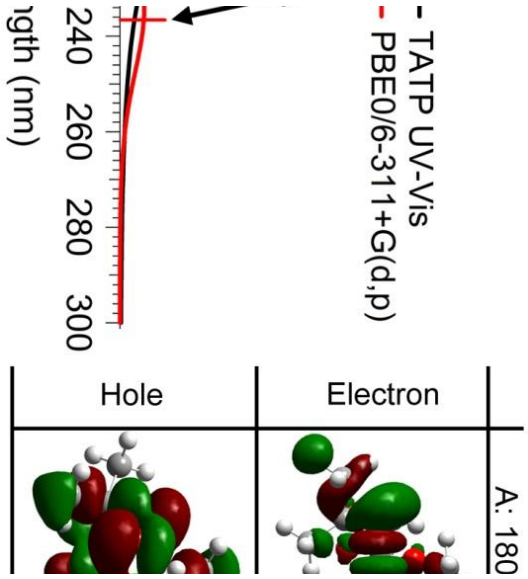

5.4.3.5 HMTD

Electronic absorption of HMTD (black trace) is shown in **Figure 8** and fit with two Gaussian functions centered at 188 and 226nm (blue and green traces). While this fit is certainly not unique, it did match nicely to the predicted spectrum and was left in for **Figure 8** as a visual aid. The PBE0/6-311+G(d,p) predicted absorption energies and relative oscillator strengths, as well as the reconstructed absorption spectrum, is presented (red) in which two transitions, A and B, have thusly been labeled. The molecular orbitals for these two labeled transitions are also presented.

The ground state of transition A (189 nm) has an interesting structure made of a relatively small contribution from C-O σ bonds, but a majority contribution from

two N atoms *n* orbitals which point into the center of the molecule. The excited state was the O-O σ^* orbital, with a small component due to a localized anti-bonding σ^* configuration between the two N atoms. Transition B shows contributions from both N and O non-bonding orbitals to the O-O σ^* states in the excited state.

Figure 8. Left: UV-Vis absorption spectra of HMTD (black line) as fit by 2 Gaussian peaks: 1 (blue) and 2 (green); and the sum of the fit peaks (open grey circles). Also included is the PBE0/6-311+G(d,p) predicted absorption spectra (red), including relative oscillators (vertical lines), see Figure S2 for actual values, with markers A

and B pointing to transitions of interest. Right: Natural transition orbitals of the hole and electron orbitals for the transitions corresponding to markers A and B.

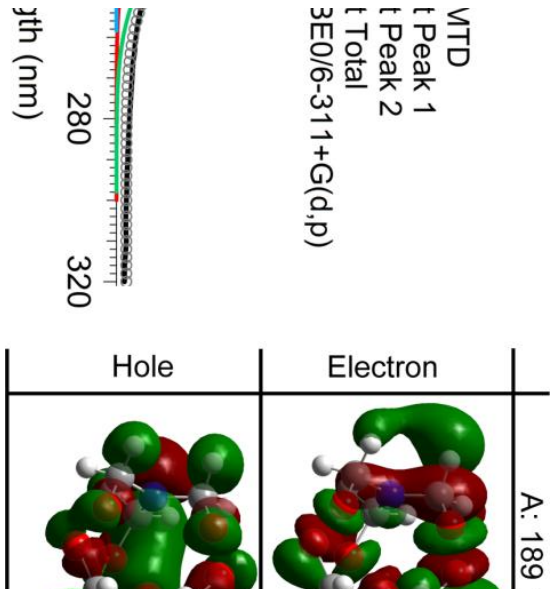

5.4.3.6 PETN

The experimental UV-Vis spectrum of PETN (black trace) is shown in **Figure 9** along with a single Gaussian fit centered at 194 nm. The absorption in this region

has been assigned to a $\pi^* \leftarrow \pi$ transition with C.T. from the carbon backbone to the NO_2 groups.[45] The PBE0 6-311+G(d,p) absorption energies and reconstructed absorption spectrum is presented in **Figure 9** as well. It should be noted that previous reports[45] have found a shoulder in the absorption spectrum at 260-290 nm due to a $\pi^* \leftarrow n$ transition of the $-NO_2$ groups; however, none of the TD-DFT methods tested calculated a non-zero oscillator in this region (though a zero oscillator was calculated for a 256 nm transition which did correspond to an $\pi^* \leftarrow n$ transition). A shoulder appearing at ~260 nm was observed in our absorption spectrum at very low relative intensity (see Figure 2 expanded view). The transition labeled A (198 nm) also corresponded to a ground state of C-H σ bonding and O non-bonding states, while the excited state was O-NO_2 π^* anti-bonding orbitals in which charge was transferred from the carbon backbone to the distal NO_2 groups.

Figure 9. Left: UV-Vis absorption spectra of PETN (black line) as fit by 1 Gaussian peak (green). Also included is the PBE0/6-311+G(d,p) predicted absorption spectra (red), including relative oscillators (vertical lines), see Figure S2 for actual values, with marker A pointing to the only transition. Right: Natural transition orbitals of the hole and electron orbitals for the transitions corresponding to A.

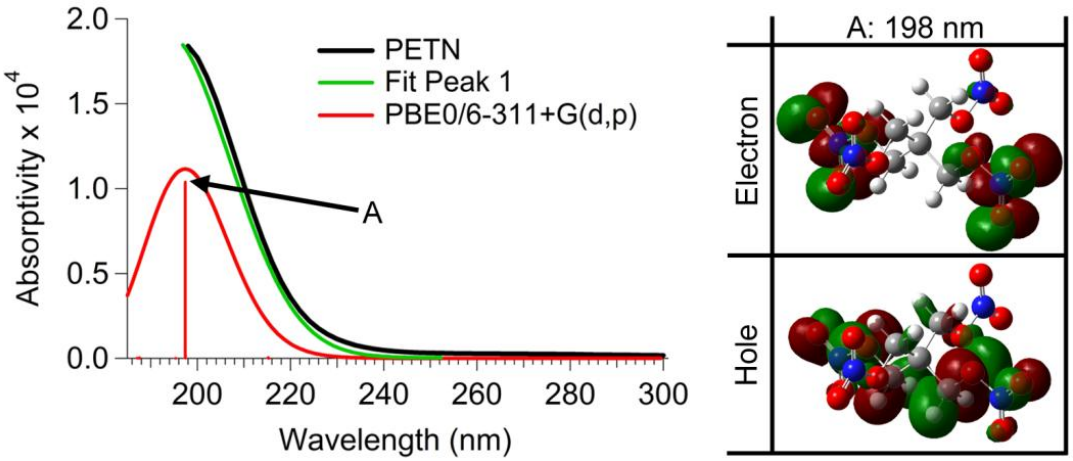

5.4.4 Energy Levels

By combining the vertical ionization potentials (IP_V) calculated by CBS-QB3 with Koopmans' theorem in our previous work[33] and the absorption energies calculated herein, we have constructed an energy level diagram for each of the six explosive molecules, as shown in **Figure 10**. For ease of comparison, the transitions described in **Figures 4-9** have been indicated in **Figure 10**. For RDX, TATP, HMTD, and PETN, the lowest 15 singlet transition energies are shown, while for HMX and TNT the first 40 are indicated. The lowest energy shown is the highest occupied molecular orbital (HOMO) and the first vertical transitions with significant oscillator strength (see **Figure S2**) for HMX, TATP, HMTD, and TNT is the lowest unoccupied molecular orbital (LUMO). For RDX and PETN, the LUMO transition is dark, having zero oscillator strength.

Figure 10. Calculated energy level diagrams for the six explosives: RDX, HMX, TATP, HMTD, TNT, and PETN. Ground state energy (HOMO) is considered equal to the vertical ionization potential (IP_V) taken from Cooper et al.[33] as calculated by

CBS-QB3. Excited states were calculated herein by TD-DFT with PBE0/6-311+G(d,p). Letters labeling transition are the same labels used in Figures 4-9 to highlight significant contributions to the absorption spectrum.

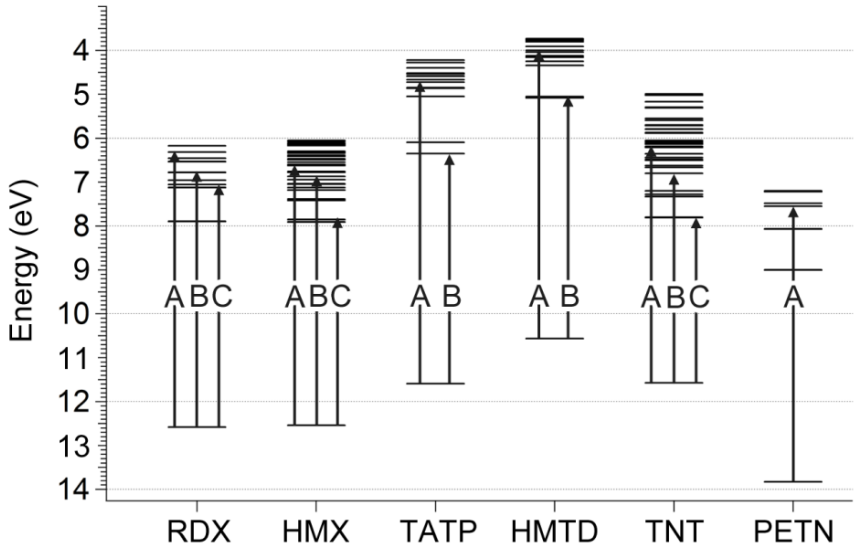

These results should be useful in the design and optimization of explosives detection methods utilizing fluorescence quenching, as the unoccupied energy levels can act as acceptor states from the fluorescent probe. For II-VI QD probes, the CB energies for CdTe, CdSe, CdS, ZnTe, ZnSe, and ZnS are all <5 eV vs. vacuum,[46,47] making them all likely candidates for fluorescence quenching by the explosive analytes, as all the explosives have a manifold of acceptor states in this range; however, possible issues in designing such systems are worth mentioning.

One potential issue could be that RDX, HMX, TNT, and PETN all have exothermic electron affinities between 0.1 and 0.75 eV, while TATP and HMTD have identical endothermic affinities of -1.12 eV. Additionally, RDX, HMX, TATP, and HMTD were seen to have unstable geometries in their reduced forms.[33] Therefore, the charge transfer step from QD → explosive could cause degradation of RDX and

HMX analyte consequently resulting in a different fluorescence quenching mechanism than has been previously discussed insofar that the energy level alignment for electron transfer and back transfer between QD and explosive may not be applicable and thus warrants further investigation.

A second issue could be band alignment with the VB of the QD, as an injected electron from the QD to an acceptor state in the explosive could decay to the LUMO level rapidly before back transfer can take place. To minimize potentially destructive reduction of the analyte by the QD and to optimize the QD quenching stability over time, the back electron transfer should be favorable. This would place a restriction on materials with VB levels below the LUMO level of the explosive analyte. PETN has a LUMO level of 9.00 eV excluding any II-VI semiconductor. RDX, HMX, and TNT (see section 3.5 about TNT-Meisenheimer complexes) have similar LUMO levels at about 8 eV, which leaves ZnO as the only candidate of II-VI semiconductors. For TATP, the LUMO was calculated to be 6.35 eV; II-VI materials with VB edges lower than the LUMO are: ZnS, ZnSe, CdS, and CdSe. HMTD has more flexibility in materials choices having a LUMO level of 5.08 eV, which includes the above listed materials plus ZnTe and CdTe. Assuming fluorescence quenching is possible with TATP and HMTD and that the CB energy is relevant to the mechanism, one could design a fluorescence assay to distinguish between an unknown sample of peroxide based explosive.

5.4.5 Meisenheimer Complex

As previously stated, QD based methods targeting TNT have utilized surface bound primary amines, which when exposed to TNT form a Meisenheimer complex, **Scheme 1**.[17,18,22] From our predictions, it does not appear that TNT is capable of quenching materials like CdSe, CdS, ZnSe, or ZnS. Therefore, the formation of this complex could be more significant to the quenching mechanism than previously thought. The rational design of using QD surface bound primary amines has been proposed as a binding mechanism of the TNT to the QD surface so efficient quenching can take place; consequently, it is likely the resulting energy levels of the TNT change dramatically to allow for electron transfer to occur.

Scheme 1. Formation of a Meisenheimer complex from the reaction of 2,4,6-trinitrotoluene with a primary amine.

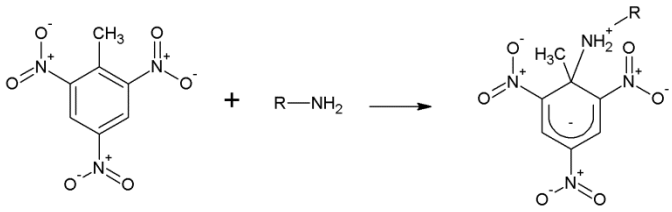

To confirm this point we have investigated the Meisenheimer complex formed between 2,4,6-trinitrotoluene and propylamine (TNT-M). Optimization of the structure was performed with B3LYP/6-31+G(d,p) and a vibrational spectrum was calculated to confirm that the minimized structure was reached. The reaction enthalpy of **Scheme 1** where R=($CH_2CH_2CH_3$) as calculated with B2PLYPD/6-311+G(3df,2p) was -20.22 KJ mol^{-1}. Assuming the contribution from entropy to be small, the equilibrium constant (K_{eq}) for this reaction would be $3.5x10^3$ in vacuum. This value is in good agreement with Sharma et al.[48] in which the TNT + isopropylamine complex K_{eq} was reported to be $2.94x10^4$ in DMSO.

The ionization energy (IE) was calculated using Koopmans' theory[33] by MP2/6-311+G(3df,2p) and found to be 8.727 eV and the exothermic electron affinity (EA) was 0.093 eV. The IE energy of the complex represents a 2.74 eV shift compared to TNT while the EA of the two were within 0.1 eV of each other. TD-DFT calculations were performed using PBE0/6-311+G(d,p) in which the absorption energies and oscillator strength, given in parentheses, for the first 4 singlet excitations were found to be: 2.64 eV (0.1987), 3.46 eV (0.2069), 3.62 eV (0.0004), and 3.76 eV (0.0001). The predicted UV-Vis spectra of TNT and TNT-M were reported in **Figure 11**. These results place the HOMO and LUMO level at 8.727 and 6.09 eV, respectively. With this shift in the LUMO energy level, quenching of QD systems is much more likely. This observation apparently confirms our conclusions regarding semiconductor selections and the role of the Meisenheimer complex in the quenching reaction.

Figure 11. Predicted UV-Vis spectrum of TNT (black) and a TNT Meisenheimer complex with propylamine (blue) with TD-DFT PBE0/6-311+G(d,p). Solid traces correspond to units of absorptivity (left axis) while vertical lines relate to the oscillator strength (right axis).

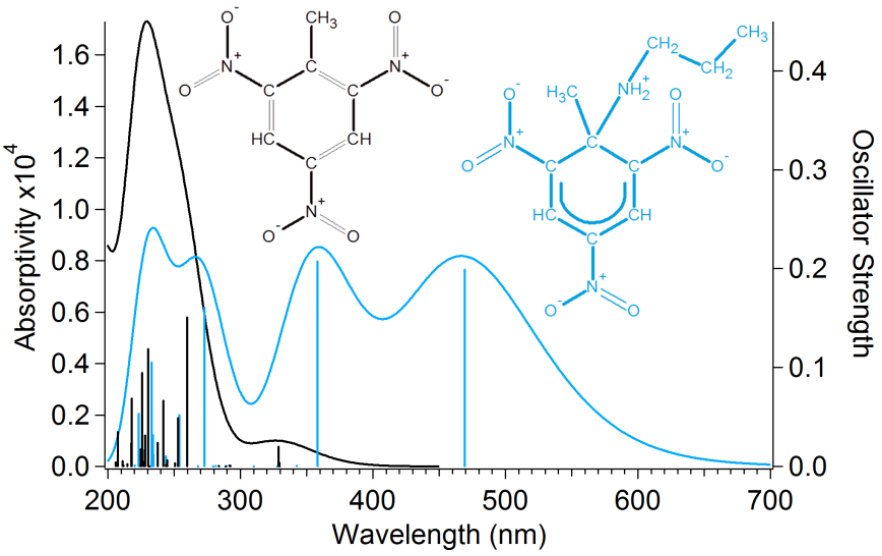

Additional observations of QD fluorescent quenching by 2,4,6-trinitrophenol (picric acid) have been reported. The Meisenheimer complex formed between picric acid (PA) and propylamine was examined in which the reaction enthalpy was calculated with B2PLYPD/6-311+G(3df,2p) and was -8.86 KJ mol^{-1}. This is 11.36 KJ mol^{-1} less than the Meisenheimer complex formed with TNT. Therefore, the expected ratio of Meisenheimer formation of TNT to PA is ~10:1. The IE and EA of PA were calculated by MP2/6-311+G(3df,2p) which were 11.214 and 0.583 eV as well as the picric acid Meisenheimer complex (PA-M) which were 9.121 and 0.194 eV, respectively. The first four singlet excitation absorption energies and (oscillator strengths) were calculated with TD-DFT PBE0/6-311+G(d,p) and were: 2.82 eV (0.203), 3.61 (0.186), 3.74 (0.003), and 3.824 (0.000). The predicted UV-Vis spectra of both the PA and PA-M complex were reported in **Figure 12**.

Figure 12. Predicted UV-Vis spectrum of picric acid (black) and a picric acid Meisenheimer complex formed with propylamine (red) with TD-DFT PBE0/6-311+G(d,p). Solid traces correspond to units of absorptivity (left axis) while vertical lines relate to the oscillator strength (right axis).

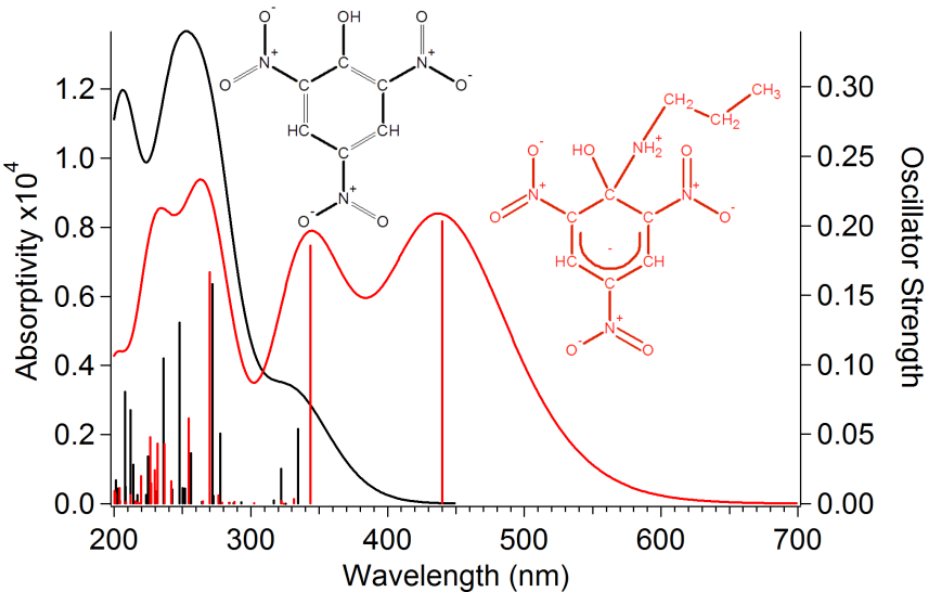

The LUMO level shift of the PA is very similar to that of the TNT-M complex. These results indicate that PA will quench QD PL less effectively than TNT which is consistent with some[18,20,25] and contradictory to other[21] reports. The energy level diagram of the TNT, TNT-M, PA, and PA-M was presented in **Figure 13**.

Figure 13. Energy level diagram of TNT, TNT Meisenheimer complex formed between TNT and propylamine (TNT-M), picric acid (PA), and picric acid Meisenheimer complex with propylamine (PA-M). The lowest energy level, corresponding to the HOMO, was calculated by MP2/6-311+G(3df,2p) and

determined using Koopmans' theory. Unoccupied energy levels were determined by TD-DFT PBE0/6-311+G(d,p).

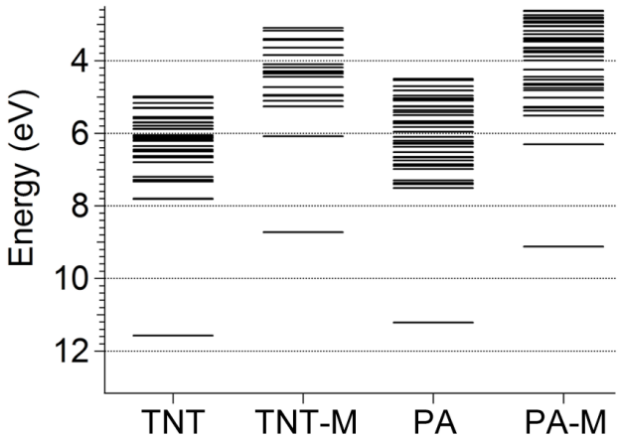

5.5 Conclusions

We have calculated the singlet excitations of six common explosives: RDX, β-HMX, TATP, HMTD, TNT, and PETN by TD-DFT methods including: PBE0, ωB97XD, CAM-B3LYP, and B3LYP with several basis sets including: 6-31G(d), 6-31+G(d), 6-31+G(d,p), and 6-311+G(d,p). The best agreement between experimentally determined absorption energies and those calculated by TD-DFT was with the PBE0 functional, with the smallest basis set of 6-31+G(d); however, all analysis was performed at the higher 6-311+G(d,p). In general, the long range corrected ωB97XD and CAM-B3LYP functionals performed identically in most cases and tended to predict higher absorption energies than PBE0 or B3LYP, while B3LYP predicted the lowest energy excitations. Natural transition orbitals were calculated for the major contributing oscillator components to the absorption spectra with PBE0/6-311+G(d,p). The results offer visualization of the hole and electron densities associated with UV to deep UV absorption. By combining IP_V at the CBS-

QB3 level and TD-DFT, energy level diagrams were reported for each of the six compounds. The energy level diagram can be utilized to assist in designing fluorescence quenching detection methods that utilize a donor/acceptor model like those proposed in QD and fluorescent polymer probe studies. Analysis of TNT and picric acid (PA) Meisenheimer complexes indicate the energetic shift of the HOMO level is responsible for the QD PL quenching observed while the uncoordinated TNT and PA are not predicted to be efficient quenchers for any II-VI semiconductor system except ZnO.

5.6 Supporting Info

Figure S1. Fits (colored Gaussians and gray open circles) generated for the experimentally measured UV-Vis spectra (black) of RDX, HMX, TNT, PETN, TATP, and HMTD in acetonitrile and the fit residuals (black dots).

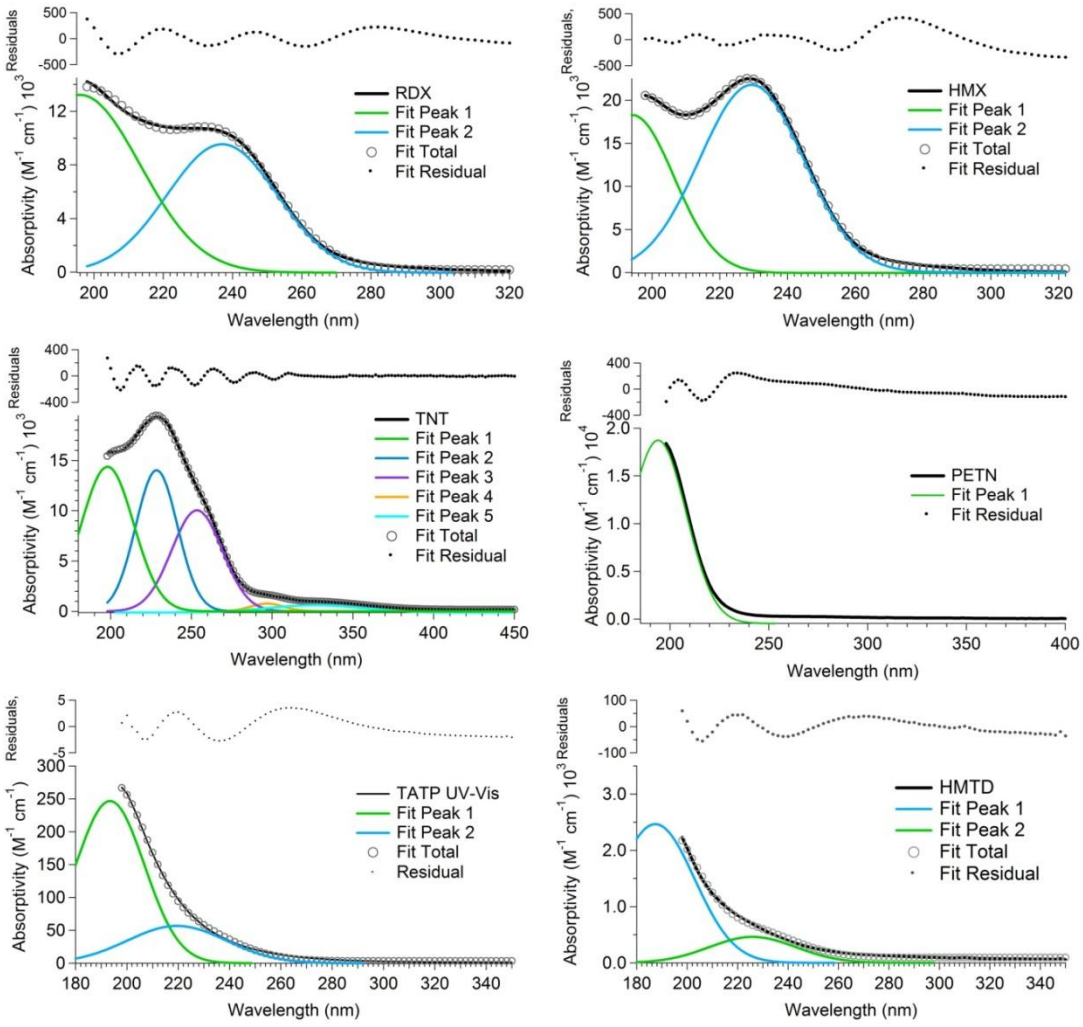

Figure S2. Absorption energies calculated by TDDFT PBE0 for four basis sets (6-31G(d), 6-31+G(d), 6-31+G(d,p), and 6-311+G(d,p)) for the six explosives (RDX, HMX, TATP, HMTD, TNT, and PETN). The size of the horizontal line is proportional to the oscillator strength. For several absorption energies, the actual oscillator strength is provided. For RDX, HMX, TATP, and TNT the magnitude of the first absorption oscillator strength is too small to be clearly visible on the plot so it has been accentuated with an arrow head.

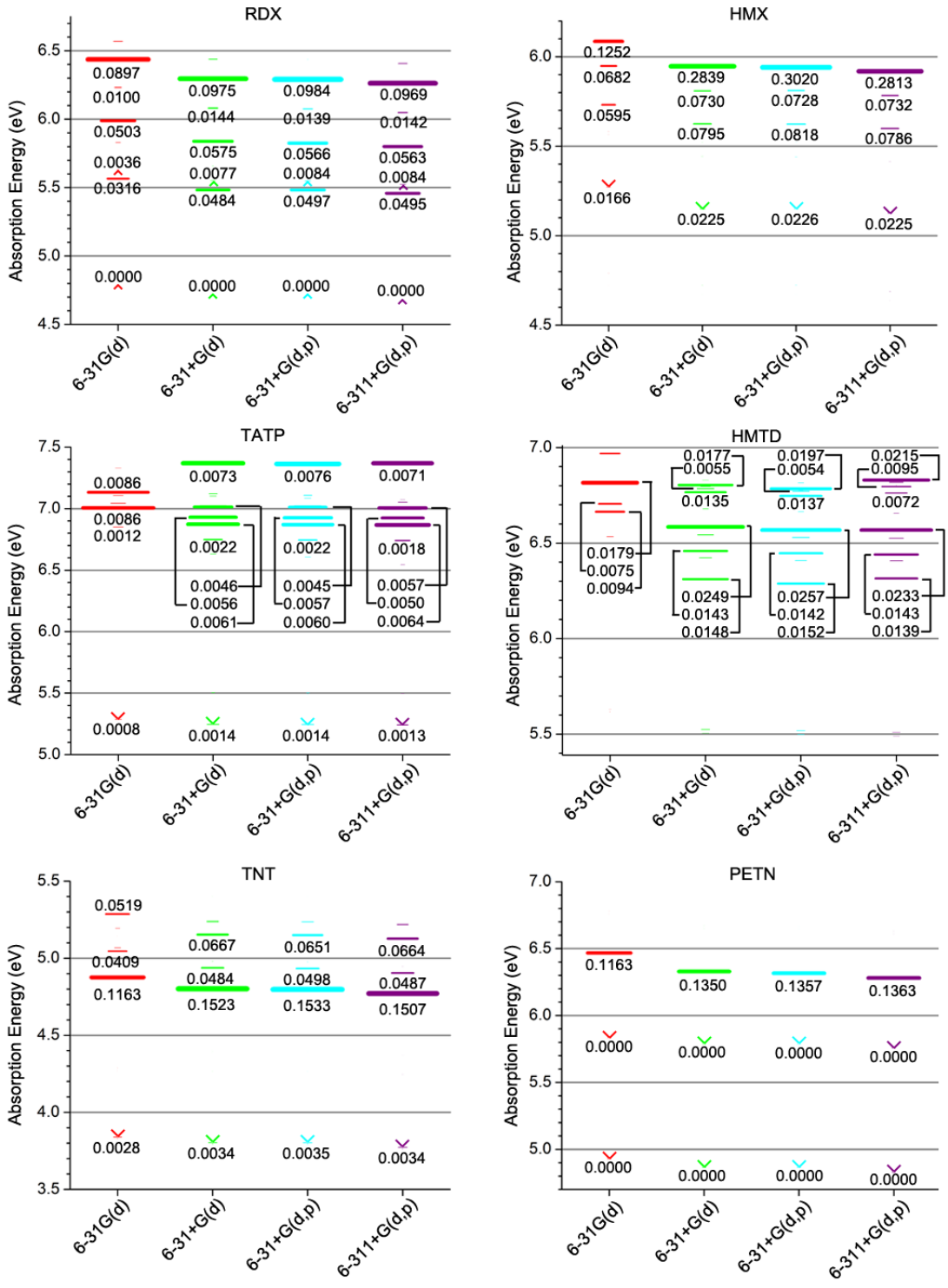
RDX
Absorption Energy (eV)
6.5
6.0
5.5
5.0
4.5
0.0897
0.0100
0.0503
0.0036
0.0316
0.0000
0.0975
0.0144
0.0575
0.0077
0.0484
0.0000
0.0984
0.0139
0.0566
0.0084
0.0497
0.0000
0.0969
0.0142
0.0563
0.0084
0.0495
0.0000
6-31G(d)
6-31+G(d)
6-31+G(d,p)
6-311+G(d,p)
HMX
Absorption Energy (eV)
6.0
5.5
5.0
4.5
0.1252
0.0682
0.0595
0.0166
0.2839
0.0730
0.0795
0.0225
0.3020
0.0728
0.0818
0.0226
0.2813
0.0732
0.0786
0.0225
6-31G(d)
6-31+G(d)
6-31+G(d,p)
6-311+G(d,p)
TATP
Absorption Energy (eV)
7.5
7.0
6.5
6.0
5.5
5.0
0.0086
0.0086
0.0012
0.0008
0.0073
0.0022
0.0046
0.0056
0.0061
0.0014
0.0076
0.0022
0.0045
0.0057
0.0060
0.0014
0.0071
0.0018
0.0057
0.0050
0.0064
0.0013
6-31G(d)
6-31+G(d)
6-31+G(d,p)
6-311+G(d,p)
HMTD
Absorption Energy (eV)
7.0
6.5
6.0
5.5
0.0179
0.0075
0.0094
0.0177
0.0055
0.0135
0.0249
0.0143
0.0148
0.0197
0.0054
0.0137
0.0257
0.0142
0.0152
0.0215
0.0095
0.0072
0.0233
0.0143
0.0139
6-31G(d)
6-31+G(d)
6-31+G(d,p)
6-311+G(d,p)
TNT
Absorption Energy (eV)
5.5
5.0
4.5
4.0
3.5
0.0519
0.0409
0.1163
0.0028
0.0667
0.0484
0.1523
0.0034
0.0651
0.0498
0.1533
0.0035
0.0664
0.0487
0.1507
0.0034
6-31G(d)
6-31+G(d)
6-31+G(d,p)
6-311+G(d,p)
PETN
Absorption Energy (eV)
7.0
6.5
6.0
5.5
5.0
0.1163
0.0000
0.0000
0.1350
0.0000
0.0000
0.1357
0.0000
0.0000
0.1363
0.0000
0.0000
6-31G(d)
6-31+G(d)
6-31+G(d,p)
6-311+G(d,p)

Figure S3. Calculated UV-Vis spectrum with TDDFT PBE0/6-311+G(d,p) of RDX (black), HMX (purple), PETN (cyan), TNT (green), TATP (yellow), and HMTD (red) with IEFPCM solvent model with acetonitrile (solid trace) and in the gas phase (dotted trace).

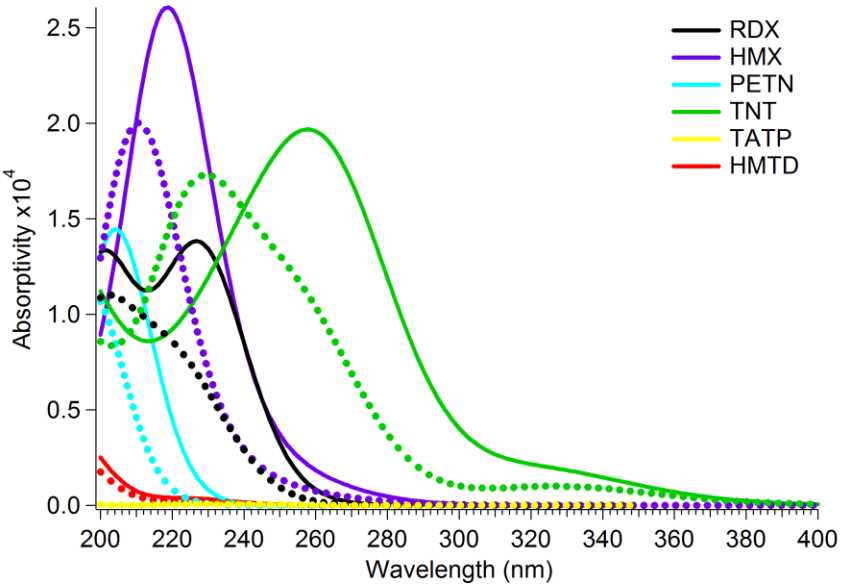

5.7 References

1. Mullen, C.; Huestis, D.; Coggiola, M.; Oser, H. Laser photoionization of triacetone triperoxide (TATP) by femtosecond and nanosecond laser pulses. *Int. J. Mass Spectrom.* **2006**, 252, 69-72.

2. Mullen, C.; Irwin, A.; Pond, B. V.; Huestis, D. L.; Coggiola, M. J.; Oser, H. Detection of explosives and explosives-related compounds by single photon laser ionization time-of-flight mass spectrometry. *Anal. Chem.* **2006**, 78, 3807-3814.

3. Marshall, A.; Clark, A.; Jennings, R.; Ledingham, K. W. D.; Sander, J.; Singhal, R. P. Laser-induced dissociation, ionization and fragmentation processes in nitroaromatic molecules. *Int. J. Mass Spectrom. Ion Processes* **1992**, 116, 143-156.

4. Cabalo, J.; Sausa, R. Trace detection of explosives with low vapor emissions by laser surface photofragmentation-fragment detection spectroscopy with an improved ionization probe. *Appl. Opt.* **2005**, 44, 1084-1091.

5. Oxley, J. C.; Smith, J. L.; Kirschenbaum, L. J.; Marimganti, S.; Vadlamannati, S. Detection of explosives in hair using ion mobility spectrometry. *J. Forensic Sci.* **2008**, 53, 690-693.

6. Creaser, C. S.; Griffiths, J. R.; Bramwell, C. J.; Noreen, S.; Hill, C. A.; Thomas, C. L. P. Ion mobility spectrometry: a review. Part 1. Structural analysis by mobility measurement. *Analyst* **2004**, 129, 984-994.

7. Borch, T.; Gerlach, R. Use of reversed-phase high-performance liquid chromatography–diode array detection for complete separation of 2, 4, 6-trinitrotoluene metabolites and EPA Method 8330 explosives: influence of temperature and an ion-pair reagent. *J. Chromatogr., A* **2004**, 1022, 83-94.

8. Schulte-Ladbeck, R.; Kolla, P.; Karst, U. Trace Analysis of Peroxide-Based Explosives. *Anal. Chem.* **2003**, 75, 731-735.

9. Crowson, A.; Beardah, M. S. Development of an LC/MS method for the trace analysis of hexamethylenetriperoxidediamine (HMTD). *Analyst* **2001**, 126, 1689-1693.

10. Tuschel, D. D.; Mikhonin, A. V.; Lemoff, B. E.; Asher, S. A. Deep Ultraviolet Resonance Raman Excitation Enables Explosives Detection. *Appl. Spectrosc.* **2010**, 64, 425-432.

11. Fang, X.; Ahmad, S. Detection of explosive vapour using surface-enhanced Raman spectroscopy. *Appl. Phys. B: Lasers Opt.* **2009**, 97, 723-726.

12. Lin, H.; Suslick, K. S. A Colorimetric Sensor Array for Detection of Triacetone Triperoxide Vapor. *J. Am. Chem. Soc.* **2010**, 132, 15519-15521.

13. Reynolds, J.; Nunes, P.; Whipple, R.; Alcaraz, A. In *Detection and Disposal of Improvised Explosives*; Schubert, H., Kuznetsov, A., Eds.; Springer: The Netherlands, 2006; Vol. 6, p 27-32.

14. Germain, M. E.; Knapp, M. J. Turn-on fluorescence detection of H2O2 and TATP. *Inorg. Chem.* **2008**, 47, 9748-9750.

15. Gao, D.; Wang, Z.; Liu, B.; Ni, L.; Wu, M.; Zhang, Z. Resonance energy transfer-amplifying fluorescence quenching at the surface of silica nanoparticles toward ultrasensitive detection of TNT. *Anal. Chem.* **2008**, 80, 8545-8553.

16. Shi, G. H.; Shang, Z. B.; Wang, Y.; Jin, W. J.; Zhang, T. C. Fluorescence quenching of CdSe quantum dots by nitroaromatic explosives and their relative compounds. *Spectrochimica Acta Part A: Molecular and Biomolecular Spectroscopy* **2008**, 70, 247-252.

17. Zhang, K.; Zhou, H.; Mei, Q.; Wang, S.; Guan, G.; Liu, R.; Zhang, J.; Zhang, Z. Instant Visual Detection of Trinitrotoluene Particulates on Various Surfaces by Ratiometric Fluorescence of Dual-Emission Quantum Dots Hybrid. *J. Am. Chem. Soc.* **2011**.

18. Chen, Y.; Chen, Z.; He, Y.; Lin, H.; Sheng, P.; Liu, C.; Luo, S.; Cai, Q. L-cysteine-capped CdTe QD-based sensor for simple and selective detection of trinitrotoluene. *Nanotechnology* **2010**, 21, 125502.

19. Xia, Y.; Song, L.; Zhu, C. Turn-On and Near-Infrared Fluorescent Sensing for 2, 4, 6-Trinitrotoluene Based on Hybrid (Gold Nanorod)-(Quantum Dots) Assembly. *Anal. Chem.* **2011**, 83, 1401-1407.

20. Freeman, R.; Finder, T.; Bahshi, L.; Gill, R.; Willner, I. Functionalized CdSe/ZnS QDs for the Detection of Nitroaromatic or RDX Explosives. *Adv. Mater. (Weinheim, Ger.)* **2012**, 24, 6416-6421.

21. Tu, R.; Liu, B.; Wang, Z.; Gao, D.; Wang, F.; Fang, Q.; Zhang, Z. Amine-capped ZnS-Mn2+ nanocrystals for fluorescence detection of trace TNT explosive. *Anal. Chem.* **2008**, 80, 3458-3465.

22. Fant, F.; De Sloovere, A.; Matthijsen, K.; Marlé, C.; El Fantroussi, S.; Verstraete, W. The use of amino compounds for binding 2,4,6-trinitrotoluene in water. *Environ. Pollut.* **2001**, 111, 503-507.

23. McQuade, D. T.; Pullen, A. E.; Swager, T. M. Conjugated polymer-based chemical sensors. *Chem. Rev.* **2000**, 100, 2537-2574.

24. Sohn, H.; Calhoun, R. M.; Sailor, M. J.; Trogler, W. C. Detection of TNT and picric acid on surfaces and in seawater by using photoluminescent polysiloles. *Angewandte Chemie International Edition* **2001**, 40, 2104-2105.

25. Sanchez, J. C.; Trogler, W. C. Efficient blue-emitting silafluorene–fluorene-conjugated copolymers: selective turn-off/turn-on detection of explosives. *J. Mater. Chem.* **2008**, 18, 3143-3156.

26. Sanchez, J. C.; DiPasquale, A. G.; Rheingold, A. L.; Trogler, W. C. Synthesis, Luminescence Properties, and Explosives Sensing with 1, 1-Tetraphenylsilole-and 1, 1-Silafluorene-vinylene Polymers. *Chem. Mater.* **2007**, 19, 6459-6470.

27. Toal, S. J.; Magde, D.; Trogler, W. C. Luminescent oligo (tetraphenyl) silole nanoparticles as chemical sensors for aqueous TNT. *Chem. Commun.* **2005**, 1, 5465-5467.

28. Sohn, H.; Sailor, M. J.; Magde, D.; Trogler, W. C. Detection of nitroaromatic explosives based on photoluminescent polymers containing metalloles. *J. Am. Chem. Soc.* **2003**, 125, 3821-3830.

29. Martinez, H. P.; Grant, C. D.; Reynolds, J. G.; Trogler, W. C. Silica anchored fluorescent organosilicon polymers for explosives separation and detection. *J. Mater. Chem.* **2012**, 22, 2908-2914.

30. Weickhardt, C.; Tönnies, K. Short pulse laser mass spectrometry of nitrotoluenes: ionization and fragmentation behavior. *Rapid Commun. Mass Spectrom.* **2002**, 16, 442-446.

31. Hankin, S. M.; Tasker, A. D.; Robson, L.; Ledingham, K. W. D.; Fang, X.; McKenna, P.; McCanny, T.; Singhal, R. P.; Kosmidis, C.; Tzallas, P.et al. Femtosecond laser time-of-flight mass spectrometry of labile molecular analytes: laser-desorbed nitro-aromatic molecules. *Rapid Commun. Mass Spectrom.* **2002**, 16, 111-116.

32. Strehmel, B.; Sarker, A. M.; Detert, H. The Influence of σ and π Acceptors on Two-Photon Absorption and Solvatochromism of Dipolar and Quadrupolar Unsaturated Organic Compounds. *ChemPhysChem* **2003**, 4, 249-259.

33. Cooper, J. K.; Grant, C. D.; Zhang, J. Z. Ab initio calculation of ionization potential and electron affinity of six common explosive compounds. *Reports in Theoretical Chemistry* **2012**, 1, 11-19.

34. Martin, R. L. Natural transition orbitals. *J. Chem. Phys.* **2003**, 118, 4775.

35. Jakubikova, E.; Snoeberger Iii, R. C.; Batista, V. S.; Martin, R. L.; Batista, E. R. Interfacial Electron Transfer in TiO2 Surfaces Sensitized with Ru(II)−Polypyridine Complexes†. *J. Phys. Chem. A* **2009**, 113, 12532-12540.

36. Becke, A. D. Density-functional thermochemistry. IV. A new dynamical correlation functional and implications for exact-exchange mixing. *J. Chem. Phys.* **1996**, 104, 1040.

37. Yanai, T.; Tew, D. P.; Handy, N. C. A new hybrid exchange–correlation functional using the Coulomb-attenuating method (CAM-B3LYP). *Chem. Phys. Lett.* **2004**, 393, 51-57.

38. Chai, J. D.; Head-Gordon, M. Long-range corrected hybrid density functionals with damped atom–atom dispersion corrections. *Phys. Chem. Chem. Phys.* **2008**, 10, 6615-6620.

39. Adamo, C.; Barone, V. Toward reliable density functional methods without adjustable parameters: The PBE0 model. *J. Chem. Phys.* **1999**, 110, 6158.

40. Adamo, C.; Scuseria, G. E.; Barone, V. Accurate excitation energies from time-dependent density functional theory: Assessing the PBE0 model. *J. Chem. Phys.* **1999**, 111, 2889.

41. Jacquemin, D.; Wathelet, V.; Perpète, E. A.; Adamo, C. Extensive TD-DFT benchmark: singlet-excited states of organic molecules. *J. Chem. Theory Comput.* **2009**, 5, 2420-2435.

42. Frisch, M. J.; Trucks, G. W.; Schlegel, H. B.; Scuseria, G. E.; M. A. Robb; Cheeseman, J. R.; Scalmani, G.; Barone, V.; Mennucci, B.; Petersson, G. A.et al. Gaussian 09. **2009**.

43. Sandus, O.; Slagg, N. *Mechanism of the Formation of Pink Water*, DTIC Document, 1978.

44. Stals, J.; Barraclough, C. G.; Buchanan, A. S. Molecular orbital interpretation of the ultra-violet absorption spectra of unconjugated aliphatic nitramines. *Transactions of the Faraday Society* **1969**, 65, 904-914.

45. Mullen, P. A.; Orloff, M. K. Ultraviolet absorption spectrum of pentaerythritol tetranitrate. *J. Phys. Chem.* **1973**, 77, 910-911.

46. Walukiewicz, W. Intrinsic limitations to the doping of wide-gap semiconductors. *Physica B: Condensed Matter* **2001**, 302–303, 123-134.

47. Van de Walle, C. G.; Neugebauer, J. Universal alignment of hydrogen levels in semiconductors, insulators and solutions. *Nature* **2003**, 423, 626-628.

48. Sharma, S.; Lahiri, S. Absorption spectroscopic and FTIR studies on EDA complexes between TNT (2, 4, 6-trinitrotoluene) with amines in DMSO and determination of the vertical electron affinity of TNT. *Spectrochimica Acta Part A: Molecular and Biomolecular Spectroscopy* **2008**, 70, 144-153.

Chapter 6. Exciton Dynamics of CdS Thin Films Produced by Chemical Bath Deposition and DC Pulse Sputtering

6.1 Abstract

Two CdS thin film samples deposited on glass substrates for use as a window layer in CdTe and copper indium gallium diselenide (CIGS) solar cells were studied. The samples were prepared by direct current pulse sputtering (DCPS) and chemical bath deposition (CBD) which were studied by UV-Vis, SEM, XRD, and ultrafast transient absorption (TA) spectroscopy. The exciton and charge carrier dynamics and of the two films within the first 1 ns following photoexcitation were studied by a white light probe. Singular value decomposition of the differential absorption spectrum was performed, in which the time dependence of the bleach recovery was fit globally with a multiexponential function to uncover the spectra of different transient species. The excited electrons of the DCPS sample decays through 1.8, 8, 65, and 450 ps time constants attributed to donor level electron trapping, valence band (VB) → conduction band (CB) recombination, shallow donor recombination, and deep donor recombination, respectively. The CBD sample has time constants of 6, 65, and 450 ps which were attributed to CB→VB recombination, sulfur vacancies (V_S) recombination, and V_S→ oxygen interstitial (O_i) donor acceptor pair (DAP) recombination, respectively. It was concluded that the DCPS deposition technique produces films of lower defect density and improved carrier dynamics, which are desired for use in solar cell applications.

6.2 Introduction

The CdS/CdTe and CdS/CIGS (copper indium gallium diselenide) thin film solar cells have proven promising alternatives to Si for light harvesting. Currently, the world record efficiency for CIGS is 20.4% set by Empa's Laboratory for Thin Film and Photovolatics up from their previous 18.7% efficient cells.[1] In these systems, a p-n junction is formed between the n-type CdS window layer and p-type absorber layer. Fabrication of these layers has been an area of intensive research. Common methods of depositing the CdS layer include the use of chemical bath deposition (CBD),[2] sputtering,[3] electrochemical,[4] close space sublimation (CSS),[2] laser ablation,[5,6] vapor transport,[7] spray pyrolysis,[8] and others. The intrinsic defect density produced by these techniques is an important factor for device performance and is the main focus of this work.

The native defects of CdS have been extensively studied by low temperature photoluminescence (PL)[9] for a variety of synthesis and treatment methodologies including close space sublimation (CSS),[10,11] laser ablation,[11] chemical bath deposition (CBD),[10-13] sputtering.[11,14] As-grown close space sublimation (CSS) films have a dominant yellow PL band from 2.07 to 2.18 eV related to donor acceptor pair (DAP) recombination between cadmium interstitials (Cd_i) or sulfur vacancies (V_S) donor and an impurity acceptor.[10] CBD films are reported to have a red PL band between 1.59 to 2.00 eV due to surface states and V_S.[10] DAP recombination in CBD films have also been reported to be 2.349 eV.[13] The V_S^{2+} has been reported to exist 2.175 eV above the valence band edge (E_v + 2.175 eV) with Cd_i^+ and sulfur

interstitials (S_i^-) found at E_v + 2.012 eV and E_c – 2.275 eV, respectively.[13,15] CBD prepared films are also reported to be dominated by red emission at 1.72 eV related to V_S while RF-sputtering produced films with increased Cd_i identified by PL from 2.10 to 2.40 eV.[11] Additionally, positron annihilation spectroscopy (PAS) has identified Cd vacancies (V_{Cd}) in CBD crystals[16] as well as clustered neutral defects.[17]

Doping of CdS has also been studied in which acceptor dopants are added in an effort to produce a p-type material. Inadvertent doping with oxygen during CBD deposition is common and is often not addressed or characterized in the literature but can reach values of 12 atom%.[18-20] CBD films were found to contain an atom% ratio of Cd:S:O of 45.7:42.5:11.8 by XPS.[20] Substitutional oxygen (O@S) was studied by density functional theory (DFT) but the oxygen 2p states did not alter the bandgap of CdS.[21] Other studies have found similar results in that substitutional oxygen is electrically inactive.[22] However, oxygen defects have been characterized as acceptor states at E_V + 116 meV when added to CdS by ion implantation.[23,24] The presence of oxygen can also influence intrinsic defect formation[25] as well as crystalline grain size and optical absorption energy.[26] In the case of ZnSe oxygen is suggested to dope the lattice interstitially, breaking the Zn-Se bond to attach to the Zn thereby causing a Se dangling bond.[22]

Herein, we have examined two CdS thin film deposition methods, CBD and DC pulsed sputtering (DCPS), for the fabrication of CdS window layers for solid state solar cell applications. Characterization of the physical morphology and crystallinity

of the as-deposited films was accomplished by SEM and XRD. The ultrafast exciton dynamics of photoexcited charge carriers in the two materials was characterized by femtosecond pump probe spectroscopy. Data analysis using the technique of singular value decomposition (SVD) global fitting was employed to obtain the lifetime and wavelength dependence of the various recombination mechanisms of the exciton. The results are discussed in the context of defect related recombination and comparisons are drawn between the two deposition methods. Insights gained from these studies are important for developing improved semiconductor thin films for solar energy conversion and other photonics applications.

6.3 Experimental

6.3.1 Sample Preparation

6.3.1.1 DC-Pulse Sputtering

The sputtered film was prepared by applying direct current pulses to a CdS target. The deposition was carried out in an argon atmosphere at 10 mTorr and 500 W. The bipolar asymmetric pulsed direct current power was 100 kHz, and the reverse time is 3 μs.

6.3.1.2 Chemical Bath Deposition

CBD CdS film was deposited through a heterogeneous reaction on a glass substrate. The reactants were comprised of cadmium acetate, ammonium acetate, ammonium hydroxide, and thiourea. The temperature of the solution was maintained at 92 °C, and the reactants were continuously stirred at 400 rpm. The deposition time

was 20 minutes, after which the substrate was rinsed with DI water, dried by spinning, and baked on a hot plate for 10 minutes at 110°C.

6.3.2 Optical and Morphological Characterization

6.3.2.1 Optical and Morphological Characterization of CdS Thin Films

Absorption spectra were collected of the CdS thin films with a Hewlett Packard 845A diode array UV-Visable spectrometer. A FEI Quanta 3D FEG Dualbeam scanning electron microscope (SEM) was used to image the two films. The films were grounded with copper tape and imaged with an accelerating voltage of 5 kV, a current of 11.8 pA, and a working distance between 9 and 11 mm. Grazing incidence x-ray diffraction was collected of the thin films using a Rigaku SmartLab x-ray diffractometer with a Cu-Kα source (0.0100 degrees step, 3.0000 deg min^{-1} scan speed). The sample diffraction spectra were compared to the ICDD PDF-2/Release 2011 database for peak identification.

6.3.2.2 Transient Absorption Spectroscopy

Ultra-fast transient absorption pump-probe spectroscopy was conducted with a Quantronix laser system consisting of a Palitra-FS optical parametric amplifier pumped by an Integra-C Ti:Sapphire amplifier system. This system has been described in detail elsewhere.[27] Briefly, 795 nm, 820 mW, 150 fs pulses from Integra-C were split 9:1 between an optical parametric amplifier (OPA) and sapphire crystal, respectively. A white light continuum from 450-800 nm was generated in the sapphire crystal. The OPA was tuned to 460 nm (2.7 eV) and attenuated with neutral

density (ND) filters to probe the samples at five different excitation intensities, which were: 707, 220, 86, 46, and 24 nJ/pulse for the DCPS sample, and 890, 195, 86, 54, and 20 nJ/pulse for the CBD sample. The differential absorption (dA) spectrum was collected over a pump probe delay period of 1,000 ps consisting of an average forward (-2→1000 ps) and reverse (1000 → -2 ps) scans where 400 spectra were averaged per data point.

The TA spectra were analyzed with singular value decomposition (SVD) global fitting (GF) procedures written in-house for Matlab, the method of which has been previously described.[28] To confirm and support SVD-GF results, single wavelength fitting for the DCPS and CBD samples were done at 510 and 490 nm, respectively.

6.4 Results and Discussion

6.4.1 Sample Morphology

The CdS thin film sample morphology was analyzed with SEM for both the DCPS and CBD deposition techniques, representative images were reported in **Figure 1 (A-C)** and **(D-F)**, respectively. The DCPS CdS film thickness was 100 nm and was uniformly spread across the glass surface as a dense smooth coating made up of small (20-30 nm) grains roughly spherical in shape, as determined by a perpendicular view of the films surface. The CBD sample was approximately 70 nm thick and was made up of more loosely packed globular to spherically shaped grains

roughly 60 to 80 nm in size. Also seen were larger, loosely scattered grains on the order of 160 to 250 nm.

Figure 1: Sample morphology of CdS films deposited by DC pulse sputtering (DCPS), top, and chemical bath deposition (CBD), bottom. A/D: SEM image at 74° tilt angle, 150k x magnification (A) and 20k x magnification (D); B/E: SEM image perpendicular to the substrate, 120k x magnification (B) and 50k x magnification (E); C/F photos of CdS coated glass slides collected against a white background and then digitally altered to blue to improve contrast.

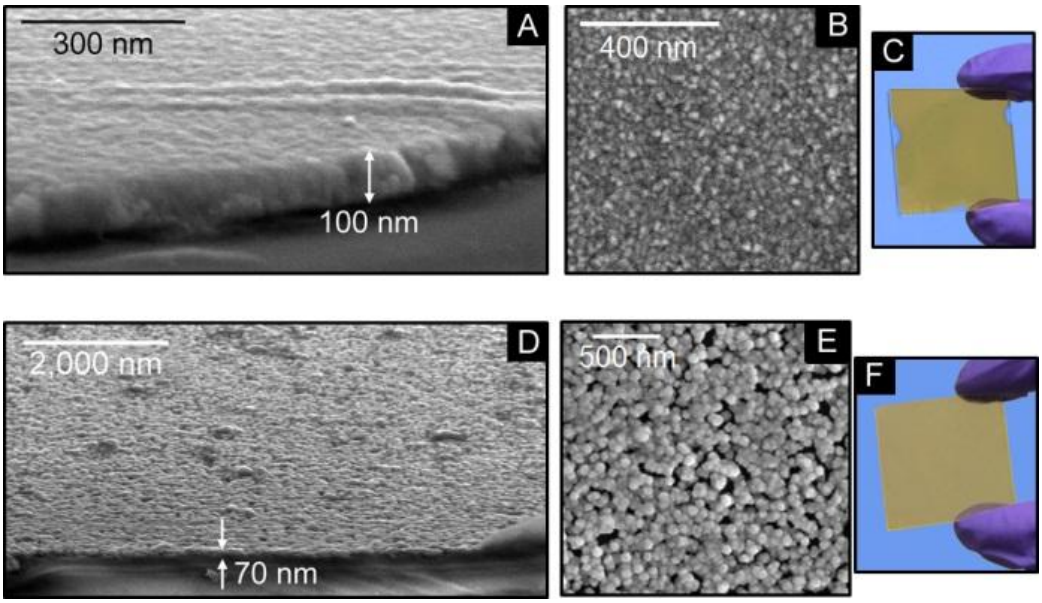

The crystallinity of the films was characterized using grazing incidence x-ray diffraction for the DCPS and CBD thin films, **Figure 2**. The DCPS sample was hexagonal and the CBS sample was cubic. In addition, the DCPS had increased crystallinity compared to the CBD sample as evidenced by the sharp and intense (002) peak.

Figure 2. Grazing incidence x-ray diffraction of DCPS (top) and CBD (bottom) deposited CdS thin films on glass. Reference diffraction peaks are shown as short vertical lines and Miller indices provided for observed diffraction peaks.

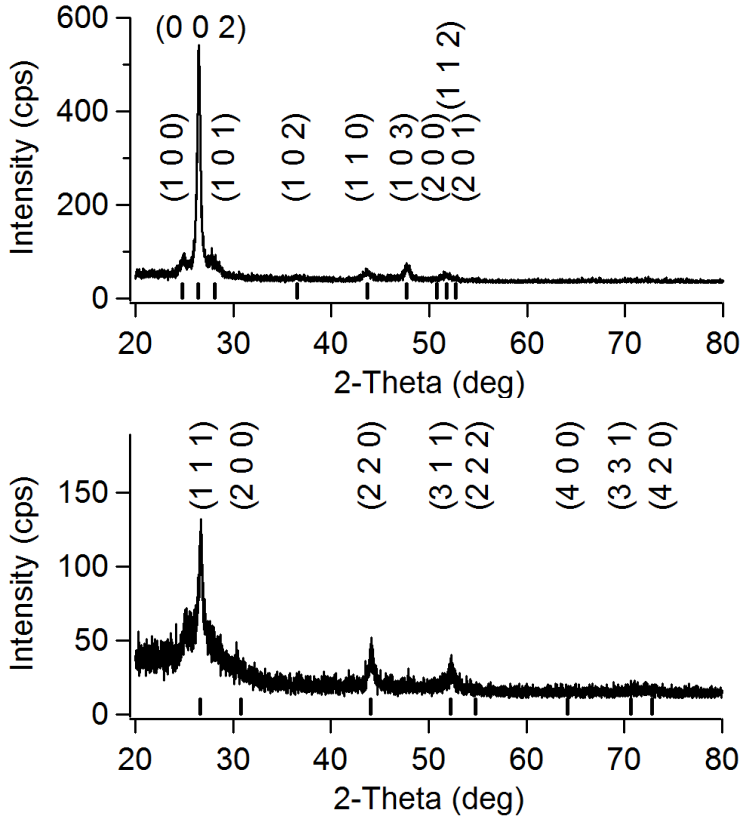

6.4.2 UV-Vis Spectroscopy

The absorption spectra of the CdS thin films deposited by DC-PS and CBD were reported in **Figure 3**. Both samples have a first exciton peak at 486 nm (2.55 eV) which is consistent with the free electron absorption energy of bulk CdS.[29] Also shown in **Figure 3** is the laser line used to excite the CdS samples during the TA measurements.

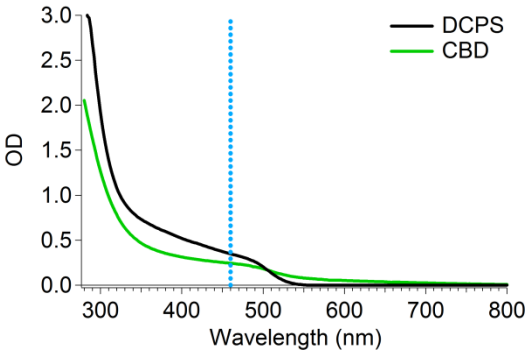

Figure 3. UV-Vis absorption spectrum of CdS thin films coated on glass by DC pulse sputtering (DCPS), solid line, and chemical bath deposition (CBD), dotted line. Vertical broken line at 460 nm indicates the laser line used to excite the samples during transient absorption experiments.

6.4.3 Transient Absorption Spectroscopy

The transient differential absorption (dA) spectra were recorded using a 460 nm pump and white light probe (450-800 nm) for the DCPS and CBD samples over the interval from 0 to 1,000 ps delay between the pump and probe pulses. The wavelength dependent transient absorption (excited state absorption) and transient bleach (ground state depletion) recoveries were visualized by a 3-D plot reported in **Figure 4 (A/C)** for the two samples, respectively, and a 2-D topographical plot shown in **Figure 4 (B/C)**. The DCPS sample has a transient absorption feature at 450-470 nm, which did not fully recover to zero over the pump probe delay interval examined. There was also an asymmetric Gaussian transient bleach feature with λ_{max} = 510 nm, which recovered a majority of its amplitude within the pulse-width limited rise and 100 ps, with a fraction of the amplitude persisting through the remainder of

the delays recorded. The CBD sample has a strong transient absorption feature below 450 nm, with significant amplitude out to 1000 ps. The transient bleach in this sample was blue shifted with respect to that of the DCPS sample, and was an asymmetric Gaussian feature with a λ_{max} = 490 nm. The pulse-width limited rise of the transient bleach recovered a majority of its amplitude before 200 ps delay, the remainder of which extended out to 1000 ps. The bleach feature width was broadened in the CBD sample.

Figure 4. Transient absorption differential absorption spectrum of CdS thin films deposed on glass by DCPS (A/B) and CBD (C/D) covering 1000 ps pump probe delay for wavelengths between 450-800 nm displayed in ¾ (A/C) and top down (B/D) views. Pump = 460 nm.

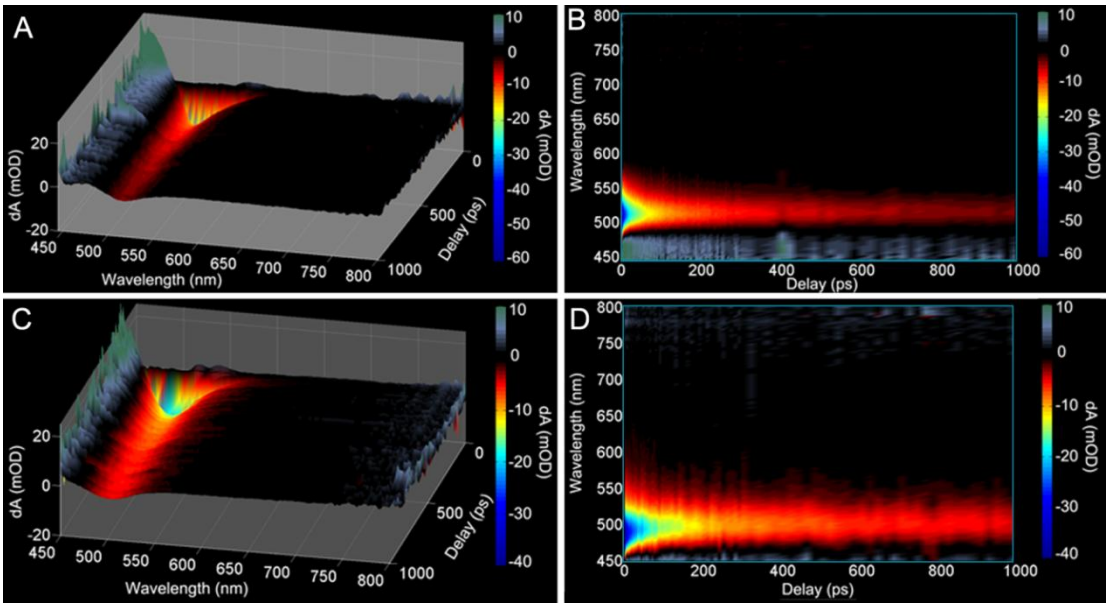

6.4.3.1 Single Wavelength Fitting

Single wavelength time profiles were extracted from the data shown above for the λ_{max} of the transient bleach feature and shown normalized in **Figure 5** (510 and 490 nm for DCPS and CBD, respectively). From this plot, it is seen that the time profiles recover with a fast, medium, and slow time constant. The two samples show very similar recoveries and differ primarily in the amplitude of the middle lifetime component, with the CBD sample having a larger amplitude in this region.

The bleach recoveries were fit with a triple exponential function, **Equation 1**. Both time profiles could be fit with lifetimes of 8, 65, and 980 ps. The fit results were also shown (red lines) in **Figure 5**. From the single wavelength fits, the difference is small between the two samples, especially when lifetimes are concerned. While the CBD sample has a larger amplitude for the medium decay, direct assignments regarding exciton dynamics are quite challenging. The samples differ in synthesis method, crystalline phase, and oxygen content; a more complete analysis technique is required to extract spectroscopic features, which can

Figure 5. Normalized time dependence of the differential absorption for CdS thin films deposited by DCPS (blue) and CBD (green) circles for probe wavelengths 510 nm (DCPS) and 490 nm (CBD) probe. Triple exponential fit results are displayed as solid red lines. Fit lifetimes were 8, 65, and 980 ps.

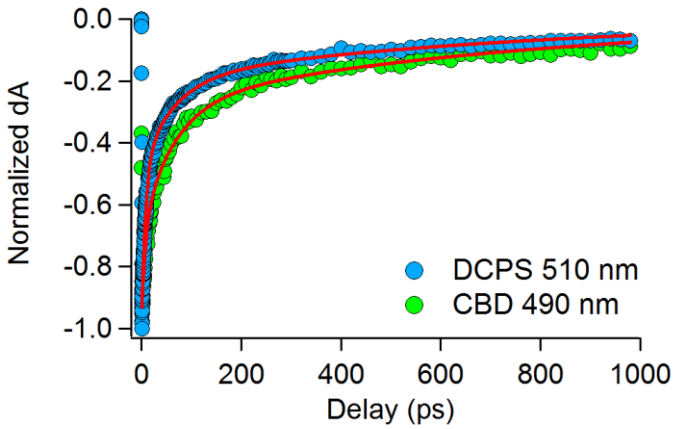

help to elucidate the effects of these differences on the exciton recombination dynamics.

$$y(\lambda, t) = y_0 + \sum_{i=1}^{n} A_i(\lambda) \exp\left(\frac{-t}{\tau_i}\right) \quad (1)$$

6.4.3.2 Singular Value Decomposition

For transient absorption utilizing continuum probes, rich time dependent spectroscopic information can be obtained so long as one can deconvolute the time and wavelength dependence of the data. The aims of doing so would be to obtain a single time constant for a given decay process which will have no significant wavelength dependence. While determining the lifetime of a given process can be a valuable tool for understanding recombination processes, semiconductor dynamics more complicated than an ideal two-level system, and thus often have multiexponential recoveries which can be difficult to assign to a specific transition. A greater depth of understanding can be gained from examining the wavelength dependent initial amplitude of each lifetime component. We have applied this analysis technique successfully to ZnSe:Cu,[30] core/shell/shell CdSe/ZnSe/ZnS,[31] and alloyed $Cd_xZn_{(1-x)}Se$/ZnSe/ZnS[32] systems to deconvolute time resolved fluorescence and transient absorption peaks into separate spectral peaks that decay with single exponential lifetimes, thereby allowing for a more detailed discussion of the exciton recombination pathways associated with each lifetime component.

Convoluted data of pump probe time delay, probe wavelength, and signal intensity (dA in our case) can be easily addressed with singular value decomposition

(SVD). This is the case for a given vector in three dimensional space in that orthogonal x, y, and z components of the vector may be described separately. Such is also the case with a convoluted n x m matrix of TA data. The SVD deconvolution produces a set of three matrices: an orthogonal n x n U matrix which depends only on wavelength (in our case), an orthogonal m x m V matrix depending on time, and n x m x Σ diagonal matrix containing eigenvalues. These eigenvalues are relative magnitudes of the respective column vectors contained in the U and V matrices in the original data. The SVD theorem is presented as **Equation 2**, in which V^* is the transpose of V.

$$M = U\Sigma V^* \tag{2}$$

An example of this procedure is shown in **Figure 6** for the DCPS CdS thin film sample excited with a pump energy of 220 nJ $pulse^{-1}$. **Figure 6 (A)** shows the first two columns of the U matrix (red and blue), as well as the raw data at ten pump probe delay times (black → light gray, decreasing in black density at longer time delays). In this plot, the first column vector contains the majority of the sample decay, while the second column vector is primarily due to the rise component of the data. This point is also evident in the V matrix, **Figure 6 (B)**, where the pulse-width (150 fs) limited rise is clearly visible as a sharp feature at early times of column 2. The column 1 vector contains the time dependence of the sample deconvoluted from the chirp and instrument response function (IRF). Also shown in **Figure 6 (C)** are the eigenvalues of the diagonal Σ matrix, indicating that the first and second column

vectors in the V and U matrices contain the majority of the actual data. The remaining components of the U and V matrices have no time or wavelength dependence which indicates they are due to noise in the data. This is an added advantage of SVD, in that the SVD deconvolution filters a vast majority of unwanted noise and unwanted column vectors can be discarded.

Figure 6. Example of singular value decomposition of convoluted wavelength vs. delay vs. dA transient absorption pump probe spectroscopy of CdS DCPS thin film data (220 nJ/pulse) into a wavelength dependent U matrix (top), a delay dependent V matrix (middle), and Σ matrix of eigenvalues. The first two column vectors of (1): red and (2): blue contribute to the majority of the data.

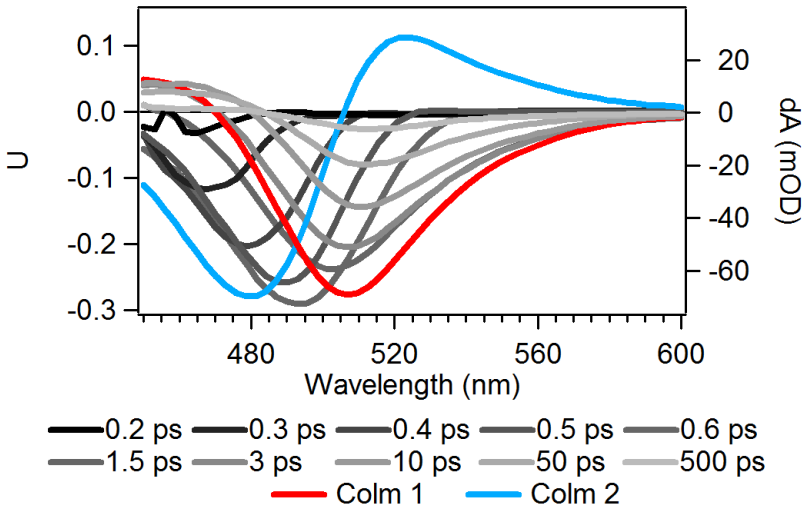
0.1
0.0
-0.1
-0.2
-0.3
U
20
0
-20
-40
-60
dA (mOD)
480
520
560
600
Wavelength (nm)
0.2 ps
0.3 ps
0.4 ps
0.5 ps
0.6 ps
1.5 ps
3 ps
10 ps
50 ps
500 ps
Colm 1
Colm 2

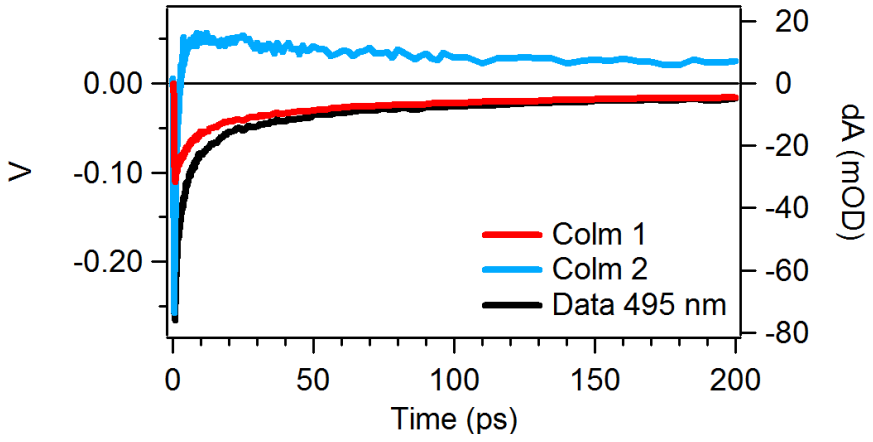
0.00
-0.10
-0.20
V
20
0
-20
-40
-60
-80
dA (mOD)
Colm 1
Colm 2
Data 495 nm
0
50
100
150
200
Time (ps)

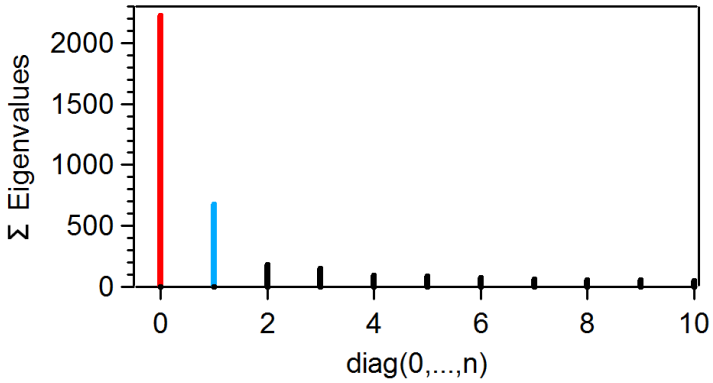
2000
1500
1000
500
0
Σ Eigenvalues
0
2
4
6
8
10
diag(0,...,n)

An example of data reconstruction of the transient dA spectrum from the first three column vectors of the U and V matrices is shown in **Figure 7 (A-G)** for the DCPS sample excited with a pump power of 220 nJ pulse^{-1}. Shown in **Figure 7 (B,D,** and **F)** is the data reconvolution from the first, first plus second, and first through third column vectors along with the respective number of eigenvalues from Σ using **Equation 2**; while **Figure 7 (C, E,** and **G)** are the residuals, respectively. It is evident that the majority of the data is contained within the first column vector; however, the residuals show a transient absorption feature which was not described. By including the second vector, the data and reconvoluted spectrum match well with no remaining signal left in the residuals. Inclusion of third vector did not improve the reconstruction or the residuals, and in fact only added noise, so this data was truncated after two vectors.

Figure 7. Singular value decomposition reconstruction of CdS DCPS transient absorption differential absorption spectrum of the raw data (A). Reconvolution of the data after SVD with one basis vector (B), two basis vectors (D), and three basis vectors (F). Residuals are shown in C, E, and G; respectively.

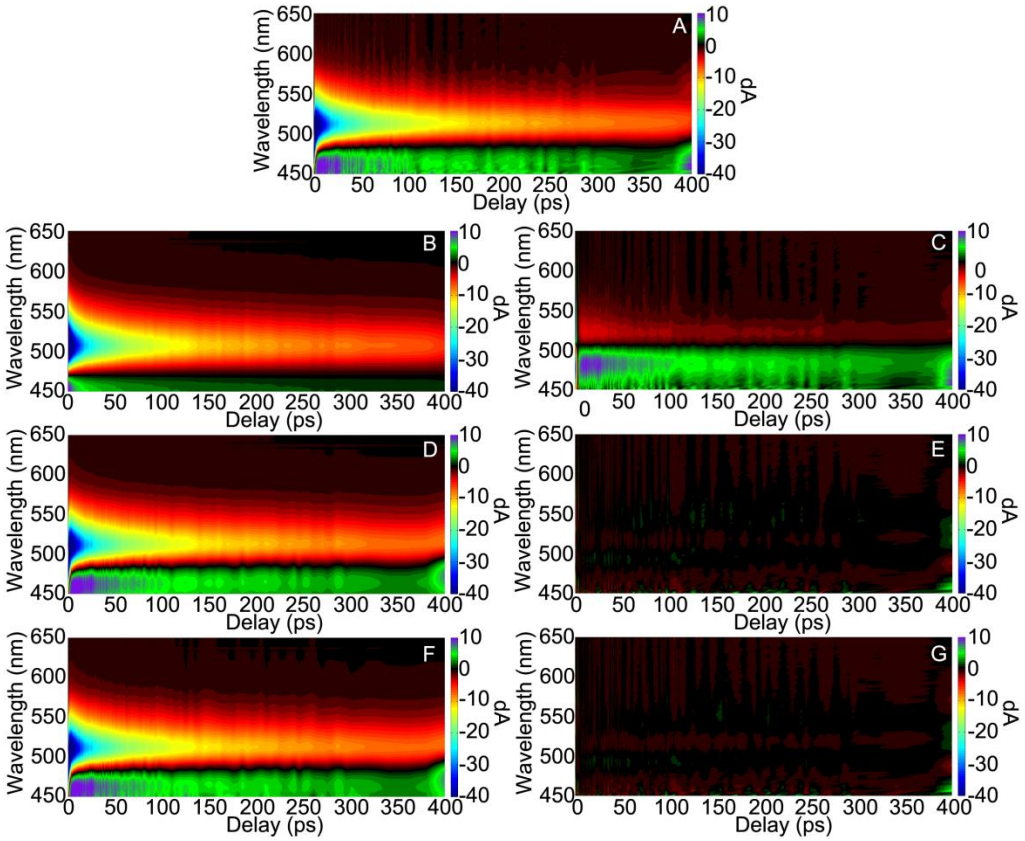

6.4.3.3 SVD-Global Fitting

From the SVD deconvolution procedure, an orthogonal time dependence trace was obtained which was fit with a 4 exponential function **(Equation 1)** for the DCPS sample, and a triple exponential function for the CBD sample. Starting with the DCPS sample, the lifetimes were found to be 1.8 ± 0.2 ps, 8 ± 0.5 ps, 65 ± 3 ps, and 450 ps. The longest time constant is not an accurate lifetime, as data was collected to 1 ns, which is not long enough to accurately fit the time dependence of this component. It is worth noting that the 1.8 ps lifetime was not necessary when the

data was fit for a single wavelength of 510 nm, but turns out to be an important component in the recombination (this point with be discussed in more detail later). The CBD sample was fit with lifetimes of 6 ± 0.4 ps, 65 ± 3 ps, and 450 ps. The lifetimes were independent of the pump flux. An example of the fit result for the DCPS sample excited with 220 nJ pulse^{-1} is shown in **Figure 8 (A)** and the CBD sample excited with 195 nJ pulse^{-1} in **Figure 8 (C)**, in which the wavelength dependent initial amplitude (B spectra) for the lifetimes as well as the sum of four B spectra is given. For comparison, the raw data is also shown at six different pump probe time delays from 0.6 to 500 ps (colored as solid traces of decreasing gray densities outlined in black, respectively).

For the DCPS sample, the global fitting uncovered a 484 nm centered 1.8 ps component, which was missed in the single wavelength fitting as its amplitude at 510 nm is relatively low. This feature is more easily seen in the 2D topographical plot, **Figure 8 (B)** in which the 1.8 ps component is mixed with the chirp (substrate response) and appears to have a time dependent red shift. The 8 ps time constant (λ_{max} = 507 nm) is blue shifted of the 65 ps component (λ_{max} = 509 nm), which decays monochromatically to the 450 ps component.

The CBD sample has a 6 ps (λ_{max} = 470 nm) feature, which in the topographical plot has less spectral red shift than the DCPS sample over the same 0 to 3 ps time interval. This can also be seen in the topography plot **Figure 8 (D)**. The 65 ps component (λ_{max} = 484 nm) decays to a 450 ps component (λ_{max} = 493 nm). All

CBD sample components were blue shifted relative to the DCPS sample, but had similar lifetimes. The discussion regarding the origin of these signals is continued below.

Figure 8. Example of SVD fit results for DCPS (A), 220 nJ/pulse, and CBD (C), 195 nJ pulse^{-1}, B spectra showing the wavelength dependence of initial amplitude of the various time constants. Also shown is the sum total of the B spectra (green). The raw data at a number of different time delays is also shown as solid traces of decreasing fill density from early to long delays. The raw topographical plots of the dA recovery over the first 30 ps are shown in B/D, respectively, for reference.

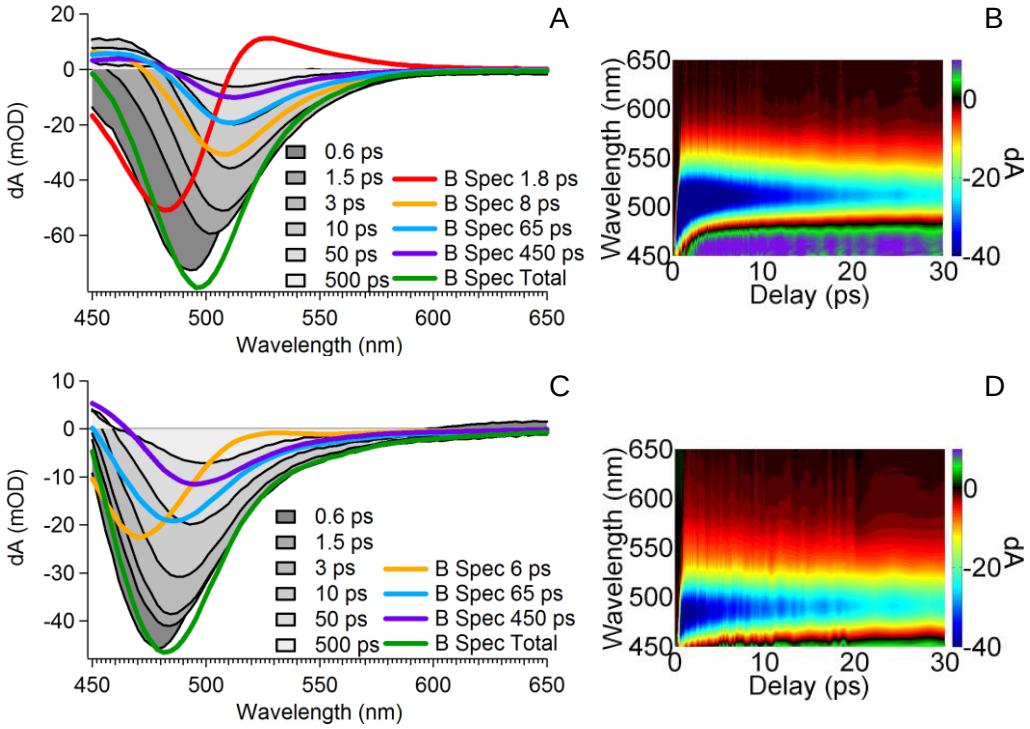

Further analysis of the B spectra was performed in an attempt to divide the broad asymmetric features of the B spectra by fitting each with a series of Gaussian peaks. The fit results for the DCPS (220 nJ pulse^{-1}) and CBD samples (195 nJ pulse^{-1}) were presented in **Figure 9 (A)** and **(B)**, respectively, in which the B spectra for the various time constants are shown as solid traces decreasing in black density from fast to slow and outlined in solid black. The Gaussian peaks used to fit the 1.8, 8, 65, and 450 ps B spectra are shown as red, orange, green, and blue traces, respectively.

Figure 9. Singular value decomposition global fit of CdS DCPS (left) and CBD (right) thin film dA spectrum of various time constants (solid traces of decreasing black density from fast to slow). Multi peak Gaussian fit of each B spectra are shown as solid lines, colored: red, orange, green, and blue.

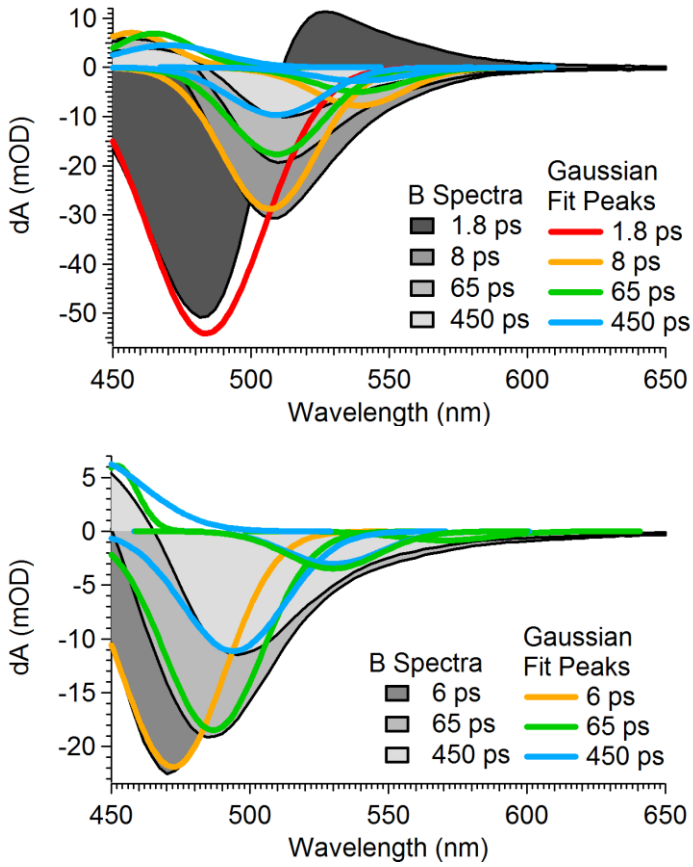

For the DCPS sample, the B spectra have three major bleach components at 484, 507, and 539 nm. The 484 nm peak has a lifetime of 1.8 ps which decays to the two 507 and 539 nm peaks. The 507 nm peak has a lifetime of 8 ps and red shifts to a 509 nm peak, which decays monochromatically via two lifetimes of 65 and 450 ps without a spectral shift. The 539 nm peak decays triple exponentially with lifetimes of 8, 65, and 450 ps. There were also several excited state absorption features seen in the DCPS sample. The broad positive 1.8 ps feature starting at 530 nm and extending to the red is due to the chirp (substrate response) feature, which is partially mixed with this component towards the red wavelengths. The blue transients are seen in the 8, 65, and 450 ps lifetimes, but their λ_{max} could not be determined.

There were four significant CBD B spectra Gaussian fit peaks, the first of which was at 473 nm and has a lifetime of 6 ps. The following dominant feature at 486 nm decayed with a lifetime of 65 ps to a red-shifted peak at 494 nm with a 450 ps lifetime. Two smaller contributions to the B spectra were found at 530 nm which have lifetimes of 65 and 450 ps . There was a remaining peak at 570 nm which decayed with time constants of 65 and 450 ps. Excited state absorption was also seen in this sample which extended blue of 465 nm with time constants of 65 and 450 ps.

The blue positive transients in both samples are assigned to a photoexcited electron trapped in a shallow or deep donor state being excited again by the probe to higher levels in the VB. This assignment is made because the recovery of these

features mirrors the recovery of the donor related recovery, as discussed in more detail later.

Each of the major Gaussian bleach features were plotted against the steady state UV-Vis absorption spectrum for the DCPS and CBD samples, **Figure 10**, respectively. From this plot, it is clear "peak 1" for the DCPS sample is the first exciton absorption for CdS. The following peaks 2 and 3 describe the exponential decay of the absorption spectra, the Urbach tail.

The CBD sample "peak 1" is blue shifted compared to E_g while "peak 2" is due to the first exciton absorption. The origin of the blue shifted "peak 1" is discussed below. The Urbach tail for this sample, described by peaks 3 and 4, is much broader than in the DCPS sample. The broad absorption tail is consistent with an amorphous material rich defect level absorption,[33] herein ascribed to O_i and V_S states. We attribute "peak 3" to absorption from CB to acceptor levels, while "peak 4" is attributed to absorption from associated centers of O_i acceptor to V_S donor states.

Figure 10. UV-Vis spectrum (solid black) of the DCPS (top) and CBD (bottom) with the multi Gaussian fit peaks of the B-spectrum for the 220 nJ pulse^{-1} and 195 nJ pulse $^{-1}$, respectively. Multipliers applied to peak 3 and 4 are shown to improve comparisons.

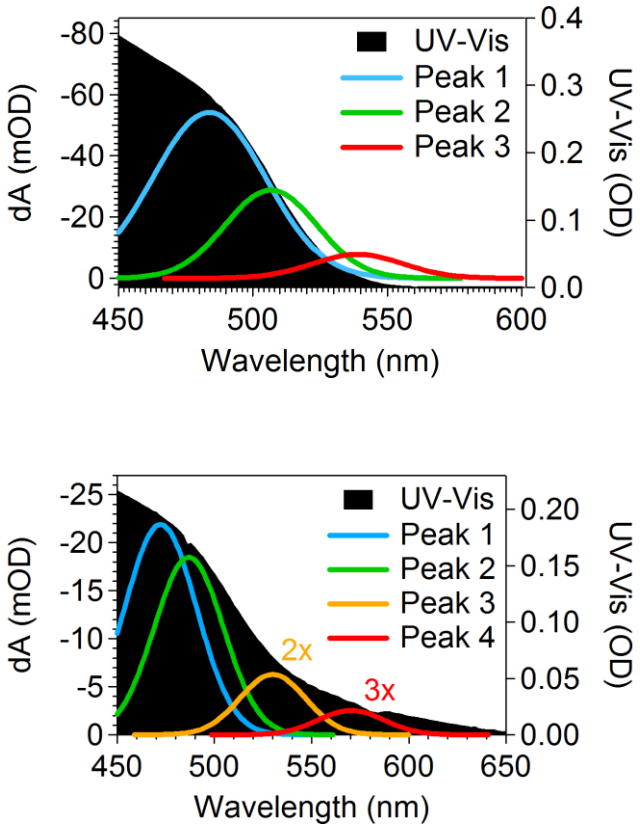

It should be made clear that a transient bleach feature found in the dA spectrum is related to depopulation of the ground state. For CdS, the E_g is 2.55 eV as seen in **Figure 10**. The DCPS sample 1.8 ps lifetime component with a spectral peak at 484 nm (2.56 eV) is assigned the trapping rate of photoelectrons from CB to shallow and deep donor levels. The peak found at 507 nm (2.45 eV) which decays with an 8 ps lifetime represents a ~100 meV energy difference between the E_g energy.

The peak at 539 nm (2.30 eV) is 240 meV less than the E_g. Because both of these peaks are transient bleach features, reduced absorption to or from these transitions was caused by stimulation of the sample by the pump. We suggest the 2.45 eV peak is due to a excitation from the CB to a shallow donor state and the 2.30 eV peak to be due to a excitation from the CB to a deep donor. Increased electron density in donor states caused by excitation of VB electrons to the CB and subsequent decay to these donor states would cause increased state filling and decreased absorption to these states from VB→donor excitation. Therefore, the CB → donor, CB → VB, shallow donor → VB, and deep donor → VB translations are governed by lifetimes of 1.8, 8, 65, and 450 ps, respectively.

The CBD sample peak at 473 nm (2.62 eV) represents absorption from the VB → CB, which at early delay times is blue shifted with respect to the expected E_g (2.55 eV). This is caused from a high donor density in the sample, which in turn overpopulates the CB to be overpopulated with electrons upon photoexcitation by the pump resulting in state filling and a shift in the apparent forbidden gap. The following peak at 486 nm (2.55 eV) is related to the decreased VB → CB absorption after the overpopulated CB empties into donor states below the CB. The peak at 530 nm (2.34 eV) is E_g – 210 meV and is attributed to the CB→acceptor excitation. The remaining 570 nm peak (2.17 eV) is E_g – 380 meV which is due to acceptor to donor transitions. The acceptor level is associated with O_i and the donor levels are due to V_S. We attribute the increased V_S to be caused by O doping.

The above described transitions and recombination processes have been summarized in **Figure 11** and refer specifically to the CBD dynamics. The unpumped sample has a partially depopulated CB due to O_i acceptor states while the V_S donor states are partially filled at room temperature. Upon excitation by the pump pulse, electrons are depopulated from both O_i and V_S states as well as the VB to fill the CB. For early time delays, the CB→VB transitions are blue shifted due to state filling. After 1-2 ps electrons repopulate the V_S states causing a red shift of the VB→CB transition. The remaining signals observed in the TA spectrum are due to depopulated acceptor state transitions to either donor levels or CB. A number of recombination channels are possible involving the V_S electrons. We assign the first 8 ps decay to recombination from CB → VB. The 65 ps recombination can be attributed to V_S to CB decay with the remaining 450 ps component due to V_S to O_i recombination.

Figure 11. Mechanism of electron relaxation investigated by ultrafast pump probe spectroscopy stimulated by 460 nm pump and probed with white light (450-800 nm) continuum for the CBD sample. Electrons in the unpumped ground state (GS) occupy the VB and partially both O_i acceptor and V_S donor states. Excitation with the pump laser depopulates the electrons, which decay back to the ground state via three lifetimes: 8, 65, and 450 ps. The vertical transitions detail the origin of the observed features in the dA spectrum for this sample. Labels 1-4 refer to the peak assignments made in **Figure 8**. The relative occupation density of the CB and V_S and depopulation of VB electrons (solid pink and black, respectively) are used as a visual

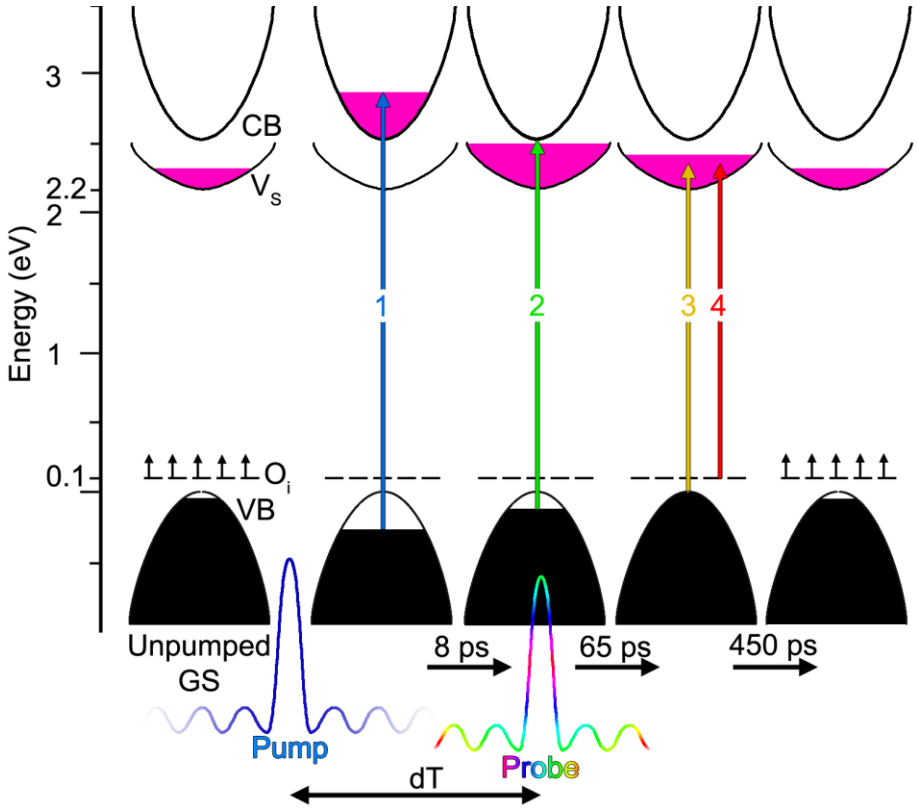
Energy (eV)
3
2.2
2
1
0.1
CB
V_s
O_i
VB
1
2
3
4
Unpumped
GS
Pump
dT
Probe
8 ps
65 ps
450 ps

6.4.3.4 Power Dependence

The TA dA spectrum was recorded for each sample under five different pump fluences ranging from 24, 48, 86, 220, and 707 nJ pulse^{-1} for the DCPS sample; and, 20, 35, 54, 195, and 890 nJ pulse^{-1} for the CBD sample. The TA spectra were analyzed with the above described SVD-global fitting methodology, and the resulting B spectra were reported in **Supplemental Figure S1**. Considering the optical density of the substrate and the laser spot area (1 mm^2), the electron hole density created upon photo excitation (η) ranged from 2.5x10^{12} to 1.1x10^{14} cm^{-3}. These densities are well below the Mott criterion ($\eta \sim {a_B}^{-3}$), where a_B is the bohr exciton radius, for significant exchange correlation effects and subsequent bandgap renormalization effects.[34]

The power dependence of the λ_{max} of the B spectra Gaussian fit peaks for the two samples is shown in **Figure 12**. The following "peak" labels refer to **Figure 10** labels, and have been colored respectively.

Beginning with the DCPS sample, 1.8 ps B spectrum Gaussian fit "peak 1" had no amplitude at 24 nJ pulse^{-1} pump fluence, but increased with an inverse square root dependence from 2.52 eV to 2.56 eV from 48 to 707 nJ pulse^{-1}, respectively. The observed E_g in the dA spectrum crossed the expected first exciton absorption energy slightly above the 86 nJ pulse^{-1} pump energy (1.1x10^{13} cm^{-3} photoelectron density). The 8 ps time constant B spectra had two Gaussian fit peaks. The first "peak 2" had an absorption energy of 2.41 eV at 24 nJ pulse^{-1} and increased with an

inverse square root dependence to 2.45 eV at 707 nJ pulse^{-1}. The E_g offset of this peak at 220 nJ pulse^{-1} was 110 meV. The second peak in the 8 ps B spectrum, "peak 3" was pump power independent, which has an absorption energy of 2.3 eV. The E_g offset of this last peak was 250 meV. Low donor density and fast recombination lifetime of the CB → VB transition can explain the reduced Burstein Moss shift in the DCPS sample. Due to the E_g offset and that it is a bleach feature, "Peak 2" and "Peak 3" are assigned to a VB→donor level absorption. There are a number of donor states in CdS in this energy range, and little can be said about the identity of the states involved in the transitions.[10] "Peak 2" was seen to have the same power dependent energy shift as "Peak 1". This indicates that a trapping process, lower in energy than "Peak 2," which becomes saturated at higher powers allows for state filling in both Peak 1 and Peak 2 bands.

For the CBD sample, the 6 ps B spectrum Gaussian fit has an absorption energy ("peak 1") at the lowest excitation energy of 2.46 eV, which blue shifted with an inverse square root dependence to 2.66 eV at 890 nJ pulse^{-1}. In the 65 ps B spectrum, there were three Gaussian features of majority contribution. The first peak, "peak 2", started at 2.46 eV at the lowest pump power and blue shifted to 2.56 eV at the highest pump power with inverse square root dependence as well. The second ("peak 3") and third ("peak 4") peak positions are power independent at 2.34 eV (530 nm) and 2.18 eV (570 nm), respectively. The lack of any power dependence of the latter two peaks is consistent with the assignment of these features due to CB→V_S and O_i→V_S absorption as seen in the dA spectrum, respectively. Also, the significant

shift of the apparent gap in the "peak 1" data suggests the donor density in the CBD sample was higher than the DCPS sample. Due to the expected donor level of the V_S states, "peak 4" is consistent with a VB→V_S transition. The remaining "peak 4" is assigned to DAP absorption between O_i→V_S.

Figure 12. Plot of the laser pump induced photoelectron density vs. λ_{max} of the DCPS (left) and CBD (right) B spectra Gaussian fit features. Peak labels are with respect to **Figure 9** assignments. Data fits are shown as solid lines.

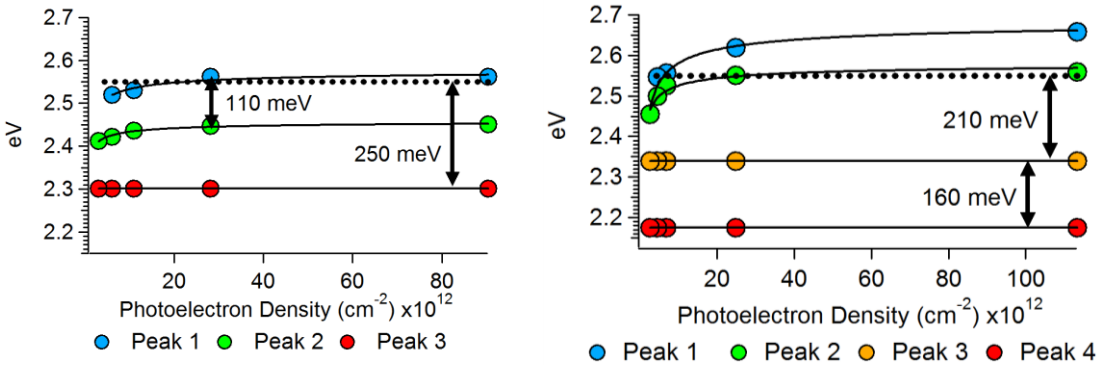

6.5 Conclusions

The excited state recombination of photoexcited charge carriers in CdS thin films prepared by DC pulse sputtering (DCPS) and chemical bath deposition (CBD) have been studied by ultrafast transient absorption pump probe spectroscopy. The DCPS film of 100 nm thickness consists of the wurtzite crystalline phase, while the CBD sample of 70 nm thickness of zinc blende phase of lower crystallinity than the DCPS sample. The oxygen content in the CBD sample was taken to be approximately 10%. The differential absorption (dA) was monitored by a while light probe for the first 1 ns after photoexcitation by a 460 nm pump at five different excitation fluence. SVD global fitting was applied to the dA spectra to obtain

wavelength independent lifetimes and time independent initial amplitudes (B spectra). The lifetimes of the DCPS sample were 1.8, 8, 65, and 450 ps which were related to carrier trapping in donor states, CB→VB recombination, shallow donor recombination, and deep trap recombination, respectively. The CBD sample has lifetimes of 6, 65, and 450 ps which were assigned to CB→VB recombination, donor → VB recombination related to V_S states, and donor acceptor pair (DAP) recombination due to V_S → O_i, respectively. Detailed analysis of the B spectra supports the above assignments and were compared for a range of pump fluence used. The results suggest that DCPS deposited CdS should provide improved performance in applications such as window layers in solid state solar cells. This study also demonstrates the power of ultrafast laser spectroscopy in unraveling detailed information about exciton and charge carrier dynamics in semiconductors.

6.6 Acknowledgments

This work was supported by the BES Division of the US DOE. The authors gratefully appreciate Yashar Abdollahian for his expertise and time in collecting XRD. Special thanks to Tom Yuzvinsky for his assistance with SEM. Thanks to Robert Fitzmorris for his discussions and edits.

6.7 Supporting Information

Figure S1. Singular value decomposition global fit B spectra of CdS DCPS thin film (A/B/C/D) for the 1.5 ps (A), 8 ps (B), 65 ps (C), and 450 ps (D) lifetimes for all 5 pump powers: 707 (red), 220 (gold), 86 (green), 48 (blue), and 24 (purple) nJ/pulse. CdS CBD thin film B spectra (E/F/G) for the 6 ps (E), 65 ps (F), and 450 ps (G) lifetimes for all 5 pump powers: 890 (red), 195 (gold), 54 (blue), 35 (green), and 20 (purple) nJ/pulse.

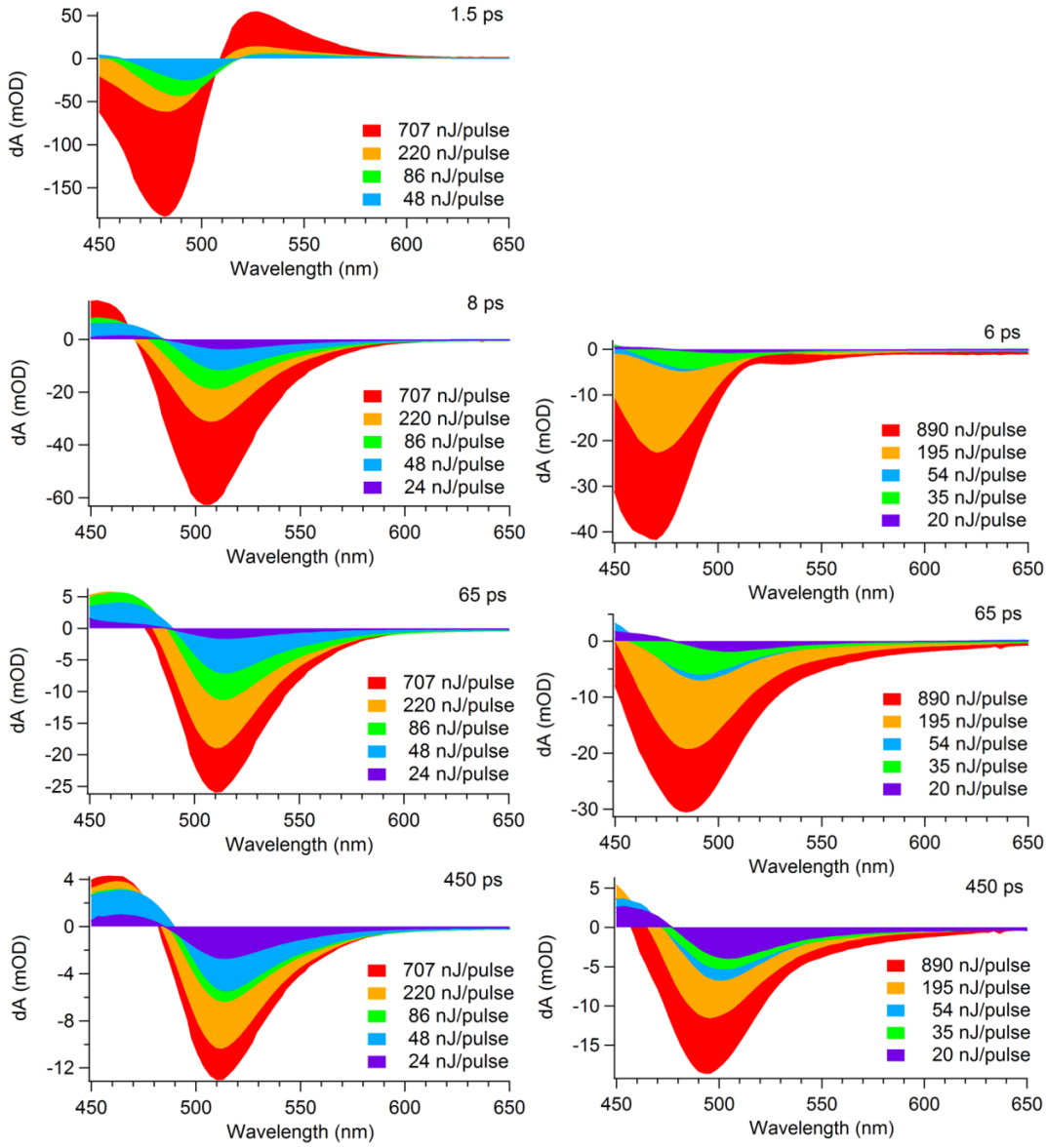
1.5 ps
707 nJ/pulse
220 nJ/pulse
86 nJ/pulse
48 nJ/pulse
dA (mOD)
Wavelength (nm)
8 ps
707 nJ/pulse
220 nJ/pulse
86 nJ/pulse
48 nJ/pulse
24 nJ/pulse
6 ps
890 nJ/pulse
195 nJ/pulse
54 nJ/pulse
35 nJ/pulse
20 nJ/pulse
65 ps
450 ps

6.8 References

1. Chirilă, A.; Buecheler, S.; Pianezzi, F.; Bloesch, P.; Gretener, C.; Uhl, A. R.; Fella, C.; Kranz, L.; Perrenoud, J.; Seyrling, S.et al. Highly efficient Cu(In,Ga)Se2 solar cells grown on flexible polymer films. *Nat. Mater.* **2011**, 10, 857-861.

2. Oliva, A.; Castro-Rodrıguez, R.; Solıs-Canto, O.; Sosa, V. c.; Quintana, P.; Pena, J. Comparison of properties of CdS thin films grown by two techniques. *Appl. Surf. Sci.* **2003**, 205, 56-64.

3. Martil, I.; Diego, N. D.; Hidalgo, C. Role of defects in the annealing behavior of RF sputtered cadmium sulfide films. *Physica Status solidi (a)* **1986**, 94, 587-593.

4. Kadirgan, F.; Mao, D.; Song, W.; Ohno, T.; McCandless, B. Properties of electrodeposited cadmium sulfide films for photovoltaic devices with comparison to CdS films prepared by other methods. *Turk. J. Chem.* **2000**, 24, 21-34.

5. El Deeb, A. F. Structural and optical characteristics of CdS thin films deposited by infrared pulsed-laser technique. *Eur Phys J-Appl Phys* **2007**, 38, 247-252.

6. Vigil-Galán, O.; Vidal-Larramendi, J.; Escamilla-Esquivel, A.; Contreras-Puente, G.; Cruz-Gandarilla, F.; Arriaga-Mejía, G.; Chavarría-Castañeda, M.; Tufiño-Velázquez, M. Physical properties of CdS thin films grown by pulsed laser ablation on conducting substrates: effect of the thermal treatment. *Phys. Status Solidi A* **2006**, 203, 2018-2023.

7. Escamilla-Esquivel, A.; Contreras-Puente, G.; Tufino-Velazquez, M.; Albor-Aguilera, M.; Vigil, O.; Vaillant, L. Photoluminescence studies of CdS films grown by close-spaced vapor transport hot walls. *J. Appl. Phys.* **1999**, 86, 3171-3174.

8. Raji, P.; Sanjeeviraja, C.; Ramachandran, K. Thermal and structural properties of spray pyrolysed CdS thin film. *Bull. Mater. Sci.* **2005**, 28, 233-238.

9. Taguchi, T.; Ray, B. Point defects in II–VI compounds. *Prog. Cryst. Growth Charact. Mater.* **1983**, 6, 103-162.

10. Abken, A. E.; Halliday, D.; Durose, K. Photoluminescence study of polycrystalline photovoltaic CdS thin film layers grown by close-spaced sublimation and chemical bath deposition. *J. Appl. Phys.* **2009**, 105, 064515-064515-064519.

11. Aguilar-Hernández, J.; Contreras-Puente, G.; Morales-Acevedo, A.; Vigil-Galán, O.; Cruz-Gandarilla, F.; Vidal-Larramendi, J.; Escamilla-Esquivel, A.; Hernández-Contreras, H.; Hesiquio-Garduño, M.; Arias-Carbajal, A.et al. Photoluminescence and structural properties of cadmium sulphide thin films grown by different techniques. *Semicond. Sci. Technol.* **2003**, 18, 111.

12. Wenyi, L.; Xun, C.; Qiulong, C.; Zhibin, Z. Influence of growth process on the structural, optical and electrical properties of CBD-CdS films. *Mater. Lett.* **2005**, 59, 1-5.

13. Subba Ramaiah, K.; Pilkington, R. D.; Hill, A. E.; Tomlinson, R. D.; Bhatnagar, A. K. Structural and optical investigations on CdS thin films grown by chemical bath technique. *Mater. Chem. Phys.* **2001**, 68, 22-30.

14. Espinosa-Rosas, M.; Aguilar-Hernández, J.; Hernández-Contreras, H.; Hernández-Pérez, M.; Contreras-Puente, G.; Cárdenas-García, M.; Ortega-Nájera, B. In *Mater. Sci. Forum*; Trans Tech Publ: 2011; Vol. 691, p 145-150.

15. Gutowski, J.; Sebald, K.; Voss, T. In *Semiconductors*; Springer: 2009, p 47-48.

16. Rempel, A. A.; Valeeva, A. A.; Kozhevnikova, N. S. Identification of structural vacancies in carbides, oxides, and sulfides by Doppler broadening of the gamma-ray line. *JETP Letters* **2010**, 92, 146-150.

17. Kar, S.; Biswas, S.; Chaudhuri, S.; Nambissan, P. M. G. Finite-size effects on band structure of CdS nanocrystallites studied by positron annihilation. *Phys. Rev. B* **2005**, 72, 075338.

18. O'Brien, P.; McAleese, J. Developing an understanding of the processes controlling the chemical bath deposition of ZnS and CdS. *J. Mater. Chem.* **1998**, 8, 2309-2314.

19. Kylner, A.; Lindgren, J.; Stolt, L. Impurities in chemical bath deposited CdS films for Cu (In, Ga) Se2 solar cells and their stability. *J. Electrochem. Soc.* **1996**, 143, 2662-2669.

20. Stoev, M.; Katerski, A. XPS and XRD study of photoconductive CdS films obtained by a chemical bath deposition process. *J. Mater. Chem.* **1996**, 6, 377-380.

21. Yandong, M.; Dai, Y.; Huang, B. Magnetism in non-transition-metal doped CdS studied by density functional theory. *Comp Mater Sci* **2011**, 50, 1661-1666.

22. Chadi, D. J. The Problem of Doping in II-VI Semiconductors. *Annu Rev Mater Sci* **1994**, 24, 45-62.

23. Akimoto, K.; Okuyama, H.; Ikeda, M.; Mori, Y. Oxygen doping in CdTe, CdS and ZnS. *J. Cryst. Growth* **1992**, 117, 420-423.

24. Akimoto, K.; Okuyama, H.; Ikeda, M.; Mori, Y. Isoelectronic oxygen in II-VI semiconductors. *Appl. Phys. Lett.* **1992**, 60, 91-93.

25. Nazarova, L. D.; Morozova, N. K.; Butnev, K. N. Effect of Doping with Oxygen and Tellurium on the Intrinsic-Defect Structure of CdS and ZnSe. *Inorganic Materials* **1996**, 32, 481-484.

26. Zhong, D.; Parthasarathy, G.; Nardi Jr, R. A.; Google Patents: 2011.

27. Newhouse, R. J.; Wang, H.; Hensel, J. K.; Wheeler, D. A.; Zou, S.; Zhang, J. Z. Coherent Vibrational Oscillations of Hollow Gold Nanospheres. *J. Phys. Chem. Lett.* **2011**, 2, 228-235.

28. Hug, S. J.; Lewis, J. W.; Einterz, C. M.; Thorgeirsson, T. E.; Kliger, D. S. Nanosecond photolysis of rhodopsin: evidence for a new blue-shifted intermediate. *Biochemistry* **1990**, 29, 1475-1485.

29. Gutowski, J.; Sebald, K.; Voss, T. In *New Data and Updates for III-V, II-VI and I-VII Compounds*; Springer: 2010, p 294-295.

30. Gul, S.; Cooper, J. K.; Corrado, C.; Vollbrecht, B.; Bridges, F.; Guo, J.; Zhang, J. Z. Synthesis, Optical and Structural Properties, and Charge Carrier Dynamics of Cu-Doped ZnSe Nanocrystals. *J. Phys. Chem. C* **2011**, 115, 20864-20875.

31. Fitzmorris, B. C.; Cooper, J. K.; Edberg, J.; Gul, S.; Guo, J.; Zhang, J. Z. Synthesis and Structural, Optical, and Dynamic Properties of Core/Shell/Shell CdSe/ZnSe/ZnS Quantum Dots. *J. Phys. Chem. C* **2012**, 116, 25065-25073.

32. Fitzmorris, B. C.; Pu, Y.-C.; Cooper, J. K.; Lin, Y.-F.; Hsu, Y.-J.; Li, Y.; Zhang, J. Z. Optical Properties and Exciton Dynamics of Alloyed Core/Shell/Shell Cd1–xZnxSe/ZnSe/ZnS Quantum Dots. *ACS Appl. Mater. Interfaces* **2013**.

33. John, S.; Soukoulis, C.; Cohen, M. H.; Economou, E. Theory of electron band tails and the Urbach optical-absorption edge. *Phys. Rev. Lett.* **1986**, 57, 1777-1780.

34. Grundmann, M. *The physics of semiconductors: an introduction including devices and nanophysics*; Springer-Verlag Berlin Heidelberg, 2006.